DESIGN AND FABRICATION OF ON-CHIP HIGH POWER OPTICAL PHASED ARRAYED WAVEGUIDES

by

Yun Jo Lee

A Dissertation

Submitted to the Faculty of Purdue University

In Partial Fulfillment of the Requirements for the degree of

Doctor of Philosophy

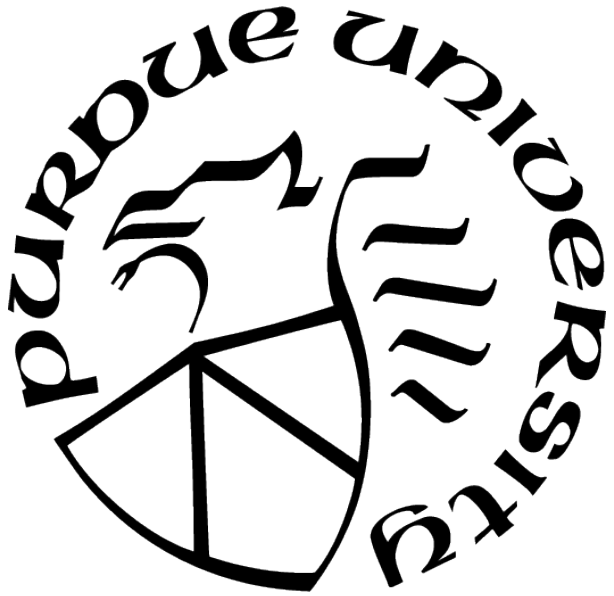

School of Electrical and Computer Engineering

West Lafayette, Indiana

December 2021

THE PURDUE UNIVERSITY GRADUATE SCHOOL
STATEMENT OF COMMITTEE APPROVAL

Dr. Minghao Qi, Chair

School of Electrical and Computer Engineerings

Dr. Andrew M. Weiner

School of Electrical and Computer Engineerings

Dr. Vladimir M. Shalaev

School of Electrical and Computer Engineerings

Dr. Alexandra Boltasseva

School of Electrical and Computer Engineerings

Approved by:

Dr. Dimitrious Peroulis

To my lovely wife Jieun Lim

and my family who faithfully supported my PhD life

ACKNOWLEDGMENTS

Firstly, I would like to thank my advisor, Professor Minghao Qi, for giving me the valuable opportunity to pursue my graduate study. His patience and generous support gave me a freedom to research various idea. Without him, I would not even attempt to start my graduate study. During my graduate study, he introduced various research topics and gave me his scientific insight and broad spectrum of knowledge about them when I encountered many challenges. I want to also thank Professor Andrew M. Weiner for his excellent guidance. It has been always my privilege to discuss and work with him.

I also want to thank my committee members Professor Vladimir M. Shalaev and Professor Alexandra Boltasseva for their valuable time, help, and suggestions for improving my work.

I was lucky to meet my colleagues, specially Dr. Yi Xuan, Dr. Ben Niu, Dr. Sangsik Kim, Dr. Min Teng, Dr. Cong Wang, Ziyun Kong, Gregory Chang, Yingheng Tang, and Ruihan Chen. Because of the valuable discussions with them, I have learned many detailed skills and theories on my research. Thus, I also want to thank them.

I want to also give thanks to a leader of the Accelerator-on-Chip (ACHIP) program, Professor Robert L. Byer. He helped me join the ACHIP program and guided me to start the research work while I was in Stanford University as a visiting research student. I want to also give thanks to Dr. Joel England, who always organized the weekly ACHIP collaboration meetings, and he helped me to study basic theory of particle accelerators. I want to also give thanks to ACHIP collaborators: Professor Peter Hommelhoff, Professor Olav Solgaard, Professor James S. Harris, Professor Jeleena Vuckovic, Mr. Tom Langenstein, Dr. Kent Wootton, Dr. Si Tan, Dr. Tyler W. Hughes, Dr. Zhexin Zhao, Dr. Neil Sapra, Dr. Yu Miao, Dr. Ken Leedle, Dr. Karel Urbanek, Dr. Andrew Ceballos, Dr. Dylan Black, Dr. Huiyang Deng, Dr. Kiyoul Yang, Dr. Jean-Philippe MacLean and Payton Broaddus. It was a great opportunity for me to work with them to demonstrate the concept of dielectric laser accelerators (DLAs).

I want to also give thanks to the staff members in the Birck Nanotechnology Center, specially Mr. William Rowe, Dr. Justin Wirth, Dr. Joon Park, Mr. Richard Hosler, and

Mr. Francis Manfred. When I had troubles in fabrication works, they always helped me to resolve them and taught me various fabrication skills.

I want to also thank my family for their love and infinite supports through my life. Especially, I thank my wife Jieun Lim for her love, full-hearted support, and encouragement.

Finally, I praise God, who is always with me and gives me the strength and upholds me with his righteous right hand.

TABLE OF CONTENTS

LIST OF TABLES

LIST OF FIGURES

ABSTRACT

The Complementary Metal-Oxide-Semiconductor (CMOS) industry has seen tremendous developments over the past several decades and state-of-the-art fabrication technology has likewise been developed. This fabrication technology develops Photonic Integrate Circuits (PIC) which can guide, split, and modulate photonic waves within a small chip scale. On-chip optical phased arrayed waveguides that operate at high power overcome the current limitations of some conventional applications. This paper discusses two applications of on-chip optical waveguide systems: optical phased array (OPA)-based Light Detection and Range (LiDAR) and waveguide array Dielectric Laser Accelerator (DLA). Both the LiDAR and DLA structures require similar properties to achieve optimized performance. These properties are as follows: capability to handle high power, the ability to split the high power evenly through several waveguide branches and distribute the same degree of optical phase on each branch at specific spatial locations, efficient designs of active phase-tuning structures, and the ability to re-combine several waveguide branches into the sub-wavelength pitch spacing array without crosstalk. Additionally, both structures must resolve specific fabrication challenges on each waveguide component. To address these issues, this paper discusses the theoretical reviews of OPA, the Laser-Induced Damage Threshold (LIDT) of optical waveguide materials, and techniques to reduce crosstalk in sub-wavelength pitch size arrays, such as extreme skin-depth (e-skid) waveguides and propagation constant mismatched waveguides. We propose optimized designs for both OPA-based LiDAR and waveguide array DLA with passive and active devices, respectively, and explain the optimized parameters and its simulation results for each component from the full layout of devices. Furthermore, we discuss the fabrication process of the devices and show the resolutions of fabrication challenges, such as trapping void gaps in an e-skid array structure, writing errors of electron beam lithography of large dense patterns, and silicon nitride to silicon hybrid waveguide pattern alignments. Next, we show the experimental setups and the measurement results from the fabricated OPA devices and analyze the results. Finally, this paper concludes the research of the proposed devices and proposes more designs for both OPA-based LiDAR and waveguide arrayed DLA structures that can further increase increase its performance.

1. INTRODUCTION

The field of solid-state electronics has seen tremendous developments over the past several decades due to the expansion of the Complementary Metal-Oxide-Semiconductor (CMOS) industry, and state-of-the-art nanofabrication technologies have thus been developed. A field of optics has also been developed due to the significant global demand for rapid telecommunication through optical fiber or wireless connections. Silicon photonics has emerged from the development of these two fields. Since silicon is highly transmittable in C-band (the wavelength that ranges from 1530 nm to 1565 nm that is widely used for optical fiber communication) and has a relatively higher refractive index than other transparent materials, it can be implemented into photonic integrated circuits (PIC), which enable photonic signal processing onto chip-scale devices, similar to conventional electronic integrated circuits (IC). PIC utilizes various optical applications and can substitute various conventional optical devices with size reductions, higher densities, lower costs, faster responses, and larger bandwidths. The on-chip optical phased arrayed waveguide structure is promising and representative of PIC as it can substitute conventional bulky and expensive systems to smaller sizes and cost-efficient products due to the silicon-based mass production from the foundry. Light detection and ranging (LiDAR) systems and particle accelerators are among those conventional technologies that have the potential to be replaced with silicon photonics-based OPA applications. The following chapter briefly discusses the concepts and mechanisms of LiDAR and particle accelerators. Then, it explains the conventional technologies of LiDAR and particle accelerators that are currently widely utilized in commercial markets and research fields. Then, we discuss the optical phased array (OPA) technology that has the potential to replace conventional LiDAR systems. We also discuss the concept and motivations of dielectric laser accelerators (DLAs), a promising next-generation accelerator. Finally, this chapter describes the shared characteristic requirements of the two systems for applying optical phased arrayed waveguide structures, and summarizes the discussion presented in this thesis.

1.1 LiDAR

LiDAR is a method of instantaneously measuring a distance of targeted object by calculating the time difference between a light traveling between the emission of modulated laser from the sensor and the time of received one from the reflection by the object. It is a prospective technology for Advanced Driver-Assistance Systems (ADAS) and autonomous vehicles (AV) as it generates 3D maps of the surrounding environment in real-time. Due to its high cost, there is still discussion between entrepreneurs and automotive engineers regarding whether LiDAR sensor technology is necessary for automotive driving. However, it is certainly helpful in avoiding collision with an object in the event of sensor or system failure.

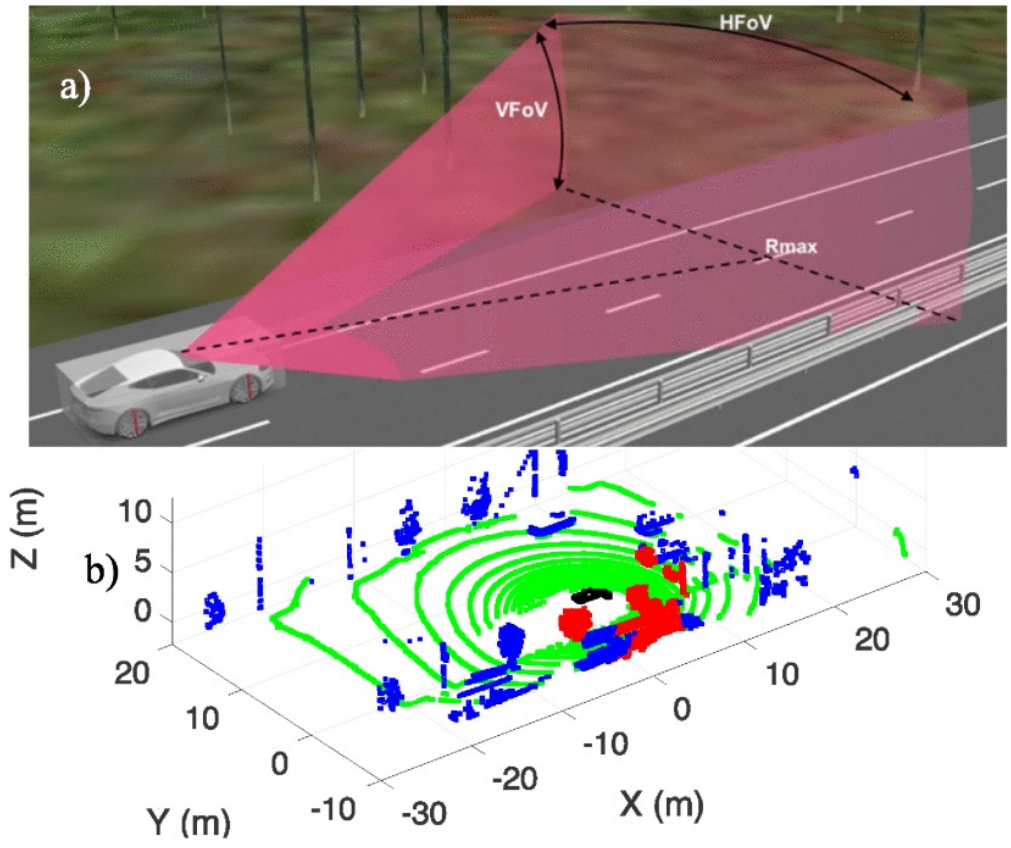

Figure 1.1. (a) Illustration of spatial coverage by a generic environmental perception sensor. (b) Examples of 3D LiDAR pointcloud surrounded by vehicle [1].

To map the surrounding environment in real-time, LiDAR sensors scan surrounding objects by rapidly emitting laser beams at horizontal and vertical angles. The sensor receives the beam via reflection from the scanned object. Generally, LiDAR sensors operate using an angular scanning range called field-of-view (FoV); the lateral angular range is called the horizontal field-of-view (HFoV) and the vertical angular range is called the vertical field-of-view (VFoV). The sensor can calculate distances by distinguishing between the signal and the noise from the receiver; this is known as the detection range (R_{max}). Figure 1.1 (a) illustrates the spatial coverage of the environment from the LiDAR sensor [1].The amount of scanning iteration that occurs per second is called the frame rate and the precise measurement of an angle is called angular resolution. Figure 1.1 (b) is an example of pointcloud; the sensor recognizes the environment concerning distance via reflected signals. The performance of LiDAR sensors can be limited. Larger HFoV and VFoV ranges, longer detection ranges, faster scanning rates, and more precise angular resolutions allow for better LiDAR sensor performances. Table 1 shows the estimated specifications of LiDAR for Level 4 and 5 AV [2].

Table 1.1. Estimated specifications of LiDAR for Level 4 and 5 AV [2].

Items	**Specs**
Range	>200 m
HFoV	>120°
VFoV	>25°
Angular resolution	<0.1
Frame rate	>15 Hz

1.1.1 Conventional LiDAR system

Figure 1.2 shows the different LiDAR technologies that have been proposed for automotive 3D LiDAR scanning [1]. Except for flash LiDAR, LiDAR technologies scan the FoV by rotating one or more light emitters. When LiDAR was first developed, macro-mechanical scanning was the only option when using the 3D LiDAR sensor and is still widely implemented in sample AV and selling broadly in the commercial market. Macro-mechanical

scanning LiDAR sensors directly rotate the light source and receiver, enabling 360-degree detection. Velodyne is a representative company and the first who have implemented this technology in their LiDAR sensors. However, the size of its sensor is bulky and restrains the freedom of the exterior designs of the vehicles. Additionally, due to difficulty in its mass production, the sensor is expensive. To compensate for this, micro-mechanical scanning LiDAR sensors have been developed. They use microelectromechanical system (MEMS) technology. MEMSs have rotational micro-sized mirrors mounted in front of the laser source and scan the HFoV and VFoV by rotating the mirrors inside. As they are fabricated from CMOS-based foundries by utilizing silicon substrates, the cost of their production is much lower than that of macro-mechanical rotational LiDAR sensors. However, MEMS micro-mirrors have rotational limitations and thus smaller FoV ranges than other LiDAR sensor technologies. Additionally, the micrometer-sized rotational mirror is easily broken by external forces. Flashed LiDAR systems generate electromagnetic pulses and then receive signals and calculate the time-of-flight (ToF). Although they have no moving parts, they are only available in short/middle ranges due to the concern of maximum power for eye safety [1]. Furthermore, its detector is more complex and more expensive. The optical OPA-based LiDAR sensor is the latest proposal. It was developed based on antenna theory; its technique is to create and control the array beam from the coherent optical frequency source to point in different directions, without moving the emitter structure. As this can be achieved using silicon photonic integrated circuits, its size is much smaller than any other LiDAR technology and it is much cheaper due to its fabrication from CMOS-based foundry processes. Additionally, since it does not have any physical moving parts to steer the beam, it is durable and more reliable for AV applications. Hence, it is a promising technology to substitute the conventional LiDAR systems described above. The basic theory behind its development and its operational mechanisms are described in the following chapter. Previous articles of introducing OPA-based LiDAR devices cannot achieve both large FoV and detection range at the same time. This paper offers a proposal as to how both can be achieved at the same time.

1.2 Particle Accelerators

1.2.1 Conventional particle acccelerators

A particle accelerator is a machine that accelerates electrically charged particles (such as protons, electrons, and ions) so that they travel at very high speeds with a high amount of energy. It is widely used for high-energy particle physics research. Particle accelerators are applicable in many commercial markets; they can be used in cancer treatment, micro-organics, and as tools for investigating material properties, among other things. Electromagnetic fields provide energy to the particles. The electric field drives kinetic energy to the charged particles to gain speed; the magnetic field deflects its path so that additional acceleration can be gained. The easiest way to accelerate a charged particle is to set two static electrodes with constant voltage differences. However, this kind of accelerator structure limits the amount of energy gained as electrical breakdown occurs between the static electrodes. To achieve higher acceleration, the particle accelerator must use an oscillating electric field system. To provide oscillation, radio frequency (RF) electric field generators are widely used in typical particle accelerators. However, RF accelerators must be large in size, ranging at least a few miles, due to the electric field breakdown limit of their electrode materials. Generally, RF accelerators are limited to an acceleration gradient of approximately 20 to 30 MeV/m [3], and it is due to the electric field breakdown by the copper. Thus, conventional metallic RF accelerators have limited potential to improve acceleration gradients. Plasma-based accelerators are a promising tool to develop higher acceleration gradients, however, they usually require a high initial velocity (close to the speed of light) of input charged particles to accelerate, so it is unsuitable in many applications [4]. Therefore, new technology is needed to achieve higher acceleration gradients while reducing the cost and size of the device for its utilization in various applications.

1.2.2 DLAs

To achieve higher acceleration gradients from the conventional accelerator system, metallic materials must be replaced with dielectrics to avoid any breakdown in the electric field.

Additionally, using a much higher frequency than RF increases the acceleration gradient to the charged particles. DLAs were developed in response to these factors. They are composed of dielectric materials and operate via optical frequency. Since tremendous nanofabrication technologies have been developed by the semiconductor industry, it is now possible to fabricate nanometer-sized structures out of dielectric materials with high yield and precision. Likewise, laser modulation technologies have been developed to produce a laser source with shorter pulse duration and higher and more stable power to produce, in turn, a more stable electric field.

The first DLA structure was proposed in 2006 based on dual grating [5] and its experimental demonstration was conducted in 2013 by Prof. Byer's group at Stanford University [6]. In this experiment, fused silica was used to fabricate the dual grating structure. It achieved 100 keV energy gain at 360 μm of its interaction length starting from 60 MeV electron beams (which is in the relativistic regime); this energy gain corresponded to 300 MeV/m of acceleration gradient. A few months later, Prof. Hommelhoff's group at FAU Erlangen in Germany successfully demonstrated DLA acceleration at the sub-relativistic regime for the first time. Using similar fused silica dual pillar structures, they accelerated the electrons to 0.275 keV energy gain at 11 μm, corresponding to 25 MeV/m of acceleration gradient from 28 keV of lower initial energy [7]. Moreover, in 2015, Dr. Leedle from Stanford University demonstrated much a higher acceleration gradient at the sub-relativistic regime using a silicon-based DLA with a single grating structure [8] and dual pillar structures [8] and dual pillar structures [9]. The single grating structure achieved 1.22 keV of energy gain at 5.6 μm with an initial energy of 96.3 keV, which corresponded to 200 MeV/m acceleration gradient [8], the dual pillar structure recorded 370 MeV/m of acceleration gradient from the same experimental conditions [9].

Based on these DLA experimental demonstrations, the accelerator on-chip (ACHIP) group has been established and includes researchers from various international universities and national labs. The group has been funded by the Gordon and Betty Moore Foundation since 2015. ACHIP group focus on the demonstration of shoebox-sized accelerators that can achieve higher acceleration gradients. Thus, on-chip dielectric waveguide integration with DLA structure became quite important to achieve ACHIP's goal, and several such integration

design are proposed and demonstrated for a while. In 2018, we first proposed the designs of 'tree-branch' dielectric waveguide network which enable to distribute the power uniformly among the longer interaction length up to few hundreds of micro-meters of DLA structures [11]. Additionally, Dr. Neil Sapra, an ACHIP member, experimentally demonstrated the silicon-only waveguide-integrated DLA structure with a photonic inverse design approach in 2020 [12]. The device was driven by a near-infrared (NIR) pulsed laser and recorded 1.21 keV of energy gain among 30 μm of its interaction length, which was the same as its waveguide width, starting from 83.4 keV of initial electron energy beam. . Therefore, some additional steps were required to fabricate a device with a DLA structure extendable by more than a few hundred micrometers in length, operating at high power, and actively tuning the input NIR laser source.

1.3 Requirements of LiDAR and DLA using silicon-based on-chip waveguides

Both OPA LiDAR structures and waveguide-integrated DLA structures share similar characteristic requirements to overcome limitations with regards to performance. Firstly, both structures must consist of dielectric materials that can sustain high power input laser sources to deliver power uniformly among the targeted structures without degradation. Secondly, both structures must deliver and generate either the same phased or a certain degree of the same delayed-phased array at the output ports, so both structural components must not only distribute the high optical power with an equal amount of magnitude on each waveguide branch but also place the same degree of the phase at the same spatial locations from the input source. Thirdly, both structures require optical phase tuning components that are placed at certain locations of waveguide branches. This is because asynchronous phases may be adjusted by a fabrication error or by applying a certain phase delay on each adjacent branch to maximize the performance of each structure. Finally, both structures must minimize the signal crosstalk between adjacent branches near the output ports.

1.4 Thesis overview

These four requirements have been considered concerning designing and fabricating both OPA LiDAR structures and expandable waveguide-array DLA structures. In this thesis, we present the completed designs of new silicon nitride (Si3N4) and silicon hybrid OPA LiDAR structures and new hybrid waveguide-array DLA structures. In Chapter 2, we study the basic theories of OPA, the mechanisms of the laser-induced damage threshold of optical materials with near-infrared (NIR) sub-picosecond lasers, the principle of minimizing the signal crosstalk of E-skid waveguides, and the principle of waveguide array minimizing the phase space overlap. In Chapter 3, we introduce the full layouts for the newly proposed designs of both the LiDAR and the DLA structures and explain in detail each component of these devices. In Chapter 4, we discuss the fabrication challenges that we confronted when fabricating new devices and show how we resolved those challenges. In Chapter 5, we present the experimental setups and test results from the newly fabricated devices and estimate their simulation results. Finally, in Chapter 6, we conclude and provide future works.

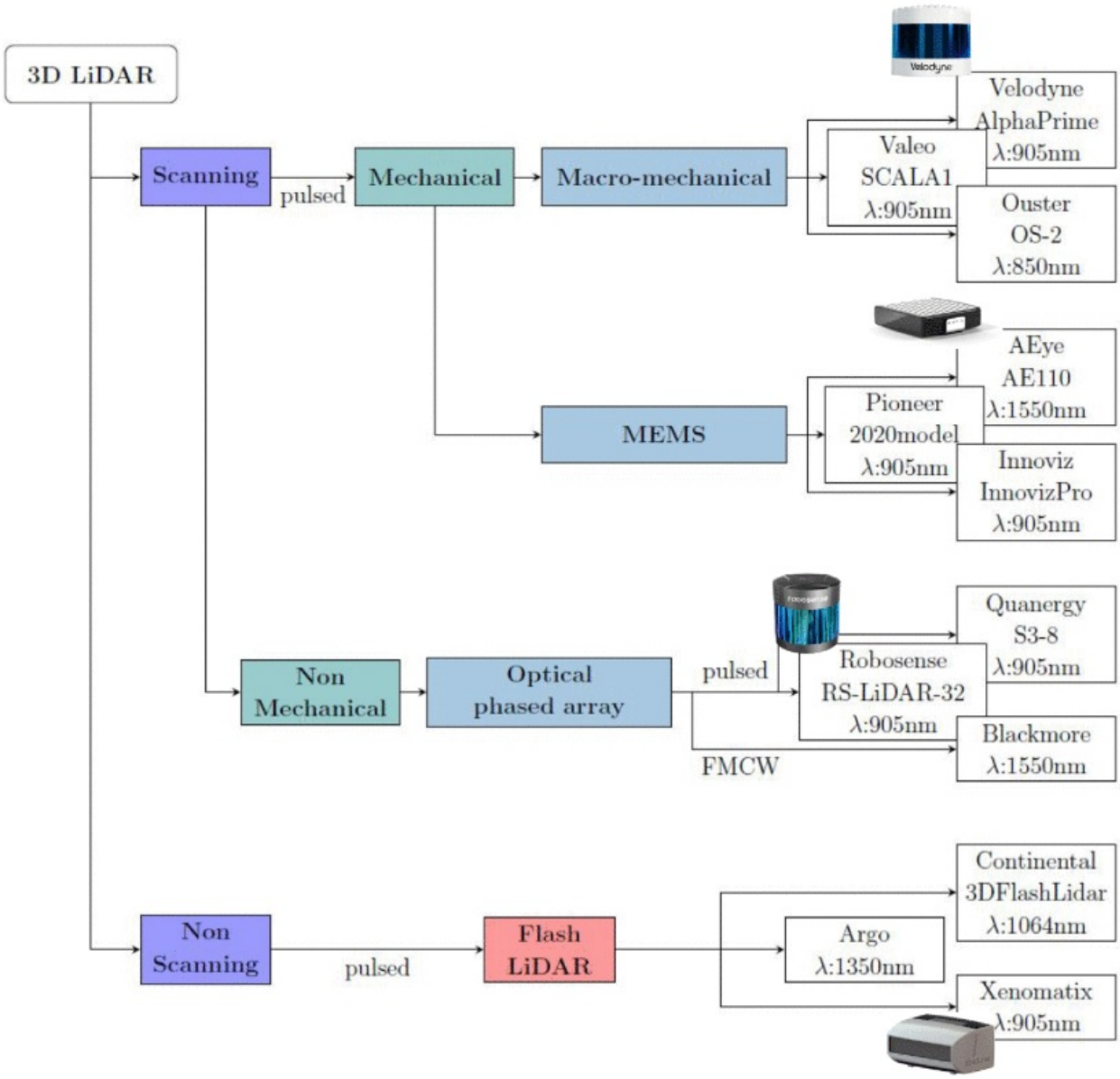

Figure 1.2. A diagram of the different technologies used for automotive 3D LiDAR sensors [1].

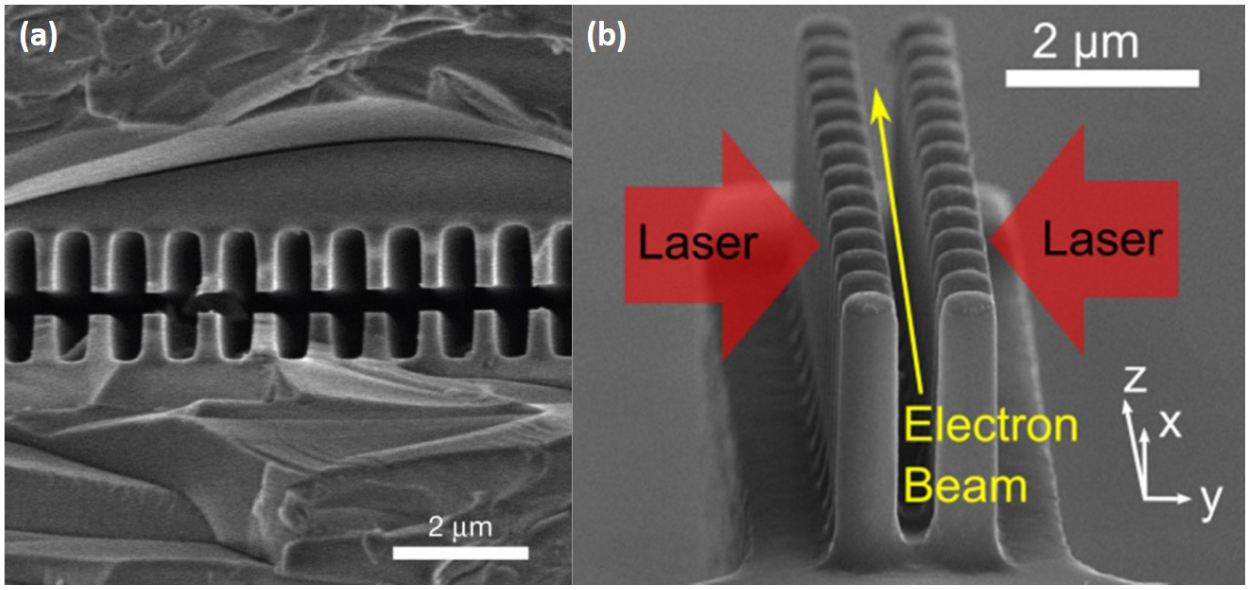

Figure 1.3. (a) Scanning electron microscope (SEM) image of the fused silica dual pillar structure for the DLA acceleration in a relativistic regime using [6]. (b) SEM image of the silicon dual pillar structure for the DLA acceleration in a sub-relativistic regime [10]

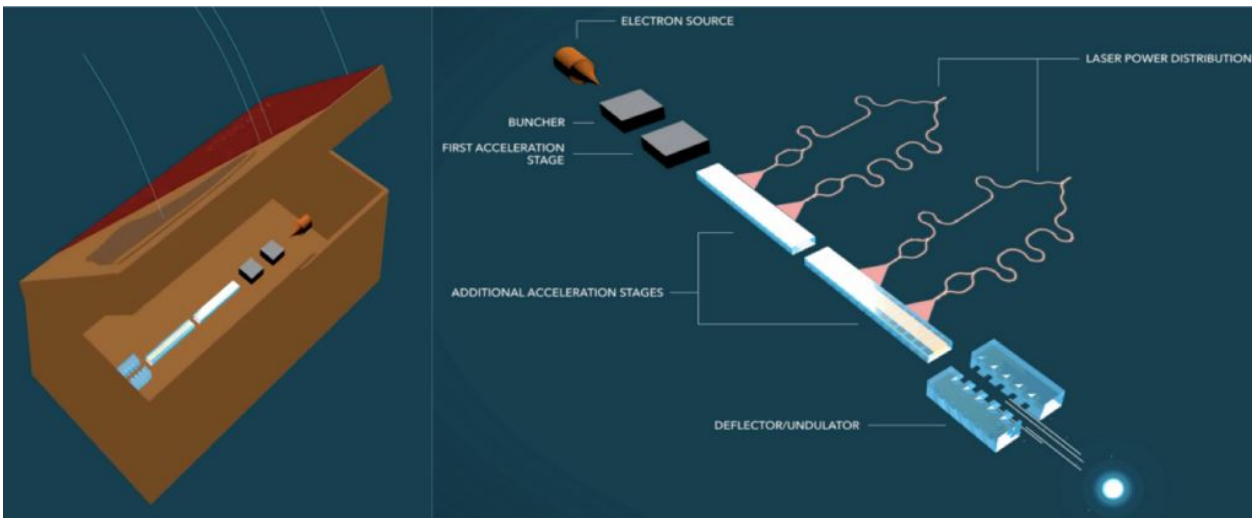

Figure 1.4. Shoebox-sized dielectric laser accelerators, proposed by ACHIP

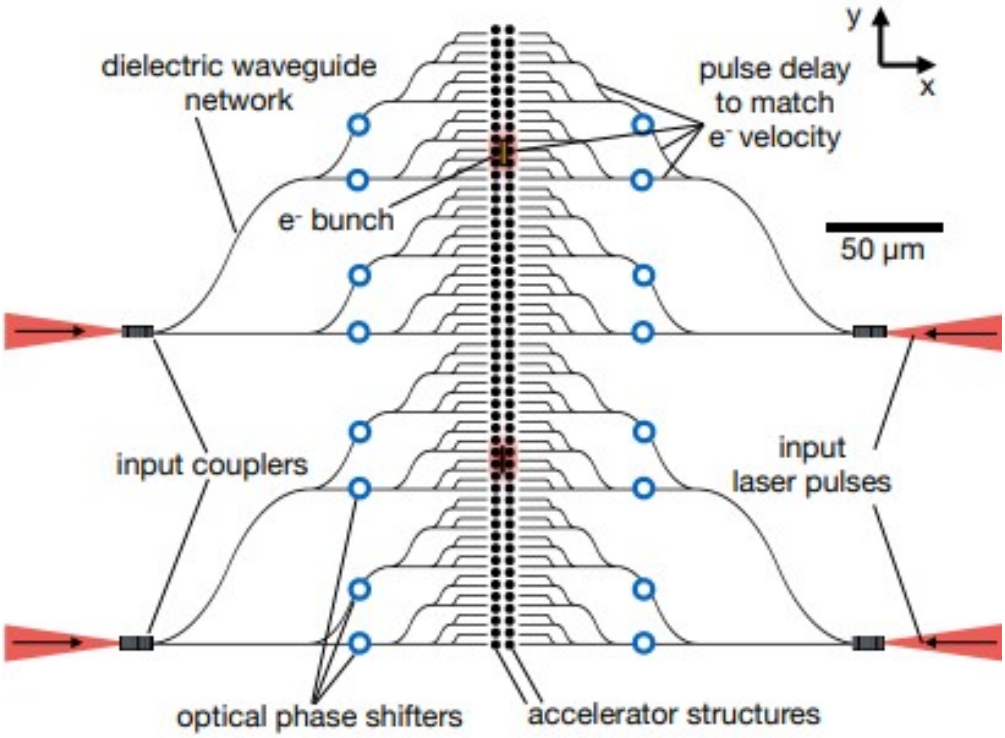

Figure 1.5. Two stages of the DLA laser coupling tree-network structure. The electron beam travels along the z-axis through the center of the structure and the laser pulses (in red) are coupled on each side [11].

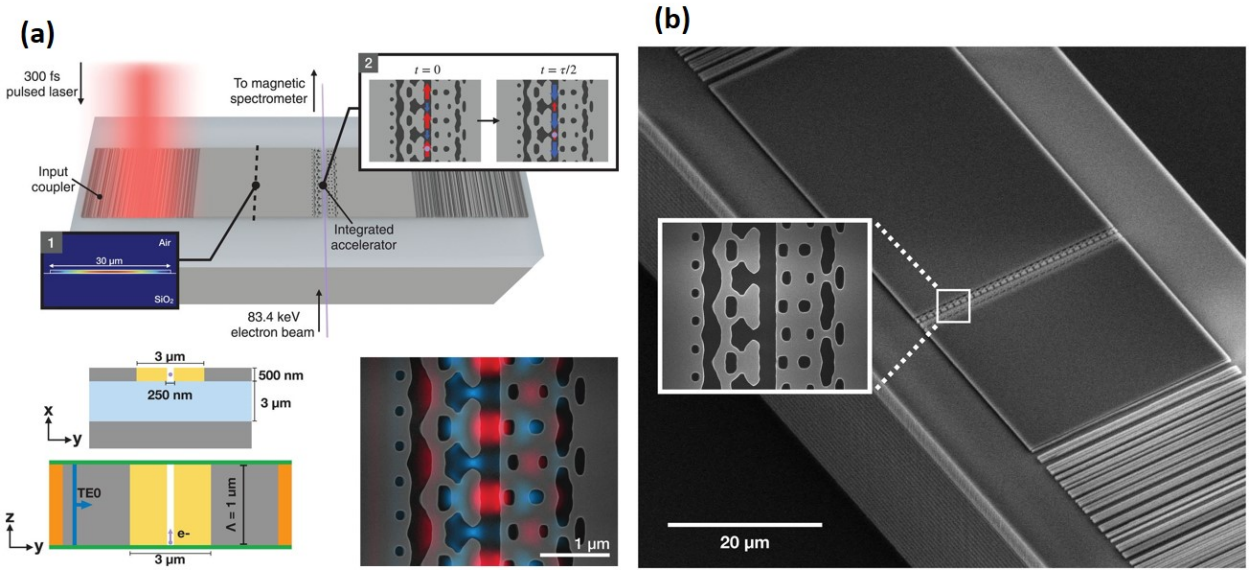

Figure 1.6. (a) Schematic illustrations of a silicon-based on-chip accelerator. Once the free-space pulsed laser coupled by the silicon's grating coupler and excited single mode was in a slab waveguide, the accelerator structure designed using an inverse design technique produced near fields that were phase-matched to an input electron beam with initial energy of 83.4 keV. (b) SEM image of silicon-based on-chip accelerator [12].

2. LITERATURE AND THEORETICAL REVIEW

In this chapter, we study basic concepts and theories required to understand the working principles of applicable devices. Since new LiDAR and DLA devices include several common components that can outperform conventional devices, we must understand the physical mechanisms of those components. Firstly, we study in detail the physical mechanisms of OPA to understand how this structure can generate desired far-field patterns and steer its beam, and what conditions are required for beam scanning applications. Secondly, we discuss the working principle of the DLA structure driven by optical frequency and describe how the acceleration gradient and energy gain can be calculated using this. We then closely examine the structural properties and summarize the study of NIR laser-induced damage threshold (LIDT) of optical materials that typically consist of on-chip waveguide structures. Additionally, minimizing the optical crosstalk between the small pitch-sized adjacent waveguide array is crucial . In this chapter, we also deal with two special techniques whereby the small pitch-sized waveguide array minimizes signal crosstalk while the power is transmitted through the long distance with a dense array. One is called an e-skid waveguide and the other is called a phase space mismatched waveguide array. We discuss the working principles of these waveguide array techniques.

2.1 Mechanisms of OPA

A phased array is a technique to create a beam of coherent electromagnetic waves from the surface of an antenna array and steer the beam to the point in different directions without moving any emitter structure. OPA is this same technique operating in optical frequency instead of RF. On-chip waveguide structures have the potential to deliver and steer the phased array beam of optical frequency; the waveguide array structure can be designed to deliver the individual wavefront to the surface antenna array without any degradation or phase distortion. A cascaded array dielectric waveguide system is an essential component of the OPA-based on-chip LiDAR emitter as it is the most efficient way to guide and distribute power into the arrayed-grating structures at the end, neglecting losses of power and phase coherence with each arrayed waveguide. With this cascaded waveguide system, beamforming

and azimuths angle steering can be achieved by applying the same amount of phase shifting in each waveguide array, as in Figure 2.1 (a) illustrated.

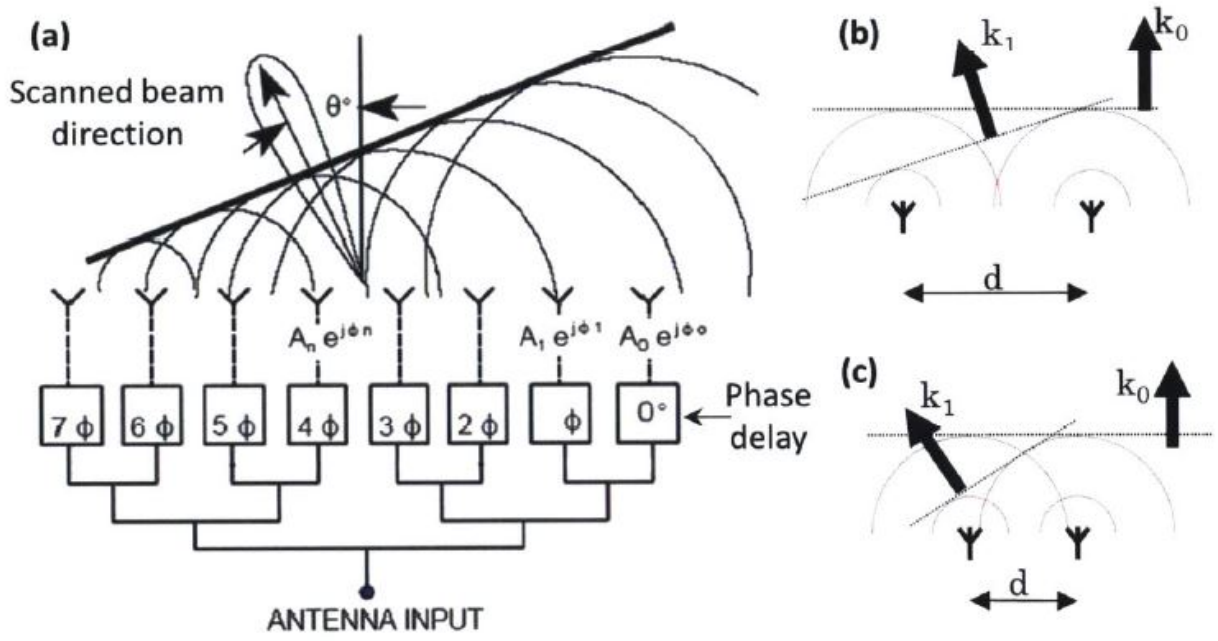

Figure 2.1. Illustration of OPA basics: (a) Schematic illustration of a beam steering with a different phased array. (b-c) Illustration of higher orders emitting from a phased array and their dependence over antenna pitch [13]

If the phase difference, $\Delta\phi$, of each adjacent waveguide can be controlled and applied and the electromagnetic wave transmitted out from each emitter array, the beam (particularly the first constructive interference, which is called the main lobe) can be tilted by the angle of θ with the following relationship:

$$\sin\theta = \frac{\lambda\Delta\phi}{2\pi d} \tag{2.1}$$

where λ refers to the input wavelength and d refers to the spacing between each of the emitters. However, if these phase differences were applied each of the emitter , higher orders of constructive interference (called the grating lobes) are presented with a different angle

θ_n, as in Figure 2.1 (b) and (c). These higher orders of angle differences can be varied by d value using the below equation:

$$\sin\theta_n = \frac{\lambda(\Delta\phi + 2n\pi)}{2\pi d} \tag{2.2}$$

where the angular separation between the main lobe and the higher orders of grating lobes can be increased once the d value decreases. If $\Delta\phi = \pm\pi$ inserted into both equation 2.1 and 2.2, so the range of the main lobe is steerable without using visible grating lobes, which calls an unambiguous beam steering range, then the θ_0 can be driven by:

$$-\sin^{-1}\left(\frac{\lambda}{2d}\right) \leq \theta_0 \leq \sin^{-1}\left(\frac{\lambda}{2d}\right). \tag{2.3}$$

. Based on this limitation, if the space between the emitter array, d, is in the range of $d \leq \lambda/2$, the unambiguous main lobe beam steering range would be $-90° \leq \theta_0 \leq 90\circ$, which is a 180° of full range above the surface of emitter array.

The far-field beam width should be considered for the optical beam resolution. It can be calibrated as an angle broadening at full-width half maximum (FWHM) of the power of the main lobe, $\Delta\theta_{3dB}$, and this can be expressed as follows [14]:

$$\Delta\theta_{3dB} = \frac{c1}{\sin\theta_0}\frac{\lambda}{Nd}, \tag{2.4}$$

where N is the nmuber of emitters and c_1 is a constant of beam profile of main lobe. To get the free-steering range of the main lobe, the emitter spacing value, d, should be limited as $d \leq \lambda/2$; thus, the number of emitters should be sufficient to increase its spatial resolution. Hence, keeping the spacing of emitter array with $d \leq \lambda/2$ and increasing the number of emitter arrays are essential for improving the quality of OPA-based LiDAR devices. Fully operational on-chip OPA structures require five components: an input coupler, cascaded power splitter, phase tuner, recombiner, and emitter array. Usually, the input coupler consists of the inverse taper waveguide and the power splitters consist of the cascaded branches of 1 x 2 Multimode Interferometers (MMI) due to their ability to split the same phase outputs. The phase tuners

are usually used as micro-heaters that deposit on top of the waveguide's array . The typical on-chip OPA structure is presented in Figure 2.2 [15].

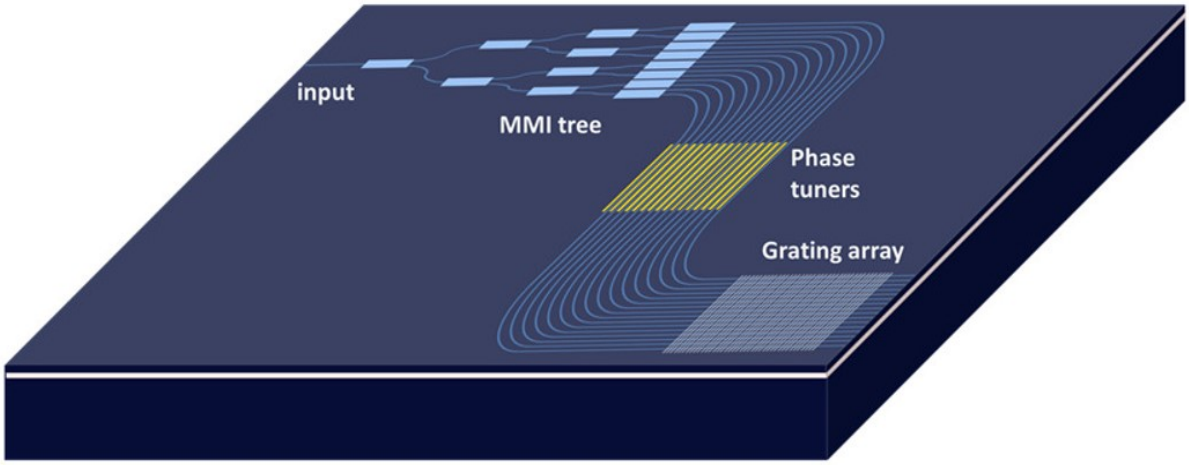

Figure 2.2. Schematic diagram of a typical on-chip OPA structure [15]

2.2 Theory and operation of DLAs

Dr. Neil Spara, a member of ACHIP, derived the mathematical formula for the acceleration gradient and its phase-matching conditions by near-field illumination from a single periodic structure [12], [16]. Since the development of nanofabrication technology, DLAs have utilized the near-field of sub-micrometer-sized periodic structures, such that these fields are phase-matched to electrons of a specified velocity, $v = \beta c_0$, where c_0 is the speed of light in vacuum and β is the ratio of v to c_0. To explain the phase-matching conditions and the acceleration gradient of DLAs, we consider a certain dielectric structure that consists of a periodic structure with its period of Λ surrounding the electron's trajectory channel, with an electron traveling in the +z-direction. We illuminate the structure with the electromagnetic waves propagating in the +y-direction with the electric field polarized in the z-direction. In this case, the acceleration gradient, G, of an electron over a single period of the structure can be described as follows:

$$G(x, y; s) = \frac{1}{\Lambda} \int_{\Lambda/2}^{\Lambda/2} E_z(x, y, z; t = (z + s)/\beta c_0)\, dz \ , \tag{2.5}$$

where the time coordinate can be written by the motion of an electron traveling at velocity $v = \beta c_0$ through the cell with trajectory $z(t) = \beta c_0 t - s$ where s is an arbitrary initial position where the electron entering the periodic cell [16]. This equation can be expressed by the complex harmonic electric field of $E_z(x, y, z; t = (z + s)/\beta c_0) = \tilde{E}_z(x, y, z; \omega)\mathrm{e}^{\mathrm{i}\omega z/\beta c_0}\mathrm{e}^{\mathrm{i}\omega s/\beta c_0}\}$, and we obtain

$$G(x, y; s) = \frac{1}{\Lambda}\int_{\Lambda/2}^{\Lambda/2} Re\{\tilde{E}_z(x, y, z; \omega)\mathrm{e}^{\mathrm{i}\omega z/\beta c_0}\mathrm{e}^{\mathrm{i}\omega s/\beta c_0}\}\, dz\ . \tag{2.6}$$

Given the periodicity in the z-direction of the DLA structure, we can express the spatial field in terms of the Fourier-series

$$\tilde{E}_z(x, y, z; \omega) = \sum_{m=-\infty}^{m=\infty} \tilde{\mathrm{e}}_m(x, y; \omega)\mathrm{e}^{-\mathrm{i}m\frac{2\pi}{\Lambda}z}, \tag{2.7}$$

where

$$\tilde{\mathrm{e}}_m(x, y; \omega) = \frac{1}{\Lambda}\int_{\Lambda/2}^{\Lambda/2} \tilde{E}_z(x, y, z; \omega)\mathrm{e}^{-\mathrm{i}m\frac{2\pi}{\Lambda}z}\, dz\ , \tag{2.8}$$

represents the complex amplitude for the m-th diffraction order. With the spatial field represented in the Fourier expansion, the expression for the acceleration gradient in equation 2.6 can be obtained:

$$G(x, y; s) = Re\{\mathrm{e}^{\mathrm{i}\omega s/\beta c_0}\sum_{m=-\infty}^{m=\infty} \tilde{\mathrm{e}}_m(x, y; \omega)\mathrm{e}^{-\mathrm{i}2\pi(\frac{1}{\beta\lambda_0}-\frac{m}{\Lambda})}\} \tag{2.9}$$

where λ_0 is a free-space central wavelength illuminated into the periodic structure. For maximal energy gain, the condition of $\frac{1}{\beta\lambda_0} - \frac{m}{\Lambda}$ should be zero, so that the phase-synchronous acceleration condition on the accelerator period would be

$$\Lambda = m\beta\lambda_0. \tag{2.10}$$

For the waveguide arrayed DLA system with guiding the quasi-TE_0 mode, the m should be 1 for the largest amplitude, and if the electron and fields are taken to be in-phase, we obtain a final expression of the acceleration gradient in the frequeny-domain as:

$$G(x,y;s) = |\tilde{e}_m(x,y;\omega)| = \frac{1}{\Lambda}\Big| \int_{\Lambda/2}^{\Lambda/2} \tilde{E}_z(x,y,z;\omega) e^{-i\frac{\omega z}{\beta c_0}}\, dz \Big|. \tag{2.11}$$

2.3 Theory of determining LIDT of optical dielectric materials

The LIDT is an important characteristic to consider regarding the design material when fabricating a dielectric optical waveguide as it relates to the waveguide's power handling capability . Each optical material has a threshold value concerning the wavelength and the pulse width of the incident laser [17]. We investigated the LIDT of some optical materials usually used for on-chip waveguide structures and the results were presented in my thesis for Master of Science, December 2017 [17].

The term LIDT refers to irreversible changes to a material's structure due to the critical power or peak influence of the laser incidence [18]. Damage can occur in various ways depending on what kind of material it is, the range of the pulse width, and the peak intensity of the electric field of the incident laser [19]. For an incident laser with sub-picosecond and high-peak electric field intensity (about $10^{12} \sim 10^{13}\ W/m^2$), the damage occurs when plasma frequency from free electron density in the conduction band of the material resonates with the incident laser frequency [20]. The plasma frequency relates to the inverse-square of the electron density in the conduction band (n_e). We can describe its relationship as follows [20].

$$\omega_l = \omega_p = \sqrt{\frac{n_e e^2}{\epsilon_0 m^*}}. \tag{2.12}$$

Here, ω_l and ω_p refer to the incident laser frequency and the plasma frequency respectively. Also, ϵ_0 and m^* refer to electron permittivity and electron's effective mass respectively. For the damage occurred with the incident laser that has sub-picosecond, near-IR range, the value of n_e is around $10^{20} - 10^{21}\ cm^{-3}$ [17], and n_e that satisfies the equation 2.12 is called the plasma density.

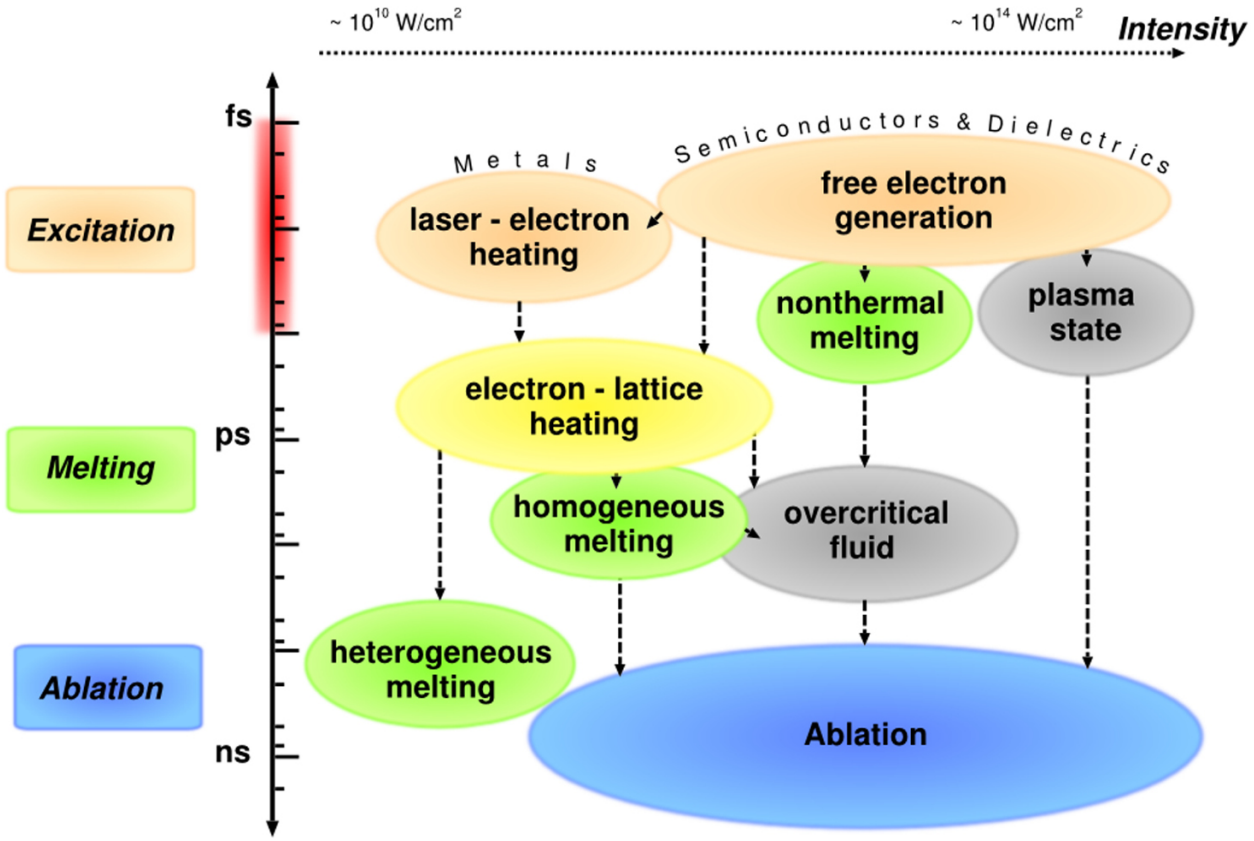

Figure 2.3. Typical timescales and intensity ranges of several phenomena and processes occurring during and after irradiation of a solid with an ultrashort laser pulse of approximately 100 fs duration [19].

Based on this damage occurrence mechanism, the damage threshold by laser pulse incidence can be estimated by how quickly the electron density in the conduction band reaches the plasma density from the laser. For dielectric optical materials with an incident laser with sub-picosecond pulse duration and NIR range, three mechanisms are dominantly involved with the damage: photoionization, avalanche ionization, and relaxation effect [17]. Thus, the total rate of change of the electron density in the conduction band can be described as follows:

$$\frac{dn_e}{dt} = K(I) + A(I, n_e) - \frac{n_e(t)}{T} \tag{2.13}$$

where the first term, $K(I)$, is the Keldysh's photoionization rate, and the second one, $A(I, n_e)$, refers to the avalanche ionization rate, and the third one, $-\frac{n_e}{T}$, represents the rate of relaxation from the conduction band to the valence band [20]. Equation 2.13 can be

rewritten with respect to the term of $I(t)$ to see the relationship between the peak intensity of electric field and the rate of n_e, thus,

$$\frac{dn_e}{dt} = \sigma_k I(t)^k + \alpha I(t) n_e(t) - \frac{n_e(t)}{T}, \tag{2.14}$$

where σ_k is the multiphoton absorption coefficient with the number of k photons, and k can be determined by the smallest number which satisfies the relation $k\hbar\omega \geq E_g$ [17], [21], [22]. Also, α is defined as a coefficient of avalanche ionization, and T refers to the relaxation time constant. If the equation 2.14 would be solved with n_e, and once the number of electron density in the conduction band is around the range of $10^{20} - 10^{21}\ cm^{-3}$, the damage threshold of specific materials and incident lasers could be estimated with respect to the peak power of electric field intensity[17]. Based on the equations 2.13 and 2.14, we can run the simulation and obtain a result regarding the damage threshold of the power density of the incident laser pulse, once we have information regarding the central wavelength, the pulse width of the incident laser, and the coefficient values of each optical materials' properties. In the journal of Dr. Mark Mero published in 2005, the parameters of several dielectric materials are presented, given by the experimental value [23]. For the LIDT estimation of silicon dioxide, SiO_2, from the laser pulse with 2 μm of its central wavelength and 300 fs of its pulse width, the number of photons for multiphoton ionization rate, k, is 8, based on the calculation of the band gap energy of SiO_2, which is 8.3 eV, divided by its photon energy, which is $\lambda = 2\mu m$, and the ratio between the effective mass and the original mass of electron in the SiO_2 is 2.2. Also, the value of α is 8 cm^2/J, and the value of T is 220 fs, from the Dr. Mark Mero's experimental result [23]. Thus, we can calculate Keldysh's photoionization rate, avalanche ionization rate, and relaxation rate, and finally we can calculate the LIDT value of SiO_2 as 4.35 J/cm^2 from the calculated value of the intensity of peak pulse.

We also measured the LIDT values with the damage threshold tests with the optical materials to see whether the values matched our calculations. Five representative optical materials: silicon (Si), silicon dioxide (SiO_2), silicon nitride ($Si_3\ N_4$), aluminum oxide (Al_2O_3), and lithium niobate ($LiNbO_3$), had been measured for each specific value of laser-induced damage threshold at the sub-picosecond (approximately 300 fs), NIR (1550 nm and 2000

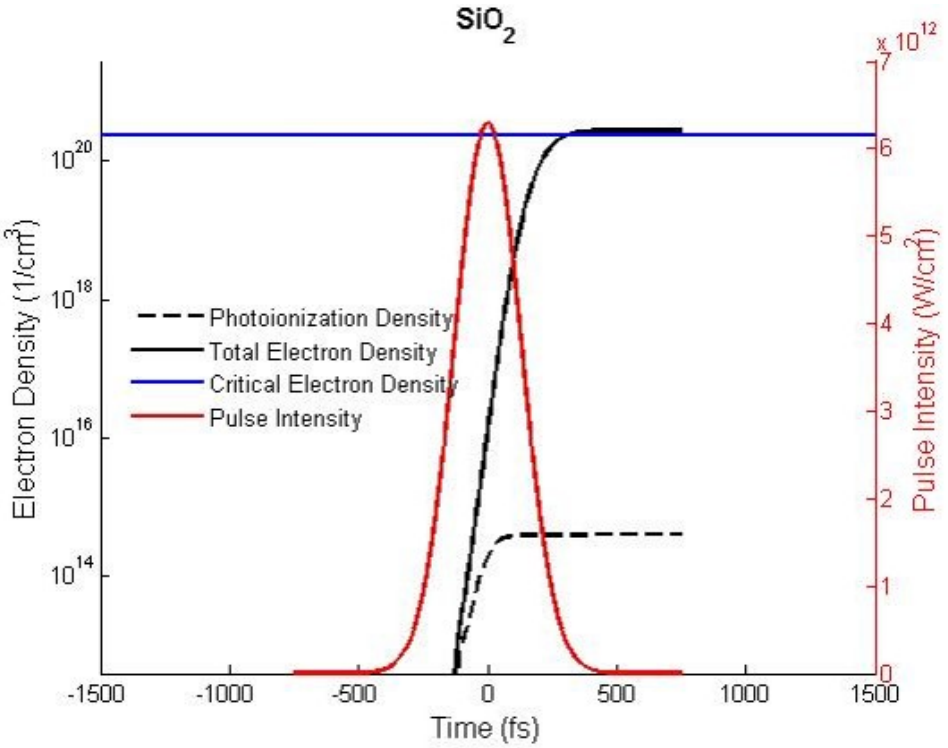

Figure 2.4. LIDT simulation result of SiO_2 of the incident laser of $\lambda = 2\mu m$ and 300 fs of pulse width. Pulse intensity has been calculated once the total electron density reached $10^{21} cm^{-3}$, derived from the equations 2.13 and 2.14 [23].

nm), and at the high repetition rate (10 kHz) irradiation. These are specific requirments for operating the DLA structures for generating acceleration gradient. These materials and laser specifications are potentially adaptable with the input source of LiDAR devices and optical interconnect modulators; thus, these measured results could be indicative of maximum power handling operation levels.

Table 2.1 shows the results regarding these laser characteristics with silicon (Si), silicon dioxide (SiO_2), aluminum oxide (Al_2 O_3), and lithium niobate ($LiNbO_3$). These materials were prepared by bulk substrates and were cleaned with RCA cleaning, which is the standard cleaning process in the semiconductor industry.

For the LIDT testing with the silicon nitride, a film deposition process was necessary. Thus, the stoichiometric silicon nitride (Si_3N_4) samples were prepared using the low-pressure chemical vapor deposition (LPCVD) process to be deposited on top of the quartz substrate,

Table 2.1. LIDT value of Si, SiO_2 (fused silica), Al_2O_3, and $LiNbO_3$ with different pulse characteristics [17]

Materials	800 nm, 700 fs, 1 kHz	1550 nm, 300 fs, 10 kHz	2000 nm, 300 fs, 10 kHz
Si	0.195 ± 0.013 J/cm^2	0.170 ± 0.005 J/cm^2	0.168 ± 0.006 J/cm^2
SiO_2	2.53 ± 0.190 J/cm^2	1.616 ± 0.197 J/cm^2	1.494 ± 0.100 J/cm^2
Al_2O_3	N.A.	N.A.	1.539 ± 0.225 J/cm^2
$LiNbO_3$	N.A.	0.726 ± 0.039 J/cm^2	0.617 ± 0.057 J/cm^2

which has a much higher LIDT value than silicon nitride materials and thus prevents damage to the substrate prior to the damage of the film materials. To see the LIDT value differences with the different film thicknesses, the Si_3N_4 film deposited different thickness, from 50 nm to 600 nm, which is the typical range of guiding fundamental TE mode of Si_3N_4 waveguides. The results are shown in Table 2.2. However, LIDT value differences between the different film thicknesses were not clearly observed in this experiment.

Table 2.2. LIDT values of stoichiometric silicon nitride (Si_3N_4) with different thicknesses [17]

Thickness of Si_3N_4 on quartz	1550 nm, 300 fs, 10 kHz	2000 nm, 300 fs, 10 kHz
600 nm	0.604 ± 0.21 J/cm^2	0.459 ± 0.22 J/cm^2
385 nm	0.607 ± 0.11 J/cm^2	0.458 ± 0.10 J/cm^2
200 nm	0.648 ± 0.02 J/cm^2	0.647 ± 0.04 J/cm^2
100 nm	0.629 ± 0.05 J/cm^2	0.536 ± 0.09 J/cm^2
50 nm	0.601 ± 0.06 J/cm^2	N.A.

Overall, LIDT values of Al_2O_3 were slightly higher than those of SiO_2, approximately four times higher than those of Si_3N_4 and $LiNbO_3$, and 9 times higher than those of Si.

2.3.1 Experimental demonstrations of LIDT of dielectric waveguide structures

Based on the LIDT information of stoichiometric silicon nitride, Si_3N_4, we studied the laser damage threshold and the power handling capabilities of weakly-guided silicon nitride waveguide structures. [24].]. This work contained not only the damage fluences but the

nonlinear phase shift and self-phase modulations, which are critical factors to handling the high-power guidance with the coherent phase. The Si_3N_4 weakly-guided waveguides consisted of 60 nm of its thickness (deposited by LPCVD process), 5.9 μm of its width, and was sandwiched by 30 μm of thick SiO_2 cladding layer.The edge of the chip was finely polished via a chemical-mechanical polishing (CMP) process. The testing setup was established using the same laser source system for the bulk materials' damage threshold testing, and had a similar setup except the chip mounting stage and the output collimating lens had information concerning the power coming from the waveguide structure, as in Figure 2.5 (a). The result of this experiment shows on Figure 2.5 (b): the maximum fluence that Si_3N_4 waveguide can deliver was $\sim$ 0.19 J/cm^2, which was lower than the measured the film of Si_3N_4 ($\sim$ 0.65 J/cm^2) [24]. This $\sim$ 0.19 J/cm^2 of damage fluence corresponds to approximately 27 nJ, the maximum pulse energy that could be delivered through this waveguide. This lower damage fluence of the end-fire coupling than that of the film of Si3N4 was because the imperfect coupling from free-space to the waveguide presented additional surface defects on the input facet [24]. Thus, Thus, if we had used the inverse taper on the side, the fluence on the input facet may have been smaller [24]. To investigate where the damage initially happened on the waveguide, we increased the power to over the maximum output fluence of $\sim$ 0.19 J/cm^2. We observed through the optical microscope that the damage occurred in the waveguide core near the input facet at the fluence of approximately $\sim$ 1.0 J/cm^2, which is below than the damage threshold of SiO_2 [24] (see Figure 2.5 (c)).

Furthermore, we demonstrated the nonlinear properties of Si_3N_4 by measuring the power spectra of the transmitted pulses under various input power levels and propagation lengths through the optical spectrum analyzer (OSA) system that can detect the power transmission spectrum [24]. Figure 2.6 shows the output spectra for the 6 mm of the waveguide and indicates that the spectral variance is negligible when the transmitted pulse energy is below $\sim$ 15 nJ for 6 mm propagation length. This means that the waveguide length should be less than 3 mm if the waveguide operated around maximum power regions ($\sim$ 27 to 30 nJ) [24].

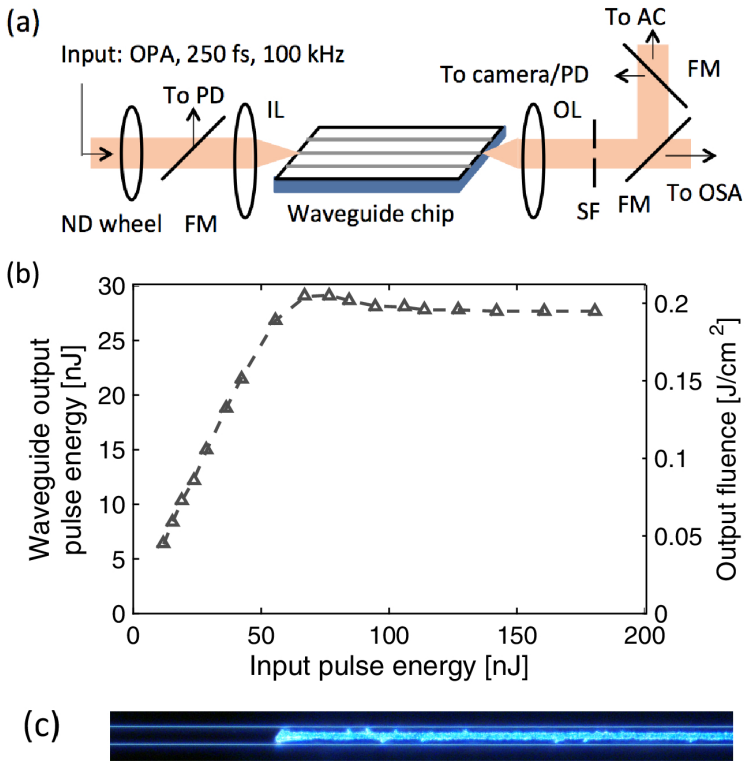

Figure 2.5. (a) Experimental setup of waveguide power handling test (b) Waveguide output vs.free-space input. Waveguide shows damage when output energy reaches 27 nJ (fluence of 0.19 J/cm^2) [17]

2.4 E-Skid waveguide

As discussed previously, both OPA-based LiDAR devices and waveguide integrated DLA structures minimize signal crosstalk between the adjacent branches near the output ports. Crosstalk is defined as a phenomenon whereby any signals transmitted on one channel generate unwanted effects to other channels nearby. In an on-chip photonic waveguide, the waveguide crosstalk is the power and phase interference from the adjacent waveguide due to the evanescent waves. The easiest way to avoid crosstalk is simply to make the space between the waveguides large enough so that each transmitting signal does not receive interference via evanescent waves from another one. However, this limits photonic chips' dense integration and loose a figure of merit of photonic device. For example, in OPA-based LiDAR structures, it would generate higher-order grating lobes if the adjacent waveguides and their output ports were not close enough.

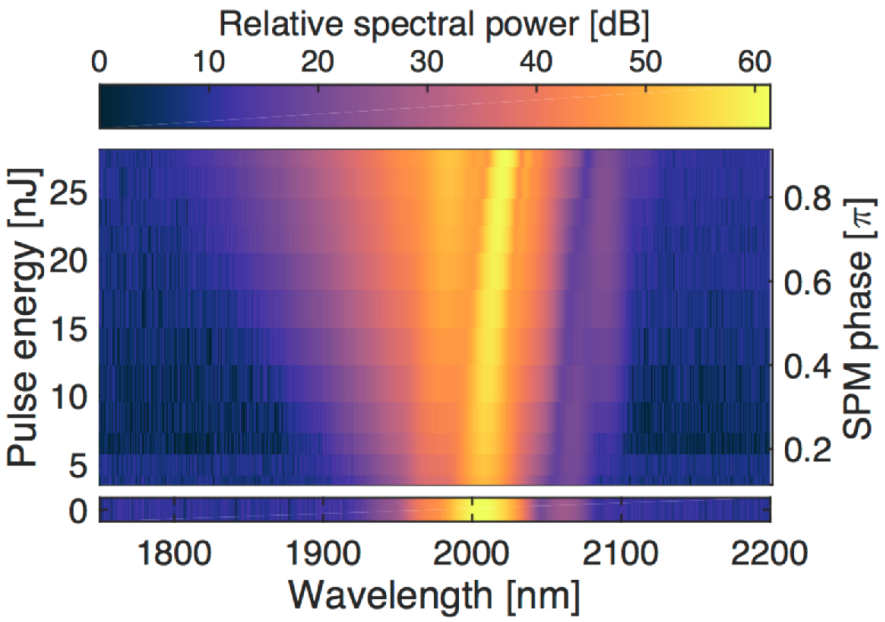

Figure 2.6. Power spectra for a 6 mm waveguide at different output pulse energy. The laser spectrum prior to input into the waveguide is shown in the bottom strip of the figure[17]

For waveguide integrated DLA structures, a higher acceleration gradient cannot be achieved due to the misalignment of phase matching between the light source and the electron trajectory. Both structures require space at least around the sub-wavelength range. The plasmonic waveguide has the potential to reduce crosstalk by sub-diffraction whereby light couples to the free electrons of metals [25]–[32]. However, metal structures standing along with a silicon-on-insulator (SOI) waveguide are not suitable for dielectric multi-stacking structures as such dielectric materials (such as silicon dioxide, SiO_2, and stoichiometric silicon nitride, Si_3N_4) require very high temperatures to deposit on the substrate. Additionally, the large ohmic loss of metals makes it difficult to apply them to the photonic integration [25], [33], [34]. Thus, reducing crosstalk between adjacent waveguides using all-dielectrics at the sub-wavelength range has been investigated for decades. For example, photonic crystal waveguides and slot waveguides instead of conventional strip waveguides were designed for confining the mode. Figure 2.7 illustrates representative dielectric waveguide platforms for light confinement in photonic chips [25]. Figure 2.7 (a) describes a simple strip waveguide, which is the most common type of waveguide for guiding light. In on-chip photonic integra-

tion circuit systems, it is usually composed of a silicon channel surrounded by silicon dioxide so that the light is confined inside the silicon core due to the total internal reflection (TIR) by high refractive index differences [25]. However, tthis type is limited as it becomes reduced in size because the mode size grows larger as the core size is reduced. Figure 2.7 (b)shows a photonic crystal waveguide that can miniaturize photonic circuits more than simple strip waveguides as it can confine more light inside the strip part of the waveguide by using Bragg reflection from the various sizes of holes near the strip side. However, this type of waveguide structure also has the limitation of size reduction for integration or arrayed structures as the periodicity of the Bragg reflectors is on the order of the wavelength [25]. Figure 2.7 (c) shows another method of light confinement, called a slot waveguide. This confines the mode inside the sub-wavelength low-index gap surrounded by high-index dielectric rods [25]. However, this method has an issue with radiation loss at sharp bends in dense photonic-integrated circuits [25].

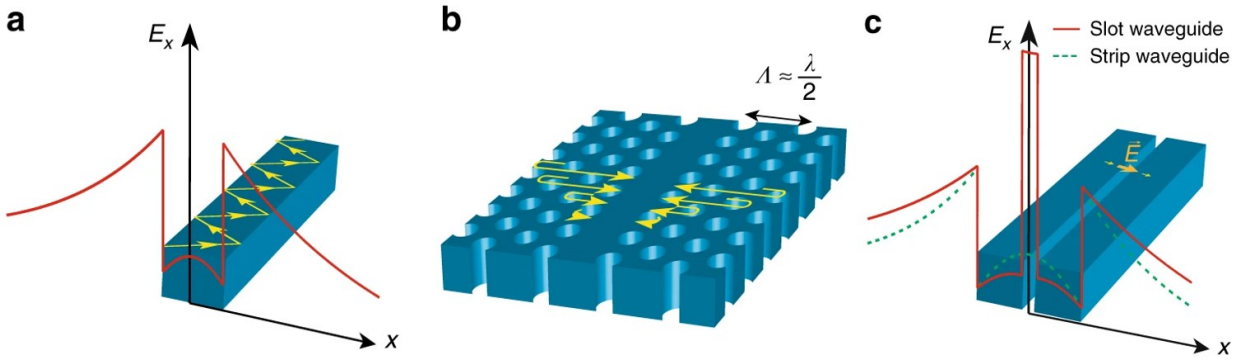

Figure 2.7. Fundamental differences of dielectric waveguides on SOI platform with respect to mode confinement: (a) strip waveguide, (b) photonic crystal waveguide, (c) slot waveguide [25].

Jahani et al. (2018) proposed a new type of all-dielectric waveguide platform with low-loss, high confinement of light, no crosstalk between adjacent waveguides, and CMOS-foundry-compatible dense photonic integration. The proposed design is shown in Figure 2.8. The idea of this new platform was to introduce the anisotropic metamaterials (AMM) in between the adjacent waveguides so that this AMM structure controlled a single component of a dielectric tensor which governed TIR and reduced the decay length of evanescent waves

[25]. This structure was fabricated using a monolithic silicon-on-insulator (SOI) with a thickness of 220 nm and sub-wavelength spacing between the waveguide of 1000 nm operating at 1550 nm of the wavelength. They demonstrated the propagation loss at 3.67 dB/cm and reduced the crosstalk to −30 dB [25].

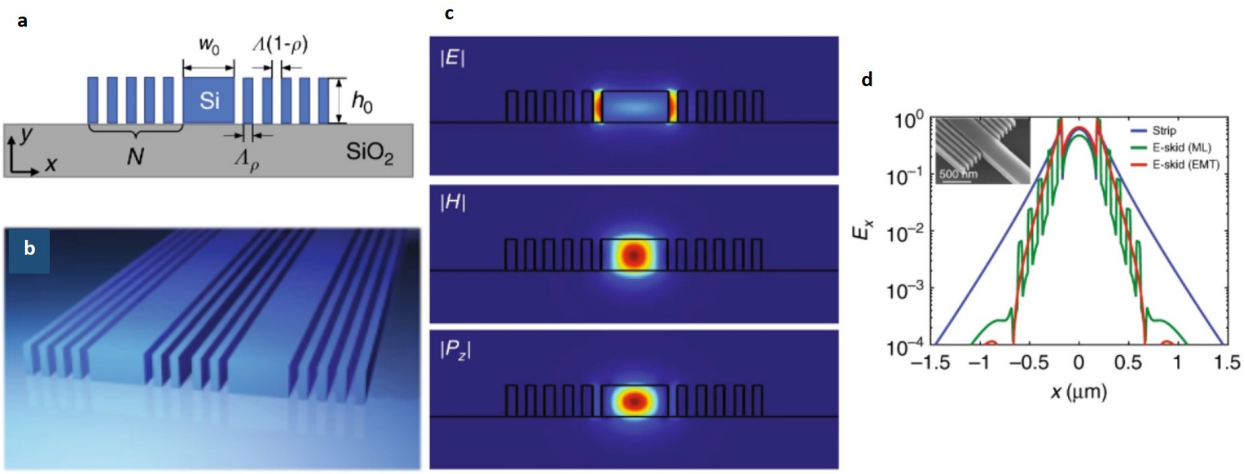

Figure 2.8. (a) Cross-sectional image of on-chip extreme skin-depth (e-skid) waveguides. (b) 3D illustration of e-skid waveguide. (c) Field profile of realistic e-skid waveguide with multilayer claddings (d) The simulated electric field profile at the center of the e-skid waveguide with multilayer (green) and homogenized metamaterial (red) cladding, in comparison with a strip waveguide (blue). Inset shows the SEM image of the fabricated e-skid waveguide [25].

Furthermore, we demonstrated the extreme suppression of crosstalk via exceptional coupling from different field components, resulting in an infinitely long coupling length with the same E-skid structure [35]. The crosstalk between the two adjacent waveguides was determined by the coupling length, L_c, which specified the length that transferred the optical power completely from one waveguide to another. The coupling length corresponded to the free-space wavelength. The L_c of the two identical waveguides could be calculated by:

$$\frac{L_c}{\lambda_0} = \frac{1}{2\Delta n} = \frac{1}{2|n_s - n_a|}, \tag{2.15}$$

where $\Delta n = |n_s - n_a|$ is the magnitude of the index of difference between n_s and n_a, which are the effective refractive index of the symmetric and anti-symmetric respectively. For isotropic media, which are simple, straight waveguides, all the dielectric perturbation components

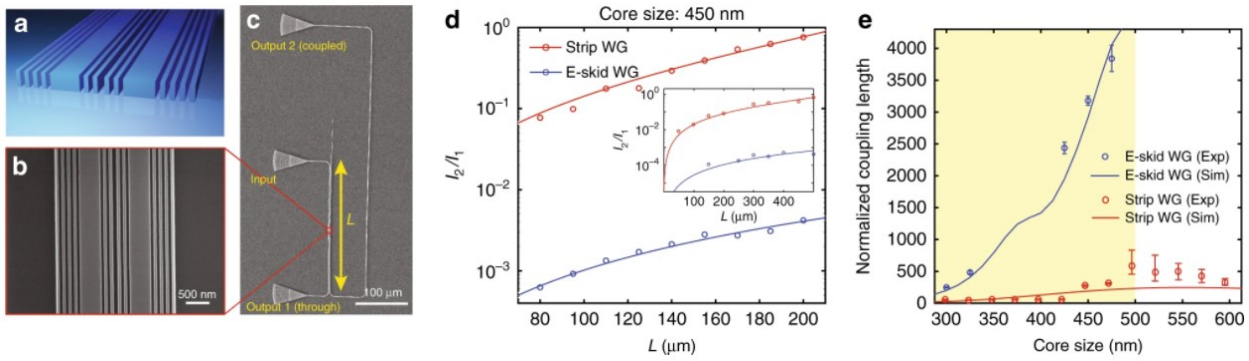

Figure 2.9. (a) 3D illustration of a coupled e-skid waveguide on an SOI platform. (b) SEM image of a fabricated e-skid waveguide. (c) SEM image of the fabricated testing device for measuring the crosstalk between the two waveguides at the telecommunication wavelength ($\lambda = 1550$ nm). (d) The ratio between the measured output power from the strip and e-skid waveguides with respect to the length at $\lambda = 1550$ nm. (e) Comparison of the simulated and measured coupling length for e-skid and strip waveguides [25].

were the same ($\Delta\epsilon_x = \Delta\epsilon_y = \Delta\epsilon_z$); thus, non-trivial coupling regimes (where $n_s < n_a$) were not shown. However, for anisotropic media, which are e-skid waveguides, those components are different ($\Delta\epsilon_x \neq \Delta\epsilon_y = \Delta\epsilon_z$), and this cause the non-trivial coupling regime [35]. Since the coupling coefficients from all the field components (κ_x, κ_y, and κ_z) can be described as:

$$\kappa_{\mathrm{i}} = \frac{\omega\varepsilon_0}{4} \iint \Delta\varepsilon_{\mathrm{i}}(x,y) E_{1\mathrm{i}}(x,y) E^*_{2\mathrm{i}}(x,y) \mathrm{d}x\mathrm{d}y, \tag{2.16}$$

we can describe the overall coupling coefficient $|\kappa|$ by adding each component together ($|\kappa| = |\kappa_x + \kappa_y + \kappa_z|$), and the coupling length of the two same waveguide is:

$$L_{\mathrm{c}} = \frac{\pi}{2|\kappa|}. \tag{2.17}$$

Therefore, these anisotropic dielectric perturbations in the metamaterial mutually cancel the couplings from different field components [35] aand extend the coupling length excessively. We achieved approximately 50 dB of crosstalk suppression, which corresponded to a coupling length approximately 500 times longer than the case of strip waveguides. Figure 2.10 shows the theoretical estimation of different effective refractive indexes of symmetric and

anti-symmetric modes by the strip e-skid waveguides and their coupling length differences. Figure 2.11 shows the experimental results from Purdue University.

2.5 Working principles of phase space mismatched (k-mismatched) waveguide array

In addition to the e-skid waveguide platform for reducing crosstalk between adjacent waveguides, there is another method to design and fabricate the waveguide's array with CMOS-foundry-compatible and dense photonic integration. Instead of manufacturing the AMM between the adjacent waveguides for reducing evanescent waves, it minimizes the coupling mode by minimizing the overlap in the phase space [36], [37]. Since the equation of normalized power coupling from one waveguide to another can be described as:

$$\frac{P_{1\to 2}}{P_1} = \frac{1}{(\Delta\beta/2\kappa)^2+1} sin^2(\sqrt{(\Delta\beta/2\kappa)^2+\kappa^2 L}), \tag{2.18}$$

where $\Delta\beta$ represents the propagation constant difference (or phase mismatch) between two waveeguides, κ the coupling strength and L the propagation distance [36], [38]. If the phase mismatch is large ($\Delta\beta \gg \kappa$), the crosstalk can be minimal. This means that, once we design the cross-section of two adjacent waveguides to have high dispersion ($\partial\beta/\partial\omega$), we can introduce a fairly strong shift of propagation constant and reduce the crosstalk [36]. Therefore, selecting the two different optimized widths of the adjacent waveguides that can have high dispersion makes a waveguide dense array in sub-wavelength scale. We call this dielectric waveguide array platform a k-mismatched waveguide. Christopher T. Phare et al. demonstrated this method to generate silicon OPA with end-fire emission with a 180-degree FoV. They choose a set of 300 nm and 400 nm widths of waveguides to guide the power in a sub-wavelength pitch array [36]. The advantage of the k- mismatched waveguide is that it has much easier fabrication than an e-skid waveguide array, which requires long and narrow fin lines (a thickness range of approximately 30 to 50 nm) to establish the anisotropic media in the narrow gap of the adjacent waveguides.

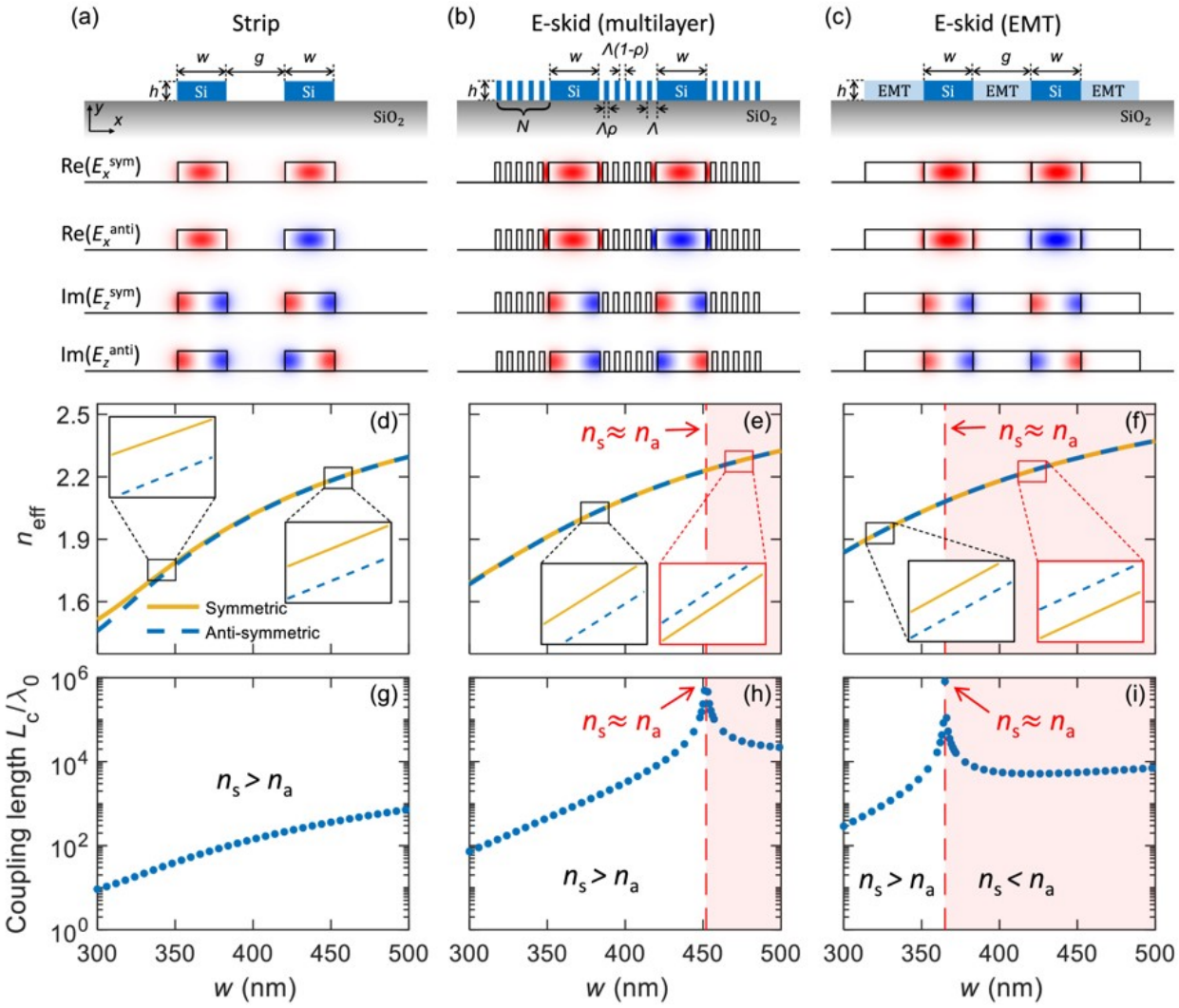

Figure 2.10. On-chip coupled waveguide configurations and exceptional coupling in coupled e-skid waveguides (a)-(c) Illustrations of cross-sectional views of coupled waveguides' geometries and their mode profiles of (a) strip, (b) e-skid, and (c) ideal e-skid with effective medium theory waveguides. (d)-(f) Numerical simulated effective indices of the symmetric ns (yellow solid) and anti-symmetric na (blue dashed) modes followed by the waveguides' geometry of (a)-(c). (g)-(i) Normalized coupling length $L_c/\lambda_0 = 1/(2|n_s - n_a|)$ corresponding with (a)-(c) [35].

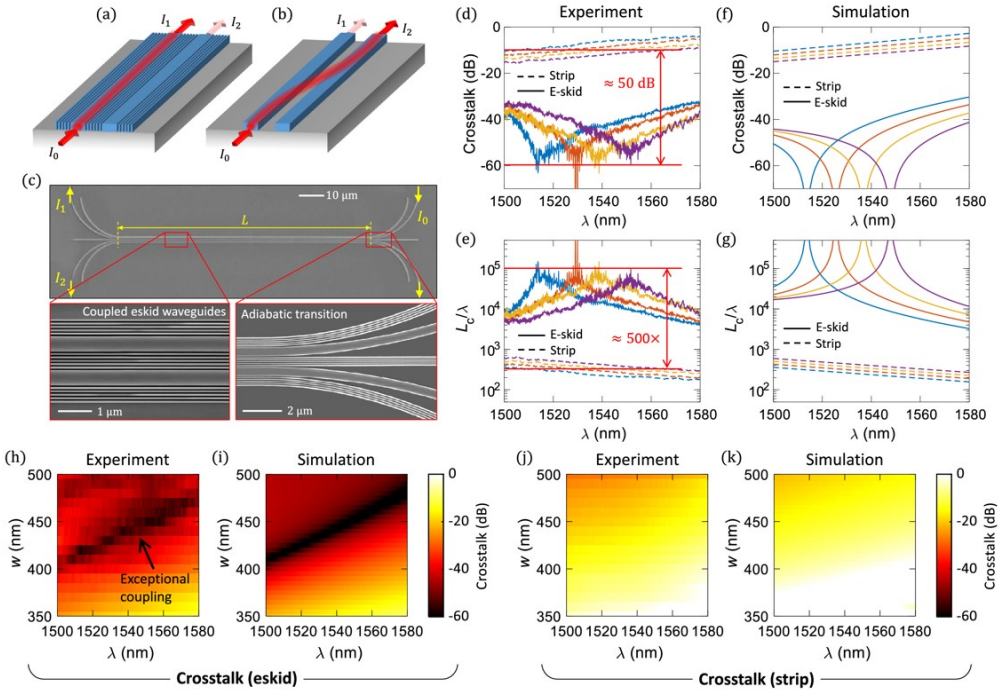

Figure 2.11. Experimental demonstration of the exceptional coupling in coupled e-skid waveguides. Schematic illustrations of the optical power coupled (a) e-skid and (b) strip waveguides. (c) SEM image of the fabricated device for the measurement. (d) Experimentally measured waveguide crosstalk of the fabricated device of (c). (e) Corresponding normalized coupling length of the coupled e-skid (solid) and strip (dashed) waveguides with different widths of waveguides. Results of numerical simulations of (f) crosstalk and (g) normalized coupling length correspond to the experimental results in (d) and (e) [35].

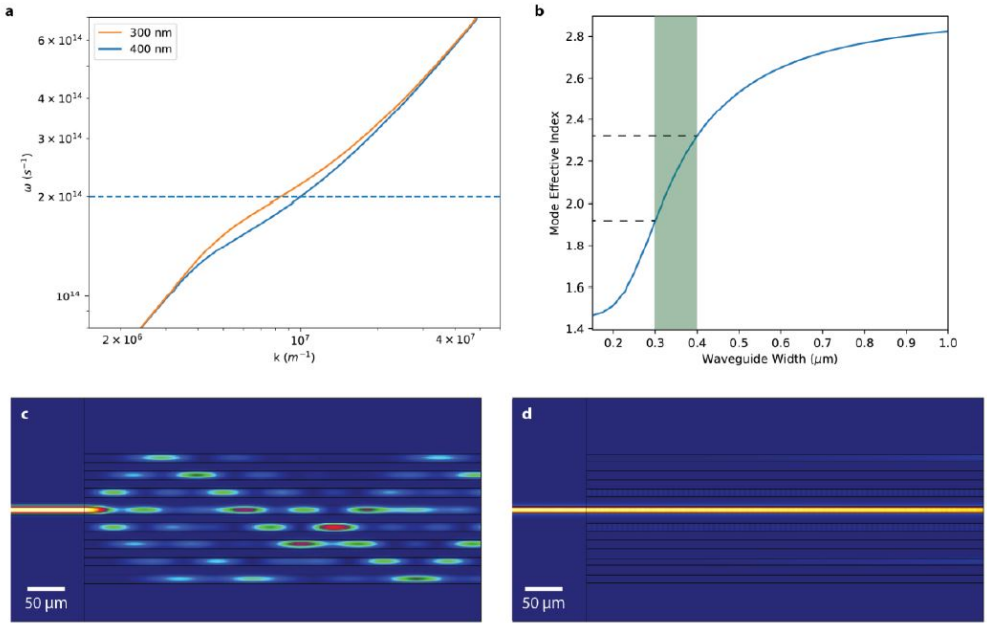

Figure 2.12. (a) A plot of - k dispersion relation for two different widths (300 nm and 400 nm) with 250 nm of the thickness of the Si waveguides. (b) A plot of effective refractive indices of different widths emphasized between 300 nm and 400 nm (green shading). (c) Simulated results of eigenmode expansion of Si arrayed waveguides with equal width of 400 nm on a 775 nm pitch. (d) Simulated results of eigenmode expansion of Si arrayed waveguides with sequentially varying widths of 300, 350, and 400 nm [36].

3. DEVICE AND COMPONENT DESIGNS

We have proposed and demonstrated new OPA-based LiDAR and waveguide-array DLA devices. OPA-based LiDAR requires both aliasing-free beam steering close to a 180-degree FoV and high power of top emission. Waveguide-array DLA must sustain its structure and power delivery system at the sub-picosecond intense pulsed laser and be built on a platform that is easily extendable around a micrometer scale for applying multiple input ports on a chip-scale. This chapter explains the full layouts of the devices that we built and proposes passive and active cases. Additionally, we explain each of the components for those devices. Each component, such as the upper-cladded half-wavelength pitch waveguide array using e-skid and k-mismatched waveguide platforms, silicon nitride (Si_3N_4) to silicon (Si) hybrid waveguide mode converters, and 1x2 and 2x2 multimode interferometer (MMI) structures with both Si_3N_4 and Si for beam splitting and phase switchers, must be optimized for operational wavelength, which is $\lambda = 1550$ nm, so that the devices can perform without additional loss or phase distortion. For waveguide arrayed DLA structures, additional structural components are required, such as Si_3N_4 multi-channel power distributors from apodized grating couplers, racetrack waveguide arrays for group delay lines, and acceleration mode radiation arrays in the electron beam channels.

3.1 Full layouts of OPA-based LiDAR and waveguide arrayed DLA devices

3.1.1 Full layout of OPA-based LiDAR device

To achieve aliasing-free beam steering close to a 180-degree FoV, we needed to place the pitch size of the emitter array with approximately half-wavelength spacing. It is difficult to achieve a pitch size of an array of less than a wavelength using conventional waveguides due to the crosstalk from the evanescent waves, as discussed in Chapter 2. Thus, we put the e-skid fin structures between the emitter arrays. Figure 3.1 describes the first designs for applying an e-skid waveguide array to the grating emitter. Figure 3.1 (a) shows a layout of the 15 e-skid array passive OPA-LiDAR device that was designed for fabricating SOI substrate with a 220 nm silicon film thickness. Once the input laser of continuous-wave

(CW) at the wavelength around the C-band (where is approximately 1530 nm to 1575 nm) with the quasi-TE0 mode coupled with the input Si waveguide (its width was 450 nm), the laser power was distributed by the four-stage cascaded 1x2 MMI splitter tree. One of the channels near the input waveguide was tapped out as output for fiber-to-chip alignment. Once the laser power had split into 16 arrays with 14 μm of spacing, it needed to combine the large-space array into the 775 nm of the half-wavelength spacing array and apply a certain amount of phase delay line. To achieve both of them, the L-shaped delay line combined the 15 channels at the end of the MMI tree with 14 μm spacing to a final spacing of 775 nm [39]. This delay line allowed for tuning of the phase of each line between 0 and 2π by sweeping the input wavelength from 1535 nm to 1575 nm. At the end of the quarter-circled corner of the L-shaped array, each array was applied with e-skid multi-fin cladding on both sides (see Figure 3.1 (b)). This device applied only three fin layers of e-skid due to the relatively short combining region and ease of fabrication. Finally, the passively phase-tuned laser array went through the grating array, as shown in Figure 3.1 (c). For the grating array emitter, we duplicated the emitters and placed them closely packed together on both sides of the emitter parts, which acted as dummy structures, to minimize the proximity effect during the on-beam lithography step. Finally, the device was cladded with silicon dioxide (SiO_2) with 2 μm of its thickness with e-beam evaporator. This was to make a void gap between the fin layers to make a higher refractive index contrast in anisotropic media. To confine the mode in the silicon waveguide, it was covered by uniform materials with a low refractive index. From this structure, we achieved an FoV of more than 140°. The results are explained in detail in Chapter 5.

To ensure successful performance, we designed the device to increase the number of e-skid grating arrays for both the narrowing beam width and the aliasing-free beam steering close to 180° FoV. Beginning from the same SOI substrate, Figure 3.2 shows the final device of 32 silicon-only channels of OPA. We did not apply dummy structures near the e-skid grating emitter since we devised a new method of e-beam lithography for writing sparse-dense waveguide array patterns, which we discuss in Chapter 4. Figure 3.2 (a) shows the full layout of the 32 channels of OPA. Figure 3.2 (b) and (c) indicates how the L-shaped combiner and e-skid grating array emitter look like. One difference between Figure 3.1 (c)

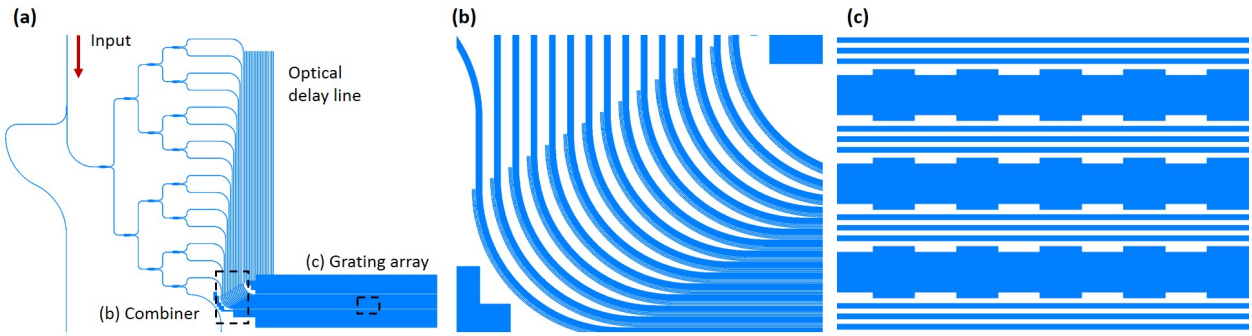

Figure 3.1. (a) Full-layout of a passive device of a 16-channel silicon-only L-shaped OPA device. (b) Layout image at the e-skid combining region. (c) Layout image of zoom-in from full-layout at the middle of the region of the grating emitter array.

and Figure 3.2 (c) is the number of fin layer. The e-skid grating emitters of 32 channels of OPA consist of four layers for enhancing mode confinement than three layers as the device has a longer combiner region at the corner of the L-shaped combiner than 16 channels one. In addition, we devised better fabrication technology to writing denser emitting array at that moment, thus, we choose four layers of e-skid fin structures. This fabrication technology will be discussed in Chapter 4.

Finally, we needed to make a device that could run at a much higher input power as the power handling capability of silicon is quite low at the input waveguide (less than 200 mW) due to its characteristics of high non-linearity and low LIDT. Since silicon nitride (Si_3N_4) has non-linearity an order of magnitude lower and four times the LIDT value, we used it from the input waveguide to the multi-stage cascaded 1x2 MMI splitter tree. Figure 3.3 shows the full layout. It was a similar structure to that in Figure 3.2 but instead of using silicon in the input and splitting tree branches, it replaced the material with Si_3N_4 and made a larger space due to its larger bending radius requirements for neglecting the bending loss of guided power. To use both Si_3N_4 and Si in the same device, we needed to make a component that could couple the mode that guided from each Si_3N_4 waveguide branch to the Si waveguide branch. We brought a design of two overlapping tapers. This component helped to convert the mode from a Si_3N_4 to Si waveguide with a neglectable loss. We discuss this component in detail in the following section.

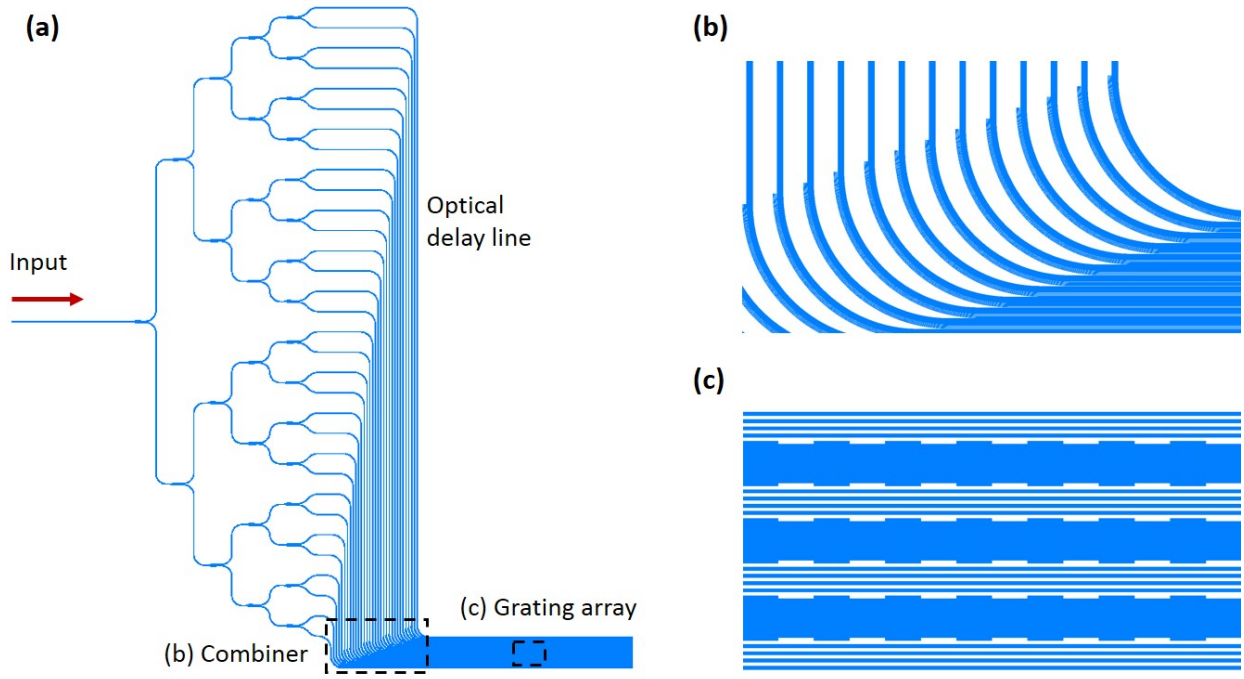

Figure 3.2. (a) Full-layout of the passive 32-channel silicon-only L-shaped OPA device. (b) Layout image at the e-skid combining region. (c) Layout image of zoom-in from full layout at the middle of the region of the grating emitter array.

To use the OPA device with an applicable LiDAR device, we needed to actively operate it. Otherwise stated, we needed to steer the beam by electronic control actuating onto the device with a fixed wavelength of an outside laser source. Then, the capability of the active phase shifting in each waveguide branch would be necessary. In a photonic integrated circuit (PIC) system, the microheater-based thermal optical phase shift technique is broadly adapted. Once the narrow width of metal wire is attached to the top of the dielectric cladded surface of the waveguide and has electric power applied to it, induced heat from the metal is delivered to the waveguide core material and the phase guided mode in the waveguide interferes concerning the thermal conductivity of the core material. We applied this model to the OPA structure. The operation process shown in Figure 3.4 (a) is different from those previously shown. Once an input power of approximately 1550 nm of working wavelength range was inserted at the entrance waveguide of Si_3N_4, it went through the multi-stages of the cascaded 1x2 MMI splitting tree, similar to the process shown in Figure 3.3 (a). We

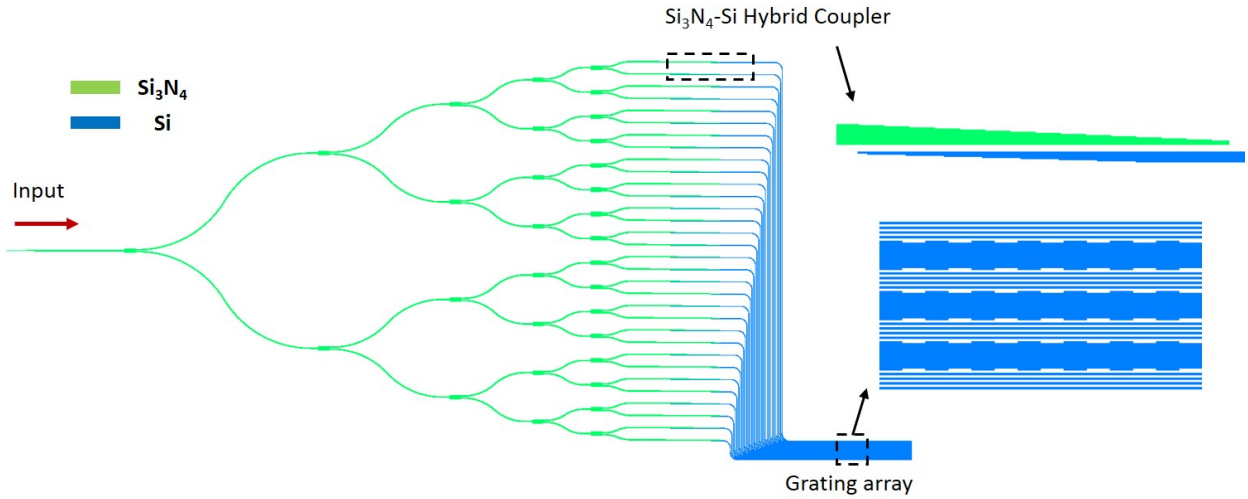

Figure 3.3. Full layout of the passive device for the 32-channel Si_3N_4 to Si hybrid structure L-shaped OPA device. The figure includes the Si_3N_4 to Si hybrid coupler and a zoomed-in image of the middle of the region of the grating emitter array.

wished to make an emitter that could generate a narrower beamwidth so we split the input power into 64 arrays. Then, each split mode went into the Si_3N_4-to-Si hybrid mode converter. Next, instead of guiding using e-skid at the combining region (from the large pitch (21 μm) of waveguide array to half-wavelength of its array), this device used k-mismatched waveguide arrays to guide each mode to the emitter array. As shown in Figure 3.4 (e), we chose silicon waveguides of both 500 nm and 400 nm of highly dispersive cross-sectional geometry to deliver each mode to the e-skid grating array emitter, reducing the crosstalk. Before the silicon's combining regions in Figure 3.4 (c), we applied the serpentine heater structure on top of the silicon array, as in Figure 3.4 (d).Since the heater required a relatively larger space than the waveguide array due to the heat crosstalk, the space between each line of the microheater was 42 μm. The width of the heater pad was 5 μm. The microheater was only applied to the width of the waveguide at 400 nm so that the single line control could tune the phased array with a certain amount of electrical power. The images of the device and the experimental demonstration are given in Chapter 5.

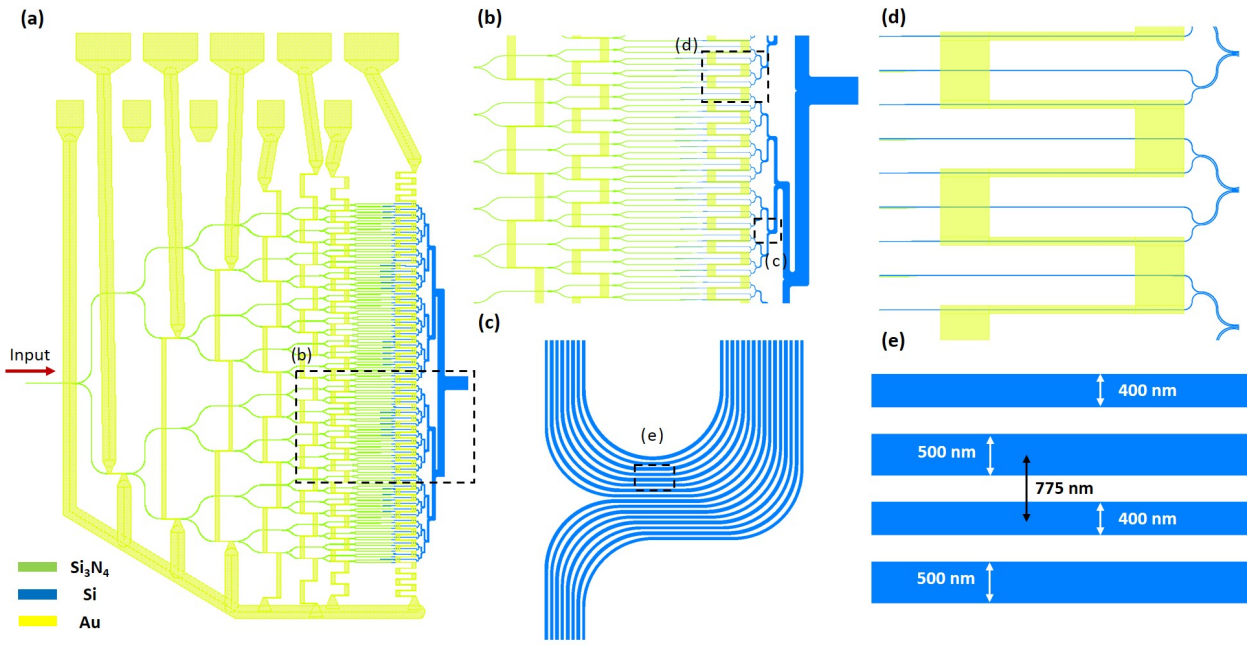

Figure 3.4. (a) Full layout of the active device of the 64-channel Si_3N_4 to Si hybrid structure with a k-mismatched waveguide arrayed OPA device. (b) Layout image at the area of the k-mismatched combiner and serpentine-designed micro-heater. (c) Detailed layout at the region of the k-mismatched combiner. (d) Detailed layout of the serpentine-designed micro-heater on top of Si waveguides. (e) Two different widths of the waveguides consisting of the k-mismatched combiner array with 775 nm of its pitch.

3.1.2 Full layout of waveguide arrayed DLA devices

This section discusses the newly designed layout of waveguide-arrayed DLA structures. As mentioned previously, waveguide arrayed DLA structures must have certain properties: first, they must be extendable structures for multi-inputs from the outside laser source, second, they should be able to sustain for generating the acceleration mode with high power sub-picosecond pulsed laser, and third, they should generate and resonate an acceleration mode in the electron projectile channel. Therefore, we invented the structure shown in Figure 3.5. Figure 3.5 (a) shows the 2D image of the structure and (b) shows a 3D image indicating how the device works from the input laser to generating the acceleration mode in the electron projectile channel. This device operated at the initial electron speed of β = 0.47. The input laser characteristics included λ = 1550 nm and a pulse width of 250

fs. To generate and resonate an acceleration mode in the electron projectile channel from the input laser source, several steps to modulating the input beam are required. First, the device coupled the free-space laser with the silicon nitride grating coupler and spread its power through the five stages of the cascaded 1x2 MMI splitting tree. Then, each split power went through the Si_3N_4 to Si hybrid mode converter and was split by the stage of the silicon's 1x2 MMI splitters. Next, each split branch was combined with the arrays that had an acceleration phase-matching pitch size, which corresponded to 775 nm for β as 0.47.With the very last branches of the array, one from the beginning and the other from the end, we attached the silicon's inverse grating structure which indicated, first, the intensity of the electric field emission from each combined array, and second, the phase matching from the output port array of the adjacent structure. This structural platform could achieve both a multi-input on-chip extendable device and a higher power input sustainability than the one with only a fabricated silicon structure.

Figure 3.6 describes the example of four stages of a multi-input waveguide arrayed DLA structure. This structure integrated four copies of a single stage of Figure 3.5 (a) by adjusting the additional lengths of either the Si_3N_4 waveguide from the grating coupler or the Si arrayed waveguide before the combining array regions with respect to calculating the time arrival of electrons from one stage to another. These lengths were related to the time intervals of input pulsed lasers from the outside source. With a suitable adjustment of length, we could easily extend the DLA arrayed structure with compact designs that previous conventional DLA structures could not achieve.

The design in Figure 3.5 and 3.6 is only acceptable in the initial velocity of the electrons of β as 0.47. However, for the shoebox design of the whole accelerator system by ACHIP, the initial electron velocity began at $\beta = 0.43$. With this initial velocity, the pitch size of the radiation array was approximately 670 nm, less than a half-wavelength. In this case, using the e-skid platform in the combining array region was difficult. First, the fin structures should have at least five layers of anisotropic media to guide less than half of the wavelength over 100 μm of its length and greatly squeeze the evanescent wave. Then, the width of each fin layer needs less than 20 nm of its width with the height of the silicon layer at 220 nm. It is difficult to fabricate such fins to stand firmly in the structure inside the arrayed structures.

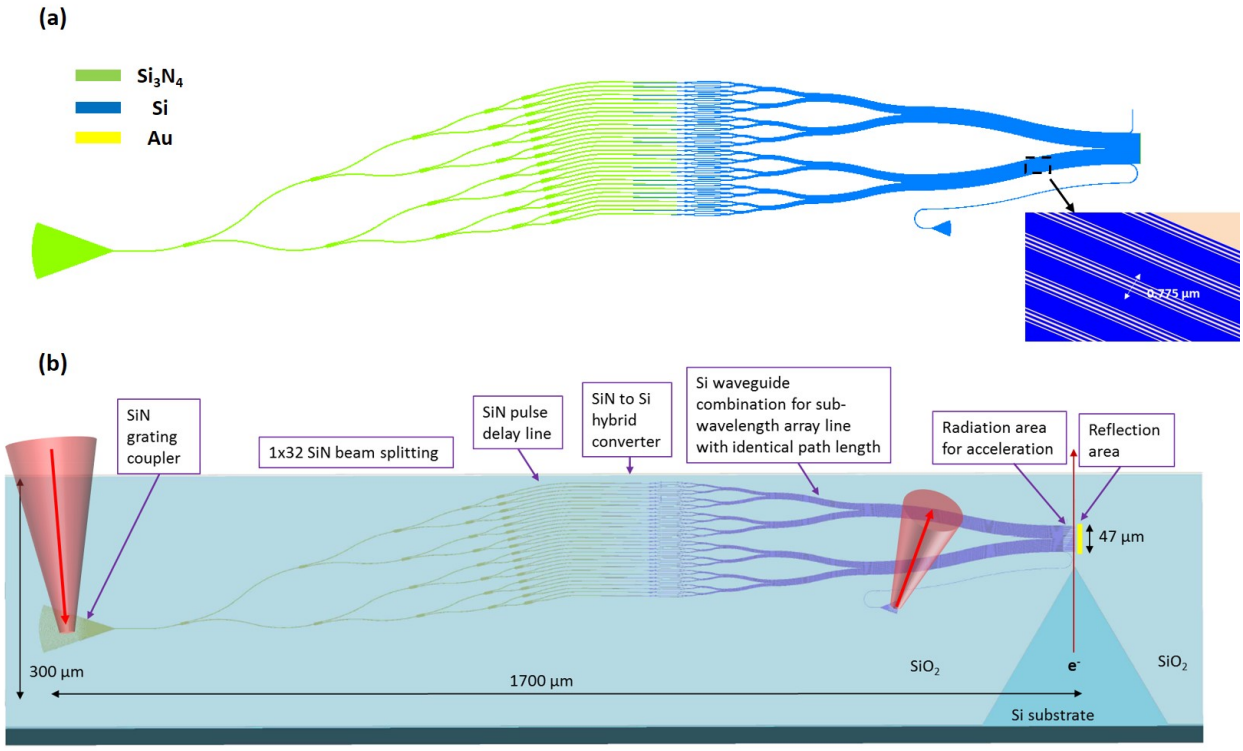

Figure 3.5. (a) Full-layout of waveguide-arrayed DLA structure from single input to 64 channels of a Si_3N_4 to Si hybrid structure. (b) 3D illustration and descriptions of each component from the 2D layout of (a). The inset image illustrates the combining array with 775 nm of its pitch using an e-skid waveguide array platform for accelerating the initial electron velocity of $\beta = 0.47$.

However, if we use a K-mismatched waveguide array, guiding the optical signal in less than half of the wavelength is possible and it has been demonstrated through the 3D-FDTD simulation. Additionally, since it does not require long, narrow fin structures, it is much easier to fabricate than the device with the e-skid array. Figure 3.7 (a) is the new proposed design for the hybrid waveguide arrayed DLA structure with k-mismatched silicon waveguide array for radiating acceleration modes that operate at the initial electron velocity as $\beta = 0.43$. Once the high power laser with sub-picosecond pulse width with 1550 nm of wavelength is coupled into the Si_3N_4 apodized silicon nitride grating coupler, as in Figure 3.7 (b), it first guides the incident power through the non-linear tapered waveguide slab and then distributes the power into eight branches with a different tapered structure, as in Figure 3.7 (c), which can distribute both power and phase uniformly into each Si_3N_4 waveguide channel. Next,

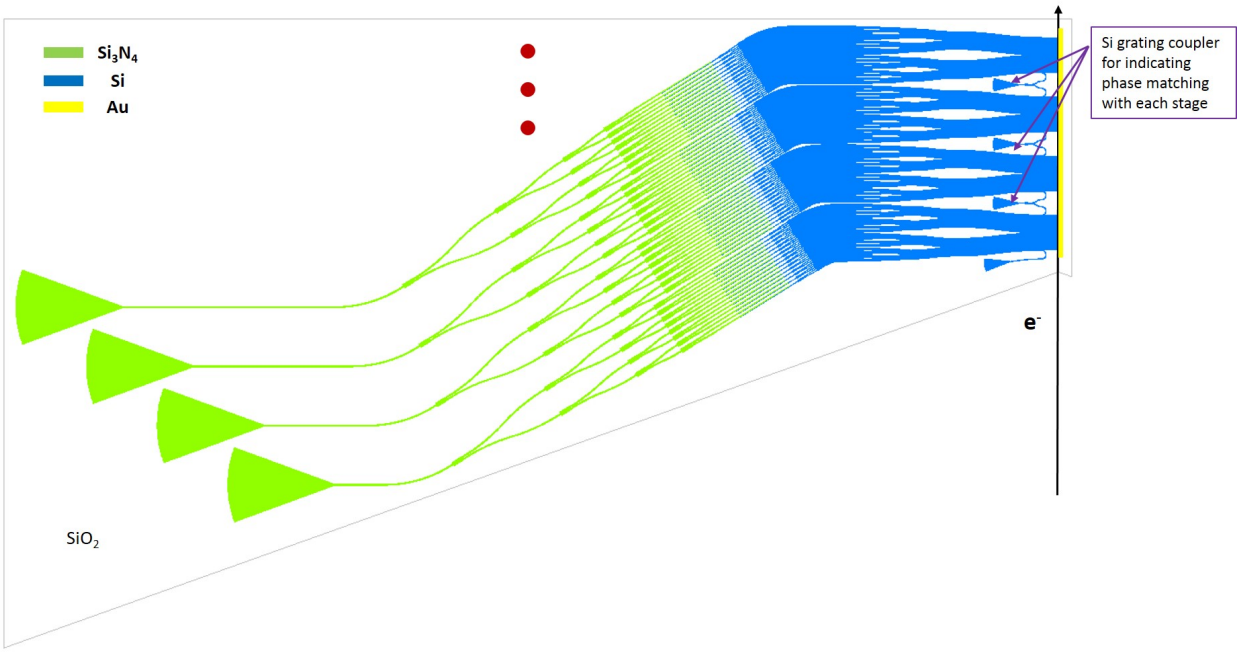

Figure 3.6. Example of the full layout with expanding four stages of waveguide-arrayed DLA structures from the single layout of (a). A total of 256 waveguide arrays generate acceleration mode in the electron beam channel.

the distributed optical powers go through the 90 degrees of racetrack-shaped bending curves, giving an equal amount of pulse delay lines for matching the electron projectile velocity into the electron channel. Those delayed pulses then go through the vertical broadening arrays that are the same path length lines for matching the vertical length of the area of the acceleration mode radiation. Then, likewise in previous designs of waveguide array DLAs, each guided pulse splits each power through the cascade, splitting through 1x2 Si_3N_4 MMI ports, and each split beam goes to a Si_3N_4 to Si hybrid converter and additional cascade splits to 1x2 Si MMI ports, as in Figure 3.7 (d). These are then combined into the 670 nm of acceleration mode radiation array by K-mismatched platforms (which looks like Figure 3.7 (e)) choosing 500 nm and 400 nm of the width (Figure 3.7 (f)).

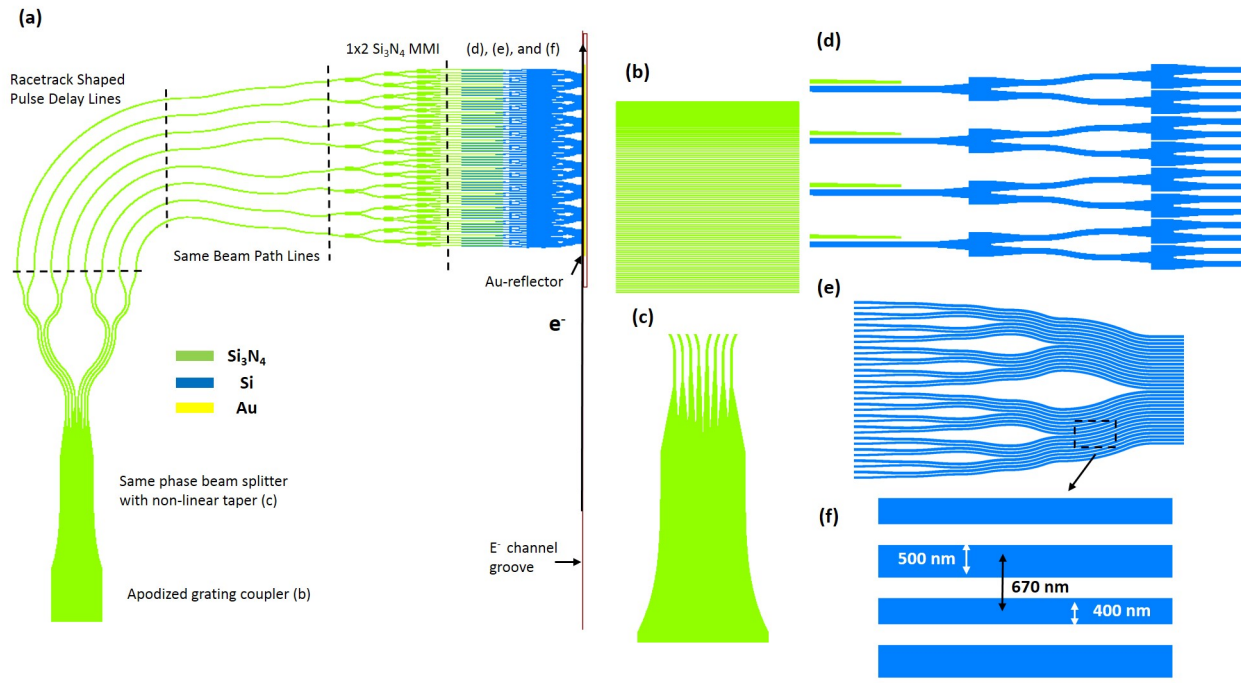

Figure 3.7. (a) Full layout of the 256 channels waveguide arrayed DLA structure consisting of a Si_3N_4 apodized grating coupler, eight branches of nonlinear tapered beam splitters, and a Si_3N_4 to Si hybrid converter. (b) Detailed layout image of a Si_3N_4 apodized grating coupler. (c) Detailed layout image of Si_3N_4 branches of nonlinear tapered beam splitters. (d) Detailed layout image of the Si_3N_4 to Si hybrid converter and 1x2 Si MMI splitter tree. (e) Detailed layout image of 32 channels of a k-mismatched waveguide combining array. (f) Two different widths of the waveguides consisting of the k-mismatched combiner array with 670 nm of its pitch for accelerating an initial electron velocity of $\beta = 0.43$.

3.2 Optimized designs of each component and simulation results

3.2.1 E-skid and K-mismatched arrays with half-wavelength pitch

All devices discussed in Chapter 3.1. operated at 1550 nm of wavelength range and commonly have combining regions of at least a half-wavelength pitch-sized array. The results from the published journals, for example, with the e-skid structure, were obtained with more than a half-wavelength spacing. Thus, we had to run the 3D-FDTD simulations to investigate optimized designs for e-skid in a half-wavelength pitch-sized array and how much the crosstalk occurs in the optimized array. For a k-mismatched waveguides array, it has previ-

ously been demonstrated with the half-wavelength pitch-sized array at 1550 nm. However, for waveguide arrayed DLAs with a shoebox application (which corresponds to the initial velocity of the electron as $\beta = 0.43$. Therefore, we must investigate through the 3D-FDTD simulation whether a k-mismatched waveguide array is applicable at the 670 nm of the pitch-sized array. First, we ran the simulation using 100 μm of a straight waveguide array. Figure 3.8 shows the 3D-FDTD simulation structural design and the results of arrayed propagation of the CW laser with 1550 nm of wavelength. Figure 3.8 (a) and (b) introduce the dimensions of the cross-sectional and plane views of the same width of the straight waveguide array. Figure 3.8 (c) and (d) present the 3D-FDTD simulation results of the magnitude of the electric field propagation from 1550 nm wavelength CW laser input with all same-phase (c) and 60-degree delayed phases at each adjacent waveguide (d). Figure 3.8 (e) and (f) show the electric field intensity at 94 μm away from the input with same-phase (e) and 60-degree delayed phase at each adjacent waveguide (f). The results show that the simple straight waveguide arrays at the half-wavelength pitch space are not a good platform to deliver the optical power and phase due to the crosstalk issue in between the waveguide propagation.

Therefore, we simulated a similar structure with the e-skid fin structures applied in between the adjacent waveguides. Figure 3.9 (a) and (b) show the dimensions of the cross-sectional and plane views of the e-skid simulation structure. We chose four layers of fin structure to make anisotropic media in between the waveguide arrays; thus, the width of each fin was 36 nm. To see any phase distortion of the guidance due to the crosstalk, we applied 60 degrees of delay input from each waveguide to the other. Additionally, we used the top cladding materials with silicon dioxide (SiO_2), the same material as the bottom cladding, and made a model where the void gap was trapped in between the fin structure and the cladding materials up and down for keeping high refractive index contrast. The simulation results of the electric field and its phase delivery results are shown in Figure 3.9 (c) to (f). Figure 3.9 (c) shows a 1D plot of the intensity of the electric field at the end of the array line at half of the height of the silicon thickness. Figure 3.9 (d) shows a 2D plot of the guided mode at the end of the array. Figure 3.9 (e) shows the propagation intensity of the electric field over a 100 μm e-skid array. Figure 3.9 (f) shows the phase propagation of quasi-TE_0 mode at the end of the propagation simulation with 60-degree delayed lines

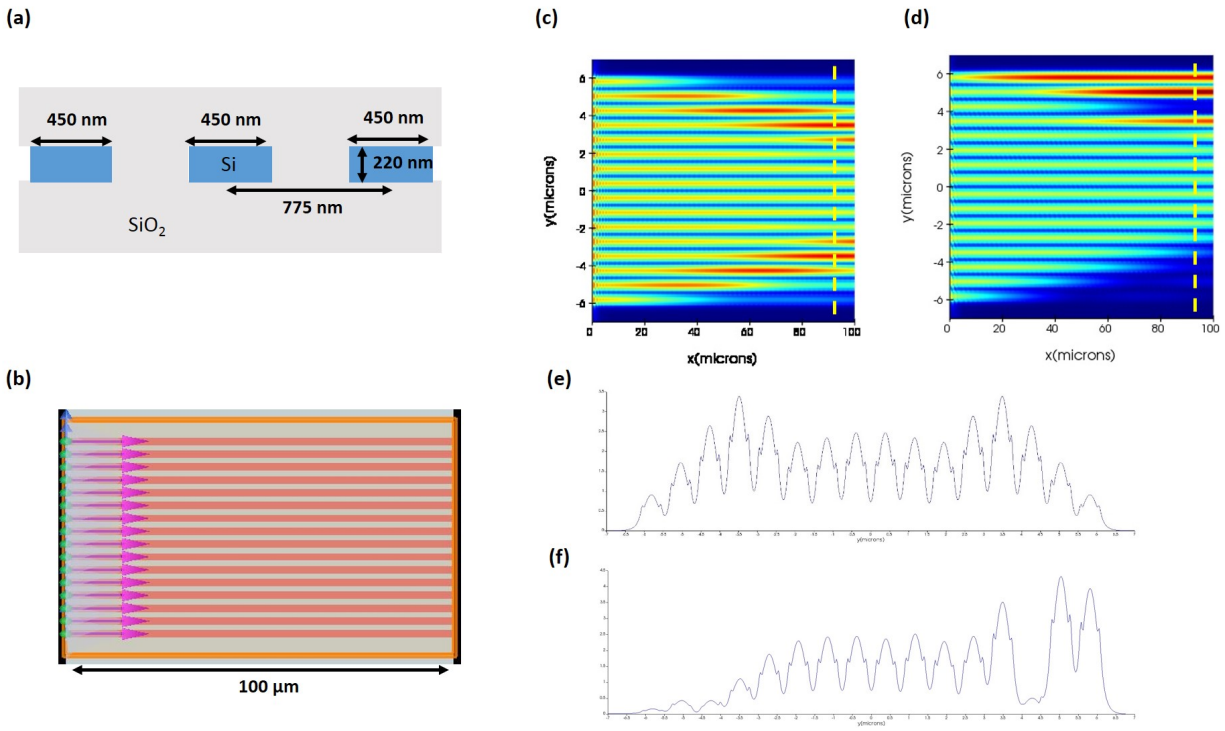

Figure 3.8. (a) Illustration of a cross-sectional view for running a 3D-FDTD simulation of the Si waveguide array with equal spacing with geometric parameters of 450 nm of width, 220 nm of thickness, and 775 nm of pitch. (b) Illustration of the top-view of the Si waveguide array with 100 μm of length for the 3D-FDTD simulation. (c)-(d) Results of the electric field intensity distribution while optical power was propagating into the structure of (b), simulated by 3D-FDTD with $\lambda = 1550$ nm and all in-phase propagation (c) and 60-degree delayed propagation (d). (e)-(f) Plot of the electric field intensity distribution of a cross-section at the end of the array, where x = 100 μm corresponding with the initial optical delay of (c) and (d).

with respect to the adjacent input power. Both power and phase were well guided through 100 μm of the dense array. The 3D-FDTD simulation demonstrated that the power loss and crosstalk were negligible within 100 μm of dense array. 3D-FDTD simulation demostrated that the power loss and crosstalk are negligible within 100 μm of arrayed length when the quasi-TE_0 mode was transmitted through them.

Finally, we tested the k-mismatched waveguides. The array consisted of the two different widths of waveguides, 400 nm and 500 nm, and these widths were 100 nm larger than the widths that were proposed in Dr. Phare's 2018 design [36]. Since the full layouts of

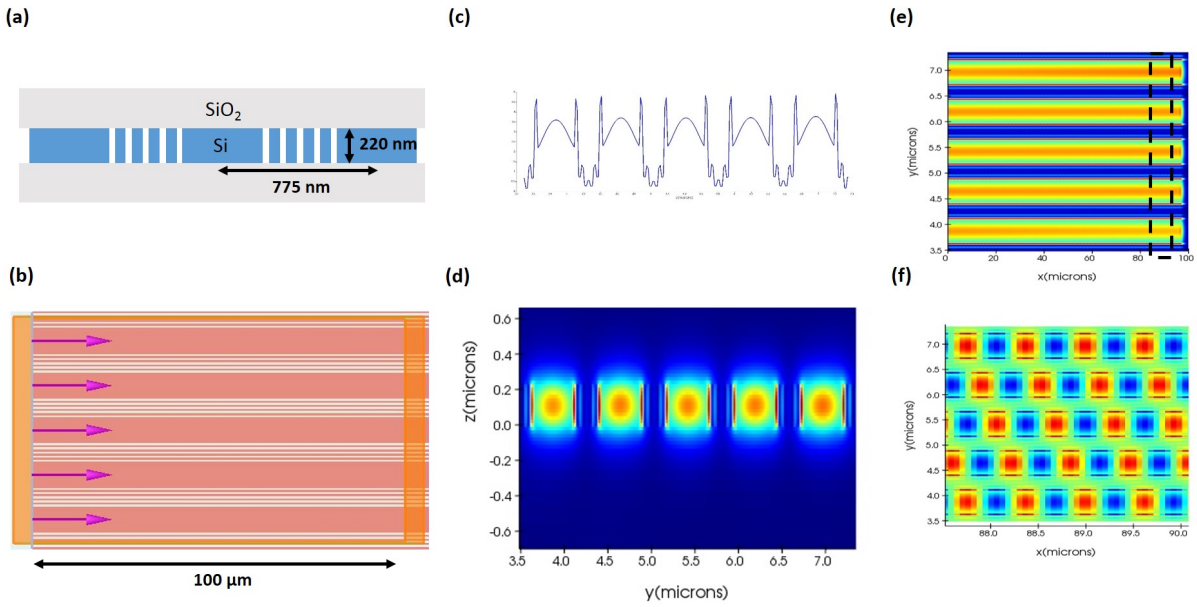

Figure 3.9. (a) Illustration of cross-sectional view for running a 3D-FDTD simulation of Si waveguide array with an e-skid platform, where its geometric parameters are 450 nm of central waveguide width and 220 nm of its thickness, and 775 nm of pitch, including four layers of metamaterial between the adjacent waveguides. (b) Illustration of the top-view of the Si waveguide array with an e-skid platform applied among the 100 μm of its length for the 3D-FDTD simulation. (c) 1D plot of the simulated result of the electric field intensity distribution propagating at the end of the array (100 μm) of the structure shown in (b) with $\lambda = 1550$ nm and 60-degree delayed initial phase difference with adjacent waveguides. (d) 2D result of (c). (e) Top-view of the simulated result of the electric field intensity distribution among the 100 μm of e-skid arrayed waveguide propagation. (f) The simulated result of the constant phase difference among the propagating arrayed waveguides near the end of the output array.

OPA-based LiDAR and waveguide arrayed DLA structures consisted of the sizes of their arrayed pitch with half-wavelength or smaller sizes, a 3D-FDTD simulation with less than half-wavelength pitch sizes was required. We simulated the structure with 670 nm of pitch size of 100 μm in length, the same conditions as in two previous simulations. The results are shown in Figure 3.10. Figure 3.10 (a) to (c) presents the overall structural view of the 3D-FDTD simulation and plane and cross-sectional views of the structure. Figure 3.10 (d) presents the propagation intensity of the electric field over 100 μm of k-mismatched array and (e) shows the 1D plot of the intensity of the electric field at the end of the array line at

half of the height of the silicon thickness. Figure 3.10 (f) shows the phased array that was propagated through the k-mismatched array line and (g) is a zoomed-in image in the middle of the array line that shows the phase guidance. Figure 3.10 (f) and (g) demonstrate two different thicknesses of array that can guide the optical power and phase with low crosstalk as the propagation constant of each thickness of waveguide is different from the other; thus, the phases are continuously mismatched while the signals are transmitted through the lines of the array.

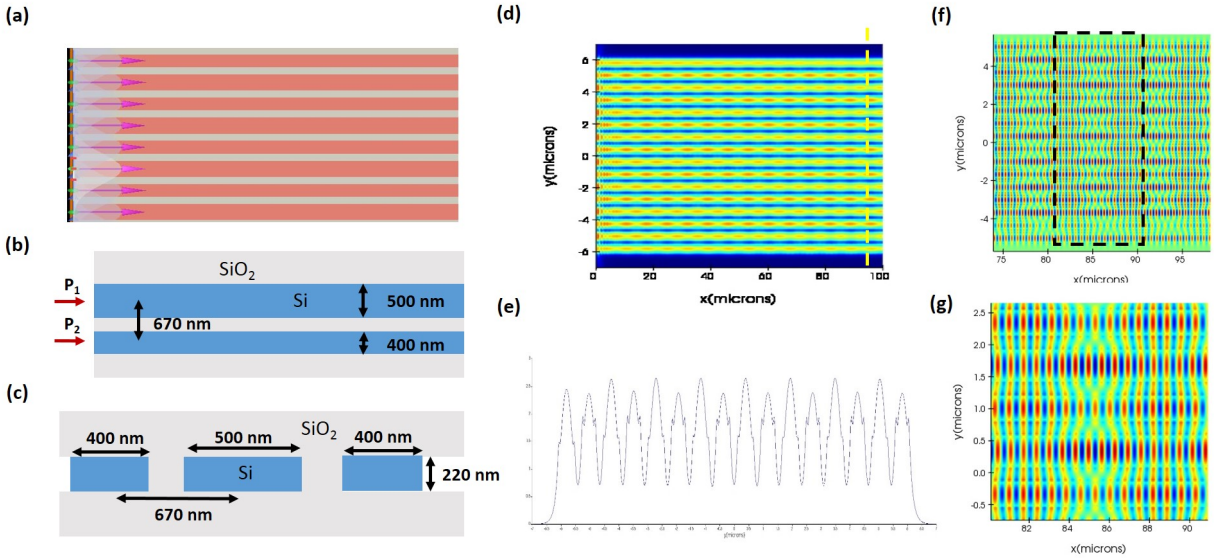

Figure 3.10. (a) Illustration of a top-view image of a Si waveguide array with a k-mismatched platform applied among the 100 μm of its length for the 3D-FDTD simulation. (b) Close-up image showing the simulation array of (a), consisting of 400 nm and 500 nm of widths of the waveguides and arrayed with 775 nm of its pitch. (c) Illustration of a cross-sectional image of (a). (d) Top-view of the simulated result of the electric field intensity distribution among the 100 μm of k-mismatched arrayed waveguide propagation. (e) 1D plot of the simulated result of the electric field intensity distribution propagating at the end of the array (100 μm) of the structure. (f)-(g) Simulated results of optical power propagation with the initial phase of all in-phase (0-degree delay) (d) and 60-degree phase delay of each adjacent waveguide, (g) among the propagating arrayed waveguides near at the end of the output array.

3.2.2 Design of silicon nitride to silicon hybrid mode coupler

As discussed earlier, both OPA-based LiDAR and waveguide arrayed DLA structures need material selections to establish the capability of a high-power delivery system. The silicon nitride had a damage threshold approximately four times higher than that of silicon, as discussed in Chapter 2. Thus, it is better to use only silicon nitride for the whole device structure if the power handling capability is the only characteristic to consider. However, due to the lower refractive index of Si_3N_4 (approximately 1.98 in 1550 nm of wavelength) than silicon (which is approximately 3.48), the waveguide design of Si_3N_4 requires a much larger bending radius (at least 50 μm with 300 nm of its thickness) than that of silicon for neglecting bending loss of power. Additionally, due to its lower confinement of the mode, it is not suitable with the dens output port branches. To increase the power handling capability and build a denser waveguide array structure, a Si_3N_4 to Si hybrid waveguide coupling system is necessary. Several studies have investigated hybrid inter-layer taper couplers [40]–[42], like a structures of Figure 3.11. Guiding the quasi-TE0 mode of 1550 nm of wavelength in silicon nitride requires 1.2 μm of its width at 300 nm of its thickness. To deliver the mode from Si_3N_4 to Si core waveguide (which has 450 nm of width and 220 nm of standard SOI substrate), two tapered couplers should be placed at the same location with different heights, as in Figure 3.11, so that the strength of the mode confinement of the Si_3N_4 waveguide decreases but the strength of the Si waveguide increases. Then, the mode can be gradually converted from Si_3N_4 to Si cores, as in the YZ view in the middle section of Figure 3.11. Finally, the fine quasi-TE_0 mode can be achieved at the end of the silicon waveguide with smaller its mode size than that of Si_3N_4.

However, fabricating the Si_3N_4 to Si hybrid tapered coupler of Figure 3.11 requires a chemical-mechanical polishing (CMP) process. This is because, once the silicon dioxide (SiO_2) layer has been deposited on top of the silicon waveguide using the various types of chemical vapor deposition (CVD) processes, usually, a bump-shaped surface of silicon dioxide is created, as in Figure 3.12 (c). If silicon nitride deposition is processed on top of that silicon dioxide surface and written and etched to make silicon nitride waveguide hybrid couplers, it creates distorted core cross-sections and causes unwanted coupling loss and mode distortion.

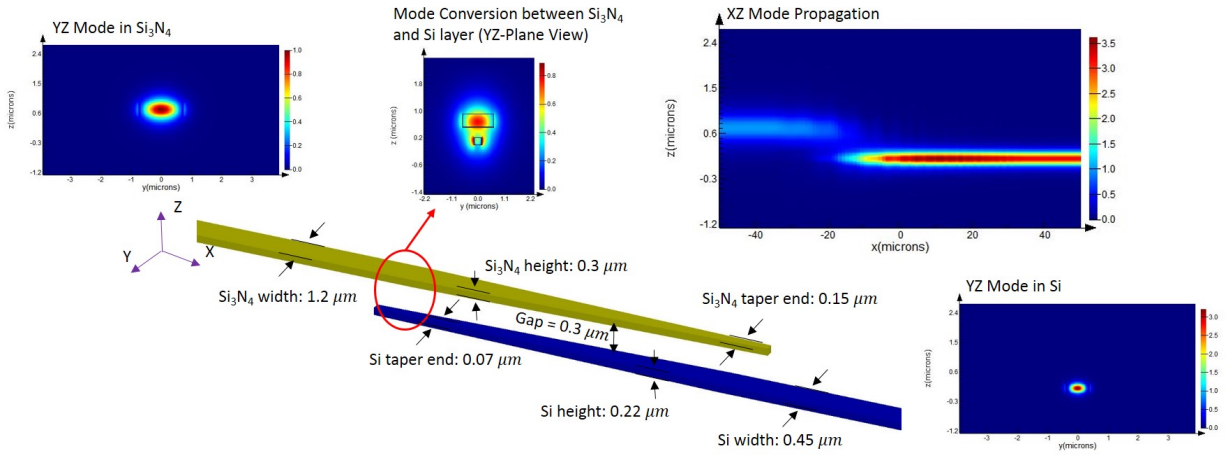

Figure 3.11. Schematic illustration of an example of Si_3N_4 to Si hybrid mode converter and the mode profiles while it travels through +x-direction. Both tapered waveguides of Si_3N_4 and Si are aligned at the center of each waveguide of y-position with 300 nm of height difference, covering all its background of SiO_2.

This is why a CMP process is required before depositing silicon nitride on top of an inter-layered silicon dioxide surface. However, the CMP process is expensive and it is difficult to control the thickness of the cladding materials. Therefore, we introduced an asymmetric-shaped inter-layer hybrid coupler, as in Figure 3.12 (a) and (b). Instead of placing both tapered structures at the same location, they were placed so they were slightly shifting from one to the other with respect to the y-axis and making tapered slopes only at the side of the outer one , as in Figure 3.12 (a), so that we can achieve the hybrid tapered couplers without CMP processing or low-loss of mode conversion. The amount of space between those two tapered waveguides is critical; if the silicon dioxide inter-layer is deposited at approximately 100 to 200 nm, then 300 nm of its gap size is sufficient for neglecting the mode conversion loss, as in Figure 3.12 (d).In addition to the gap size optimization, we also found the optimized parameters of the hybrid tapered coupler geometry, such as the tapered length of both silicon nitride and silicon, waveguide offsets from the tapered tips of the other materials, and the final widths of the tapered tips, using 3D-FDTD simulation. The results of the optimized parameters are shown in Figure 3.12 (b).

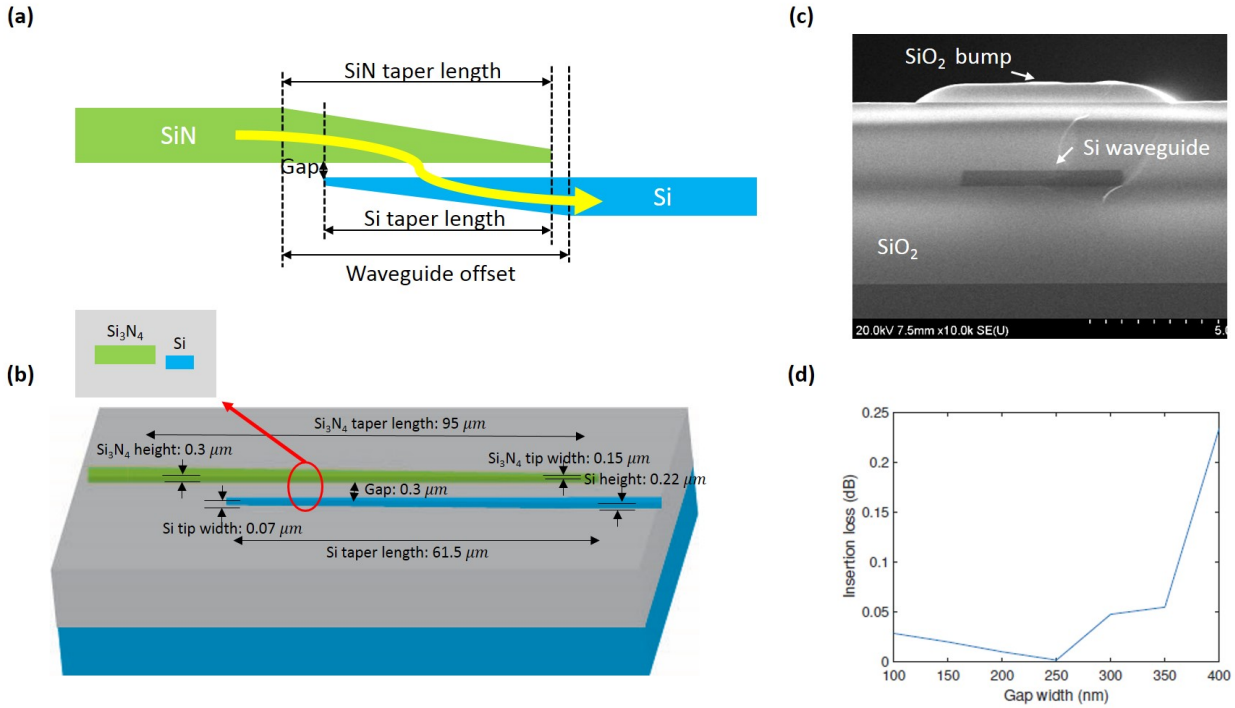

Figure 3.12. (a) Schematic illustration of the Si_3N_4 to Si hybrid mode converter with misaligned structure and the path of optical power transmission. (b) 3D image of the Si_3N_4 to Si hybrid mode converter of (a) placed in the SOI platform, and specific values of the parameters. (c) SEM image of an example cross-sectional view of SiO_2 upper cladding on top of the Si waveguide and the bump of SiO_2 that is inevitably shown on top of the Si waveguide. (d) Simulated result of insertion loss with respect to the different sizes of gaps in between Si_3N_4 and Si asymmetric tapers.

3.2.3 Optimized design of a 1x2 multimode interferometer (MMI) beam splitter with silicon and silicon nitride

All of the device structures shown in Chapter 3.1.1 had cascaded beam splitting tree structures; 1x2 MMI splitters were used for the splitting methods. Since the splitters required not only that the power was divided with an equal amount on each output port but also that the same phase-front was maintained on both of the output ports, the 1x2 MMI splitter was the appropriate structure. It satisfied both these requirements as it used the self-imaging effect [43]–[45]. A low-loss design for a 1x2 MMI splitter was crucial to minimize loss while the input power transmitted through several stages of the cascaded MMI tree (see Figure 3.13 (a)). In this section, the optimized designs of 1x2 MMI for both 220 nm thickness of

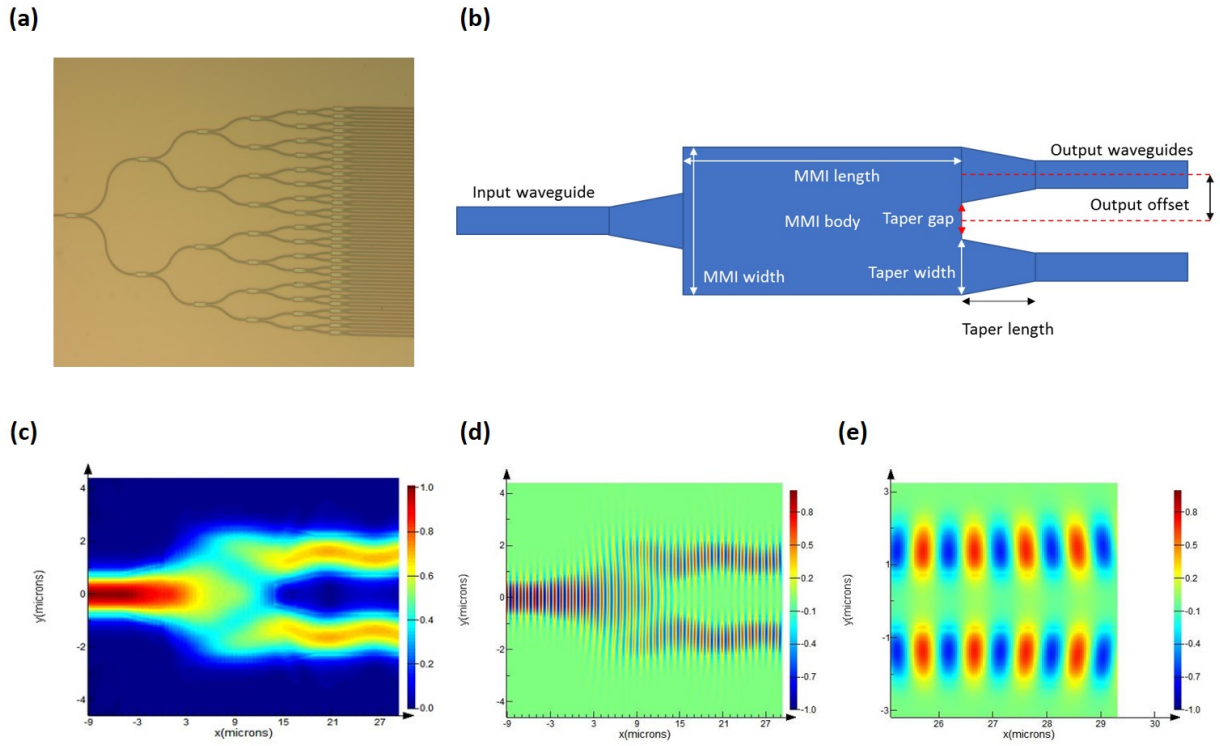

Figure 3.13. (a) Optical image of cascaded 1x2 MMI tree splitters of Si arrayed waveguide. (b) Illustration of specifically designed parameters of 1x2 MMI splitter. (c) Result of electric field profile of optimized 1x2 MMI splitter. (b)-(c) Results of the simulation of 1x2 MMI splitter of phase output. (c) Zoomed-in image at the output ports of (b).

silicon on insulator (SOI) and 300 nm thickness of silicon nitride platform are discussed. A basic scheme of an MMI splitter is shown in figure 3.13 (b). To optimize the designs for achieving the lowest loss in both platforms, the values of the parameters shown in Figure 3.13 (b) should be defined at specific conditions. We used a 3D-FDTD simulator to obtain the best parameters that gave the lowest loss of input power at the 1550 nm of working wavelength on both platforms. Table 3.1 presents the results from the simulations on each platform. The insertion losses of these two designs were lower than 0.1 dB, making them suitable for using the component of the cascaded beam splitting trees.

Table 3.1. Parameters of optimized 1x2 MMI in SOI and Si_3N_4 platforms

Parameters	SOI	Si_3N_4
Waveguide width (nm)	450	1200
Waveguide height (nm)	220	300
MMI body length (μm)	3.3	12.5
MMI body width (μm)	2	5
Taper length (μm)	2.8	3
Taper width (μm)	1	2.34
Output offset (μm)	0.5	1.33

3.2.4 Apodized grating coupler of silicon nitride with power splitter with equal phase

In Chapter 2.3, we briefly discussed that silicon has a value of its LIDT ($\sim$ 0.17 J/cm^2) about a quarter of its value of silicon nitride ($\sim$ 0.68 J/cm^2). Hence, for coupling the high-power laser with the NIR sub- picosecond pulsed width, fabricating grating couplers with silicon nitride platform is more advanced than using silicon grating couplers due to the laser-induced damage of the structure. However, the coupling efficiency of a mono-layered uniform grating coupler of silicon nitride reported, at most, 38 %, due to its lower mode confinement strength and the exponential scattering intensity distribution [46]. Dr. Zhexin Zhao, a member of ACHIP, proposed an analytical model to design an apodized grating coupler that indicates which geometric parameters, such as periodicity and etch length, are changed along the grating coupler [47]. Her article proposed the algorithms for optimizing the scattering strength of each range along the length of the coupler and satisfying phase-matching conditions at each unit cell of grating [47]. Once the material and its thickness are selected and its etch length defined, the grating pitch for satisfying the phase-matching conditions should be:

$$\Lambda = \frac{\lambda + l_e(n_{wg} - n_e)}{n_{wg} - n_c sin\theta}, \tag{3.1}$$

where Λ is the pitch, l_e is the etch length, λ is the free-space wavelength, n_e and n_{wg} are the effective indices of the etched and unetched slab waveguide [47]. By running the

numerical simulation with a long uniform grating of a given etch length and pitch, the scattering strength of each pitch was extracted by fitting the remaining power in the guided mode along the propagation direction, matching its optimal scattering strength equations (α_z) into the following equation:

$$\alpha_z = \frac{A_t^2(z)}{2\{\int_z^L \sqrt{2\alpha^*(s)} exp[-\int_z^s \alpha^*(t)\,dt] A_t(s)\,ds\}^2}, \tag{3.2}$$

where $A_t(z)$ represents the intensity of the field with respect to the propagation direction (z-direction), and L is the total length of grating coupler. With the given grating pitches driven from the previous model (with the condition of full-etching of 300 nm of the thickness of Si_3N_4 and 50 μm of the length of grating coupler), we ran again with the 1D-FDTD simulation, including the thickness of 2.2 μm of buried oxide (BOX) and 2.38 μm of upper cladded SiO_2, like the figure 3.14 (a) shown, we achieved up to 60 % of efficiency (presented on figure 3.14 (c), which is higher compared with the reported values of sole-Si_3N_4 grating couplers. Figures 3.14 (e) and (f) show the various type of grating coupler we can design for applying into waveguide arrayed DLAs with the given information of grating pitch and etch length, described in the figure 3.14 (g).

ACHIP tested the laser-induced damage threshold of 300 nm thickness of a Si_3N_4 grating coupler. Dr. Yu Miao, another collaborator in ACHIP, fabricated a uniform pitch grating coupler combined with a tapered-down single-mode output waveguide structure (see figure 3.15 (a)). The characteristics of the input laser were 1550 nm of the central wavelength, 300 fs of pulse width, and 100 kHz of repetition rate. Its beam diameter was 33 μm. The measured maximum input energy without degradation was 30 nJ. At that point, the output energy without degradation was 3 nJ. The laser-induced damage occurring at the input grating coupler was 150 nJ, approximately five times higher than the output power degradation. As shown in figure 3.15 (b) and (c), power degradation and damage started at the bottleneck of the tapered structure where the electric field intensity became the highest. Therefore, we needed to design a tapered, multi-branched waveguide to mitigate the concentration of the electric field intensity from the input power.

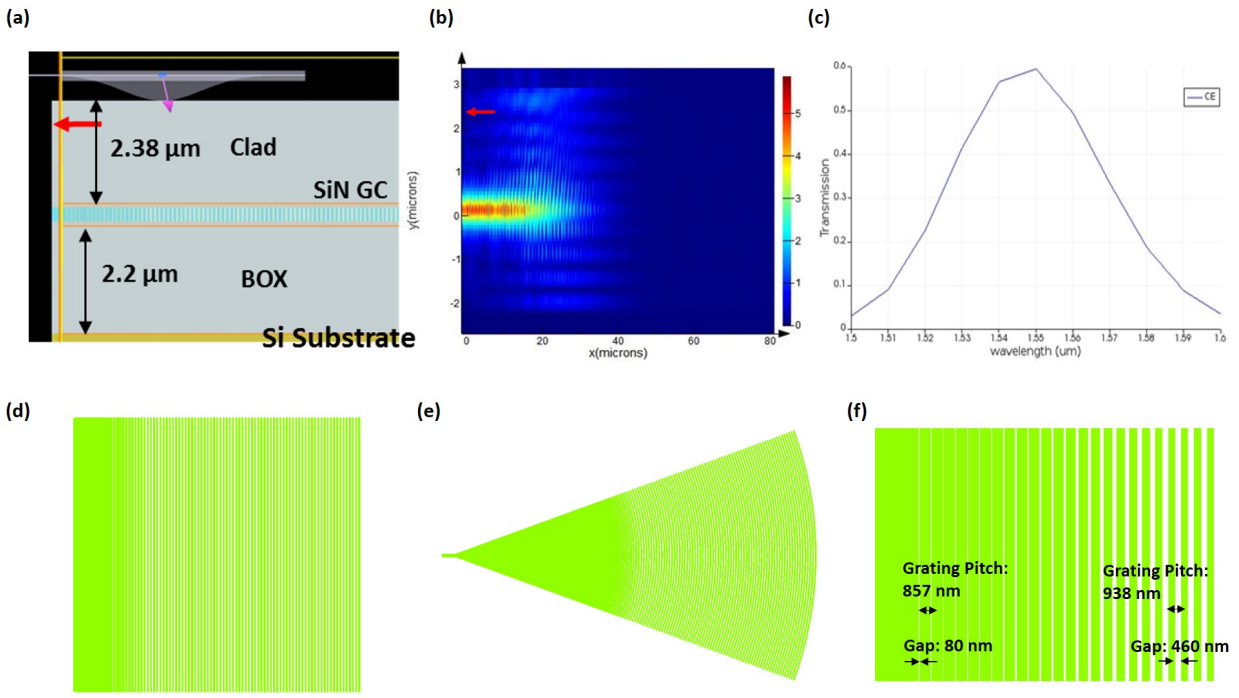

Figure 3.14. (a) Illustration of a simulated construction of apodized Si_3N_4 grating couplers. Free-space single-mode Gaussian beam of 1550 nm of central wavelength inserted into the grating coupler tilted at 10 degrees, and the grating coupler surrounded by 2.2 μm of BOX and 2.38 μm of top cladding with SiO_2. (b) Simulation result of power coupled by apodized Si_3N_4 grating couplers. (c) Result of coupling efficiency of the structure. (d)-(f) Various layout images based on the information of the grating pitch and etched length from the simulated construction of (a).

We designed the grating coupler with single-mode beam splitters. Figure 3.16 (a) and (c) illustrate the full layout of waveguide-arrayed DLA structures; the grating couplers and their splitter designs are shown in Figure 3.16 (b) and (d). We designed two types based on the free-space beam spot sizes. First, for 21 μm of beam diameter, we designed four arrays with 5 μm spacing at the output. Second, for 50 μm of beam diameter, we designed up to eight arrays with 5 μm spacing output single-mode waveguides. To design these splitters, we considered not only distributing power intensity but also aligning the optical phase degree at the same locations on various waveguide branches to generate an acceleration mode at the end of the output radiation port. To satisfy these conditions, we used a 2.5D-FDTD simulator to obtain the best parameters for the splitters.

Figure 3.17 (b) illustrates the basic structure to simulate. For 21 μm of input with quasi-TE_0 mode guided after coupling with a Si_3N_4 grating coupler, the mode was separated by four tapered waveguides. To find the optimum point to satisfy both power and phase conditions, we simulated the electric field intensity distribution by changing the parameters of the positions of the center of each tapered waveguide, the tapered width, each tapered length, and the overlapped area at the starting position of the tapers. For power distribution, the center position and the width of each tapered waveguide were the main factors; the tapered length was the main factor for aligning phase positions for the difference of each phase speed. Figure 3.17 (c) to (f) show the results of the optimized structure. Figure 3.17 (c), (d), and (f) present the electric field distribution splitted by the optimized structure, one with top-side and the others with the cross-sectional output ports of Si_3N_4. Figure 3.17 (f) is an 1-D plot of the maximum electric field intensity at the middle of its height from (d). These results clearly show that this optimized structure can distribute power equally. Additionally, as figure 3.17 (e) illustrates, with the phase position at the output ports, these optimized splitters also satisfy the same phase generation from the single-mode input power.

Furthermore, we expanded the design to accommodate larger beam diameters and higher numbers of branches to avoid laser-induced damage and the degradation effects of power delivery. We optimized eight branches of splitters for coupling the same laser characteristics with 50 μm of the beam diameter. First of all, similar to our design approach for the four-branched splitting structure in Figure 3.17, we set 52 μm of slab width for guiding 50 μm of quasi-TE_0 and then obtained the optimized parameters for the tapered positions of each branch, the width and length of each taper, and their overlap regions. Then, to couple the full range of the Gaussian beam with 50 μm of its full width at half maximum (FWHM) of diameter, we placed 80 μm of the width of grating coupler so that the profile of electric field intensity of Figure 3.18 (a) can be coupled in the grating coupler and guided to initial Si_3N_4 slab waveguide. To connect the width of grating coupler and the splitting branches, we placed nonlinear tapered slab in between for guiding the coupled power with modulating the power intensity and phase. We designed a nonlinear curve using the following equation:

$$\omega(x) = \alpha(L - x)^m + \omega_2, \tag{3.3}$$

where L is a length of tapered region and $\omega(x)$ is a width of certain tapered position, and if $\omega_1 = \omega(0)$ and $\omega_2 = \omega(0)$, then the value of α would be:

$$\alpha = \frac{\omega_1 - \omega_2}{L^m}. \tag{3.4}$$

We found out when the value of L is 170 μm, α is 1.676e^{-}8 and m is 4, and these parameters of nonlinear tapered slab gave the best profile of electric field intensity distribution among eight branches. Figure 3.18 (c) to (f) show the results of the 2.5D-FDTD simulation with such parameters. We achieved less than 15 % of 8-branches of electric field distributions and achieved phase alignment at the same position as the output branches.

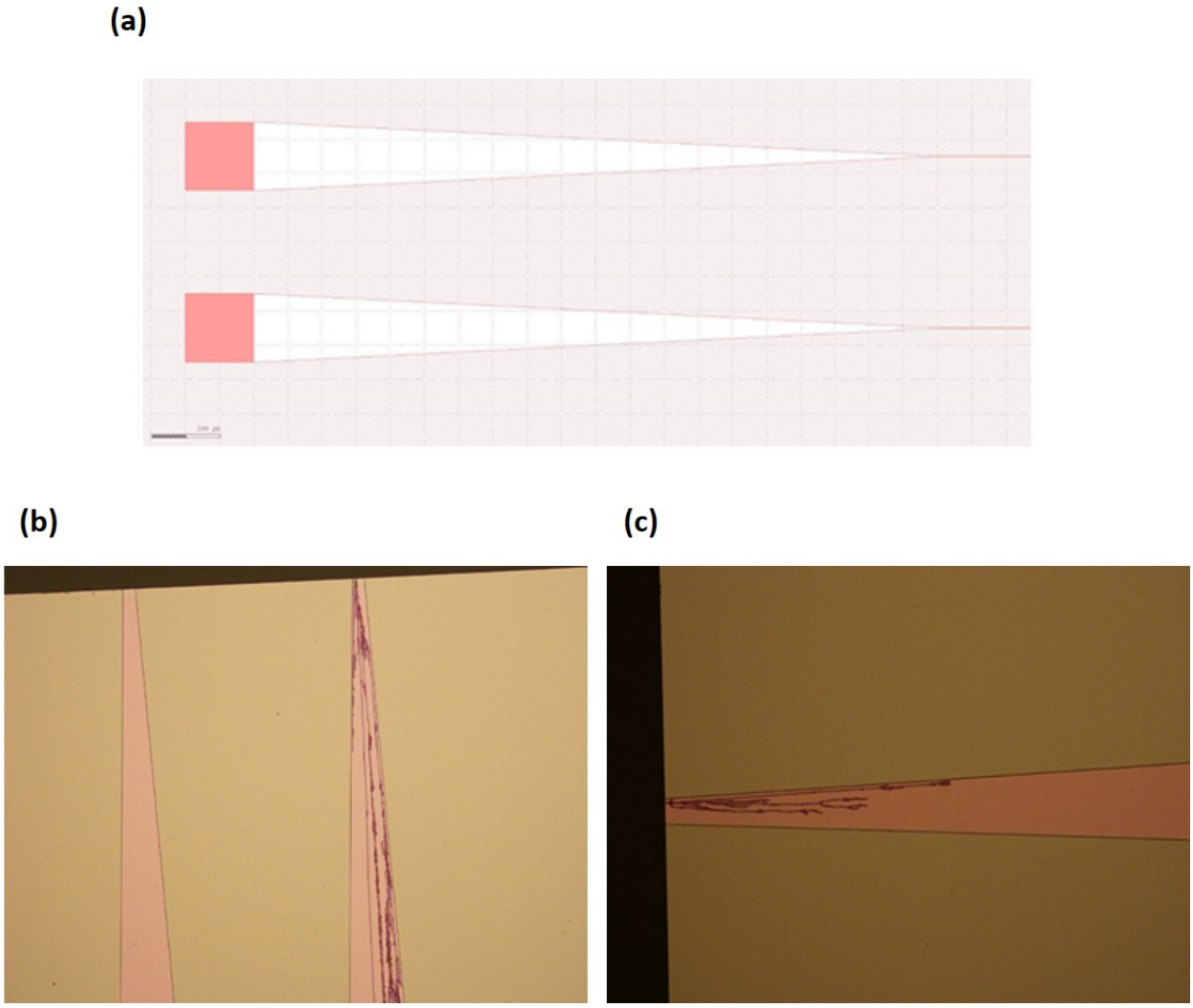

Figure 3.15. (a) Layout image for testing the laser-induced damage fluence of a given pulsed laser of 300 fs of pulsed width, 1550 nm of the central wavelength, 100 kHz of repetition rate, and 33 μm of the beam diameter. (b)-(c) Optical images of damaged tapered waveguides with approximately 30 nJ of input energy.

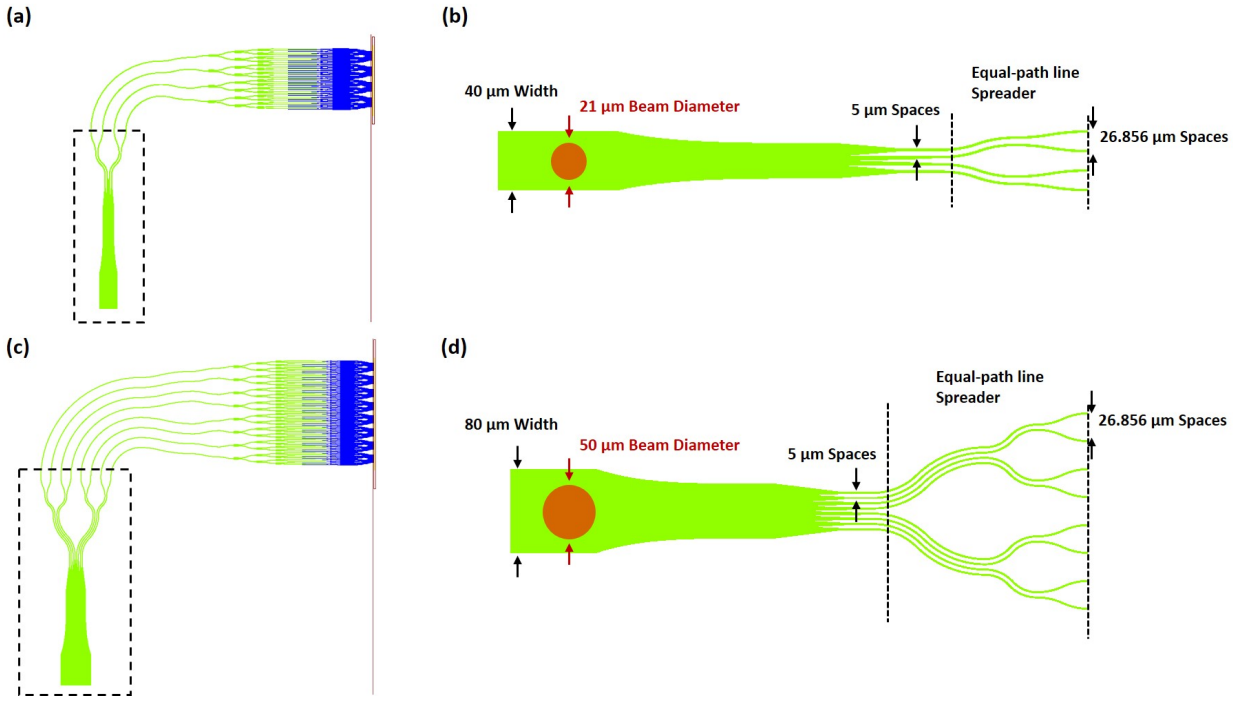

Figure 3.16. (a) Full-layout of a waveguide-arrayed DLA structure consisting of a Si_3N_4 apodized grating coupler with four branches of nonlinear tapered beam splitters. (b) Detailed layout of a Si_3N_4 apodized grating coupler with four branches of nonlinear tapered beam splitters for coupling optimization of 21 μm of beam diameter and equal path line spreader from 5 μm to 26.856 μm. (a) Full-layout of a waveguide-arrayed DLA structure consisting of a Si_3N_4 apodized grating coupler with eight branches of nonlinear tapered beam splitters. (b) Detailed layout of a Si_3N_4 apodized grating coupler with eight branches of nonlinear tapered beam splitters for coupling optimization of 50 μm of beam diameter and equal path line spreader from 5 μm to 26.856 μm.

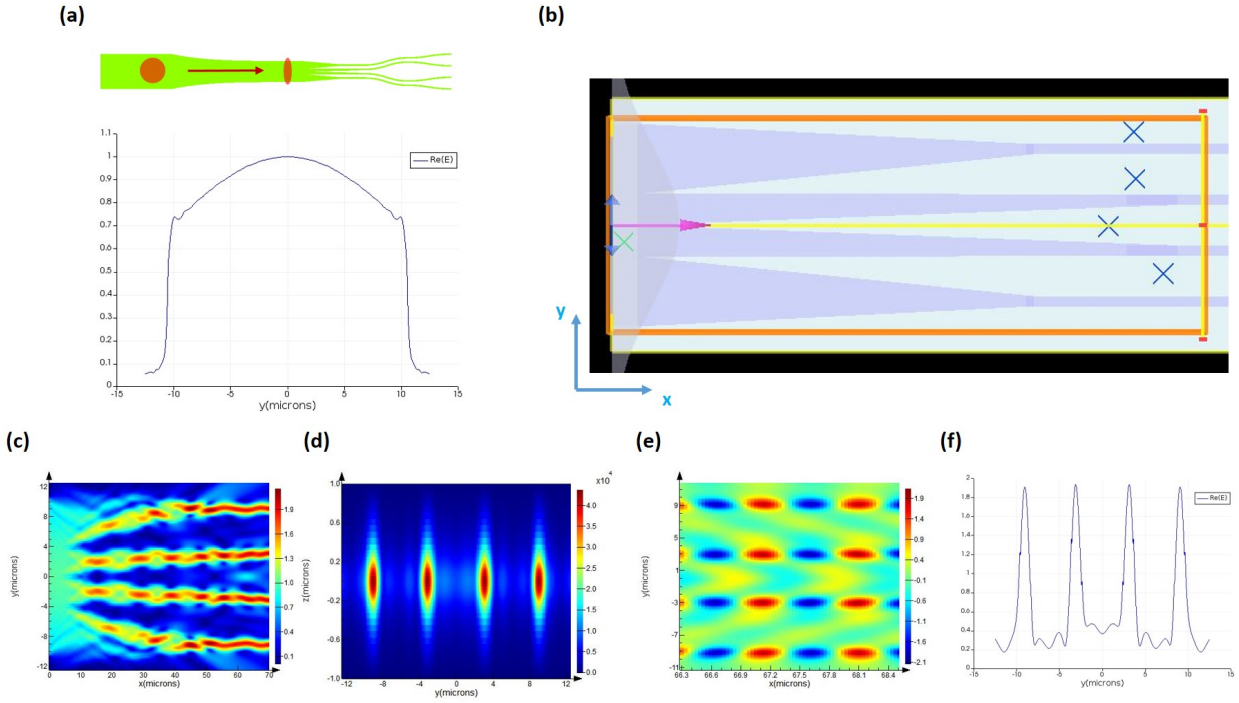

Figure 3.17. (a) Profile of input electric field intensity before splitting four branches of tapered waveguides. (b) A design of a Si_3N_4 splitting (four) of a tapered waveguide for discovering the optimized design through the 2.5D-FDTD simulation. (c)-(d) Simulated results of the optical power propagation of the optimized design with top-view (c) and cross-sectional view of output ports (d). (e) Simulated result of phase alignment at the same location on output ports. (f) 1D-profile of the result of the output electric field intensity distribution by four ports.

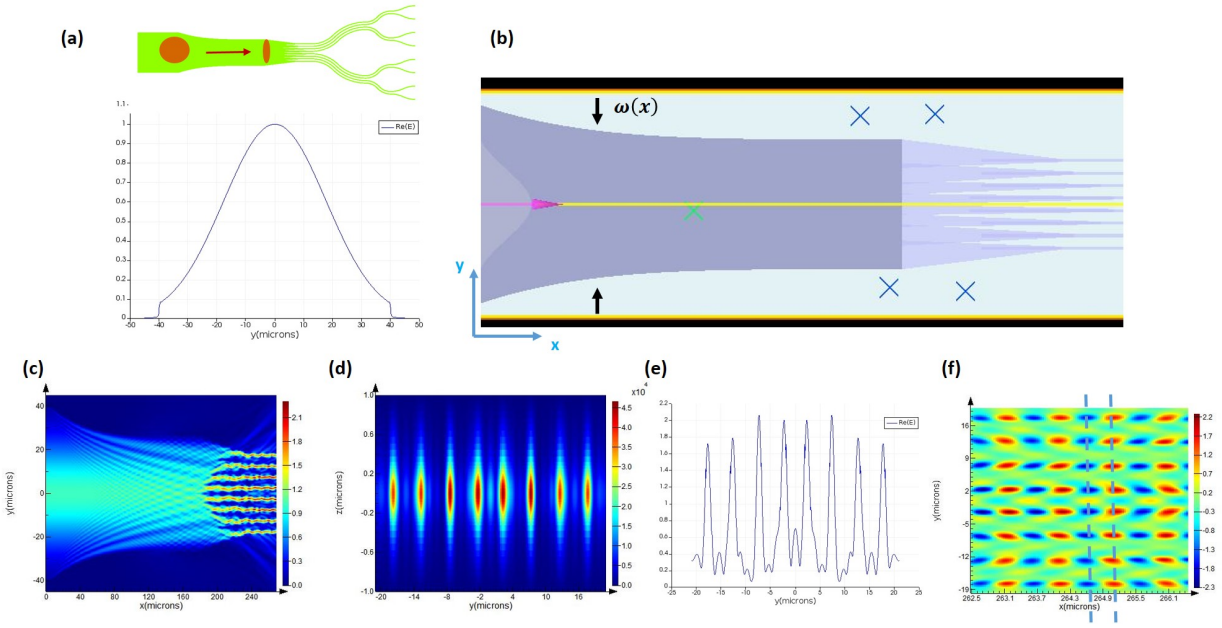

Figure 3.18. (a) Profile of input electric field intensity coupled with 50 μm of beam diameter by an apodized Si_3N_4 grating coupler. (b) A design for a Si_3N_4 slab of a nonlinear tapered structure with eight branches of splitters for discovering the optimized design through the 2.5D-FDTD simulation. (c)-(d) Simulated results of the optical power propagation of the optimized design with top-view (c) and cross-sectional view of output ports (d). (e) 1D-profile of the result of output electric field intensity distribution by eight ports. (f) Simulated result of phase alignment at the same location on output ports.

4. DEVICE FABRICATION PROCESSES AND RESOLUTIONS OF CHALLENGES

4.1 Fabrication processes of silicon nitride to silicon hybrid waveguide array

4.1.1 Fabrication of alignment marks on SOI substrate

To fabricate the silicon nitride to silicon hybrid waveguide array structures, fabricating alignment marks on the SOI substrate are critical due to the alignment writing concerning the exact coordination of the layout by a lithography process. In photonic integrated circuit applications, stoichiometric Si_3N_4 material is widely used due to its low propagation loss and broad transparency range when used for waveguide components. The stoichiometric Si_3N_4 deposition process is mostly used in a low-pressure chemical vapor deposition (LPCVD) process due to its purity, low defects, and uniform way of coverage. The LPCVD process should run at a high temperature (900 °C or higher) to acquire silicon from the reaction of dichlorosilane (DCS) and ammonia (NH_3) gases. Commonly, materials selected to make alignment marks in e-beam lithography processes are metals, such as gold or platinum, and are often used in semiconductor fabrication processes for higher contrast rates of reflection from the substrate while the e-beam scans the position of the alignment marks. However, such metals are not sustainable with the high temperature of LPCVD silicon nitride deposition. Therefore, instead of using metals for fabricating alignment marks, etched alignment marks are required for silicon nitride to silicon hybrid structures. The depth of their mark is also critical for writing multi-layered structures since depth contrasts effects for e-beam scanning while finding the alignment marks. Generally, these structures require approximately 1 μm of depth. To fabricate our silicon nitride to silicon hybrid waveguide structure, the depth was deeper than 1 μm because, first, it is difficult to contrast with reflected electron beams while e-beam is writing a silicon nitride layer due to the thick dielectric layer of deposited films and BOX, and second, for writing a Si_3N_4 waveguide array with e-beam lithography, we used a thick-layered hydrogen silsesquioxane (HSQ) negative-toned e-beam resist, however, its chemical properties are similar to silicon dioxide; thus, contrasting e-beam scanning is much more difficult than with conventional CMOS fabrication processes. Therefore, the

depth of etched alignment marks on the SOI substrate requires at least 1.5 μm, considering the film deposition height and HSQ resist. Figure 4.1 indicates the size of the SOI substrate (a), the shapes and depth of the alignment marks ((b) and (c)), and the shapes and positions of the vernier marks (d). We used 35 mm by 35 mm of SOI pieces to fabricate the hybrid structures. For an e-beam writing system, we needed two sets of alignment marks for the precise alignment writing: one is called a "global mark" and the other is called a "chipset mark". Global marks, which have cross marks with 10 μm of their width and 1 mm of their length, are placed on the middle of each side of the piece. Concerning the issue of stitching errors from the e-beam lithography system, we divided the writing area into 16 places, each 7 mm by 7 mm, and chipset marks were placed at the middle of each writing area, with the cross mark that had 2 μm of width and 100 μm of length, as in Figure 4.1 (b). Those alignment marks had over 1.5 μm of depth (see Figure 4.1 (c)). To measure any misalignment of the lithography process, we placed the vernier marks on each corner of the writing areas for silicon, Si_3N_4, and gold patterns in both x and y directions. These vernier marks can measure at least 100 nm of discrepancies. Figure 4.1 (d) shows their shapes and placements.

First, we spun the photoresist on top of the SOI substrate for protecting any debris or particles while running the dicing process. Then, we diced 35 mm by 35 mm of SOI pieces from 8 inches of the substrate and then cleaned the piece with both solvent and RCA cleaning. To fabricate etched alignment marks, we choose to write them with an e-beam lithography instead of optical lithography tool for the positioning sensitivity of alignment between the silicon waveguide to Si_3N_4 waveguide. It is difficult to fabricate such etched alignment marks using e-beam lithography as a typical photoresist has higher chemical selectivity than that of a typical e-beam resist. Thus, we spun the PMMA with 2000 rpm to achieve approximately 2 μm of its thickness and then soft-baked it at 180 °C for 90 seconds. Then, we wrote the alignment marks with the dose of 2200 $\mu C/cm^2$ of the e-beam lithography. After finishing the e-beam writing, we developed PMMA using the solution of MIBK: IPA 1: 3 for 2 minutes and then put the piece onto the hot plate and baked it again at 100 °C for 1 minute due to hardening the PMMA resist for increasing the chemical resistance while etching. We used a reactive ion etching (RIE) process to fabricate etched alignment marks since this process can achieve the anisotropic shape of the etched geometry. We used SF6 chemical

first to minimize the resist reduction while etching the silicon area. Then, we used a RIE etching process with CHF_3 and O_2 chemicals for deep etching a BOX layer. To achieve a deep anisotropic directional etching of silicon dioxide layer with PMMA applied surface, we changed some parameters for plasma generation. For example, we set the RF source power as 525 W and RF bias power as 50 W. Additionally, O_2 usually induced faster etching conditions to the organic materials but it was necessary to hamper the organic residue depositing onto the etched area; thus, we used 2 sccm while etching silicon dioxide and we used CHF_3 as 40 sccm. Finally, we achieved more than 1.5 μm of anisotropically etched marks, sustaining the selectivity between PMMA and SiO_2 as a 1:1 ratio. To remove PMMA, we used the solution Remover PG for more than 10 minutes and soaked the piece in Piranha solution (a mixture of sulfuric acid (H_2SO_4) and hydrogen peroxide (H_2O_2)), a strong acid solution that can clean any organic residue on the substrate, to prepare for the fabrication of silicon waveguides. The Piranha solution cleaning process is necessary when fabricating e-skid fin structures as the solution helps silicon surfaces to maintain a hydrophilic state [48], which increases adhesion between the silicon surface and HSQ so that the patterns of narrow-sized fin structures written by e-beam lithography do not fly away while in the development process. The whole process for fabricating etched alignment marks on the SOI substrate is shown in Figure 4.2.

4.1.2 Fabrication steps of silicon nitride to silicon hybrid waveguide array

Once the SOI piece was prepared by the fabrications of etched alignment marks and the Piranha cleaning process, we began fabricating the silicon and silicon nitride hybrid waveguide structures. Figure 4.3 presents the fabrication flow of the hybrid structure. First, we spun the e-beam resist of XR-1541-004, which was 4 % of HSQ resist diluted in MIBK solution, with 6000 rpm. This spin rate produced the thickness of HSQ as 60 to 70 nm. Then, the HSQ was heated to 120 °C for 3 minutes on a hot plate for soft-baking. The soft-baking process was critical not only for drying out the solvent inside the resist but also for increasing the adhesion between the silicon film and the resist. After preparing the HSQ resist on top of the SOI piece, we began writing the patterns for the silicon waveguide array

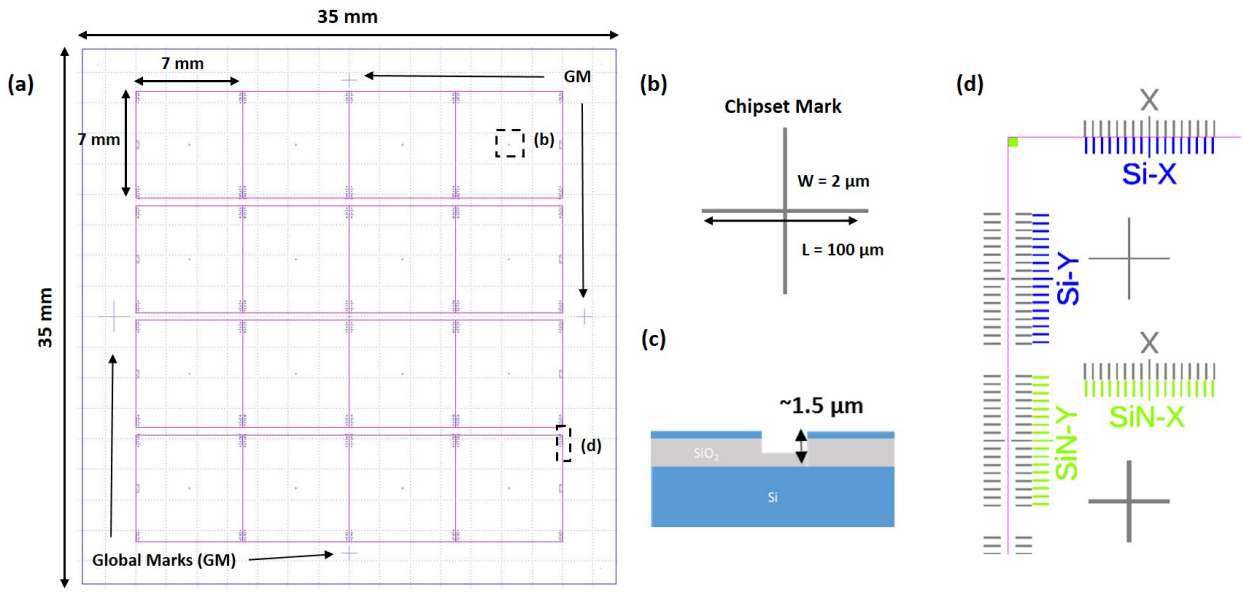

Figure 4.1. (a) Layout of alignment marks and the positions on SOI. (b) Design of each chipset mark. (c) Cross-sectional illustration of the etched depth of the alignment marks on SOI. (d) Detailed layout of vernier scales engraved on each corner of the writing field on SOI.

with the base dose of 900 μC/cm^2 with the customized proximity effect correction (PEC). After finishing the writing, we developed the HSQ resist with 80-second immersion in a solution of 25 % Tetramethylammonium hydroxide (TMAH). The reactive ion etcher was also used for etching the silicon. At this time, we used the chemical gases of Cl_2 and O_2 for etching the silicon waveguide due to the higher selectivity between silicon and HSQ resist, and the increments of anisotropicity of the waveguide geometry. For removing the residue of HSQ resist, we immersed the sample into the solution of 6:1 buffered oxide etch (BOE) for 5 seconds and then rinsed the sample with distilled water.

The next step after finishing the fabrication of the silicon waveguide structure was to deposit the inter-layer on the silicon dioxide. We used a low-temperature oxide (LTO) process to deposit the silicon dioxide for the inter-layered film due to its low step coverage. This process is discussed in detail in the next chapter. After depositing silicon dioxide approximately 150 nm into the inter-layer film, we deposited the stoichiometric silicon nitride (Si_3N_4) using an LPCVD process until reaching a thickness of 300 nm. We again ran e-beam lithography to write the Si_3N_4 waveguide structures. To fabricate the Si_3N_4 waveguide, we

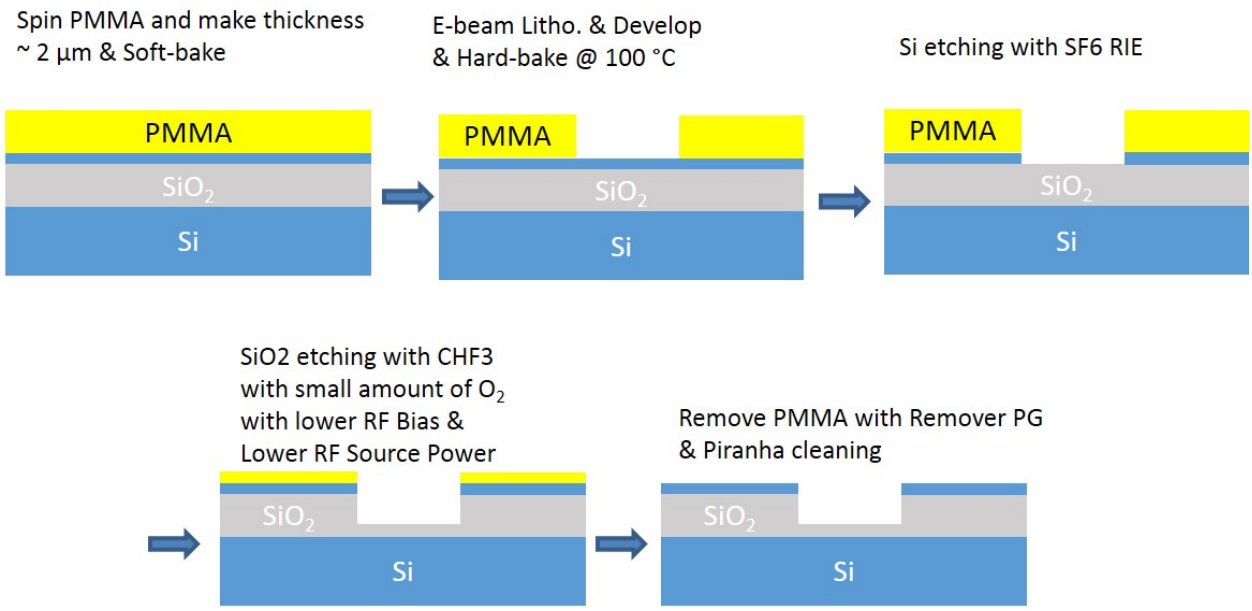

Figure 4.2. Fabrication process of alignment marks on SOI.

used the e-beam resist of Fox-16, which can produce a thicker HSQ resist, with a spin rate of 8000 rpm; we achieved 600 nm of its final thickness. Similar to the preparation of XR-1541, we soft-baked it at 120 °C for 3 minutes on a hot plate and wrote the patterns for the Si_3N_4 waveguide structures using the base dose of 1100 $\mu C/cm^2$ with the customized PEC applied. We used the chemical gases CHF_3 and O_2 with a RIE process to build fully etched Si_3N_4 waveguide structures. Any remaining Fox-16 after etching the Si_3N_4 waveguide was removed by immersing it into BOE solution for approximately 10 seconds and then rinsing the sample with distilled water. Figure 4.4 presents the alignment results of Si and Si_3N_4 waveguides. Figure 4.4 (b) and (c) show the scanned electron microscopic (SEM) images of the result of alignments for both x and y directions with both Si and Si_3N_4 fabrication; the results indicate that both layers of the alignment writings were done with less than 100 nm of discrepancy. Figure 4.4 (e) and (f) show the hybrid mode couplers that were fabricated were well-aligned.

To deposit silicon dioxide as an upper cladding, we again put the sample into the LTO chamber and deposited it up to 2.5 μm. Since we also fabricated the layout of active devices, we needed to deposit a micro-heater structure on top of the upper cladding surface. This

Figure 4.3. Fabrication process flow of silicon nitride to silicon waveguide array.

required a lift-off process. Thus, we again span the AZ1518, a positive-toned photoresist, with 2000 rpm to achieve 1.8 μm of its thickness. Patterns of micro-heater structures were written by Heidelberg MLA150 Maskless Aligner, one of the optical lithography tools for direct writing systems. AZ1518 was developed by the solution of MF-26. Then, we deposited a gold film of approximately 300 nm using an e-beam evaporator, which can deposit metals uniformly. After finishing the gold deposition process, we immersed the sample into the acetone for over 12 hours before the lift-off process. Next, we rinsed it with methanol and isopropyl alcohol and, finally, we fabricated a U-groove structure to make optical fiber hold at the end. Figure 4.5 (a) and (b) show the optical microscopic images of the final fabricated devices of passive and active OPA-based LiDAR.

4.2 Trapping void gaps in e-skid fin layers

In an earlier chapter explaining the fabrication flow of silicon nitride to silicon hybrid waveguide structures, the height of 150 nm of an inter-layered SiO_2 film was deposited by

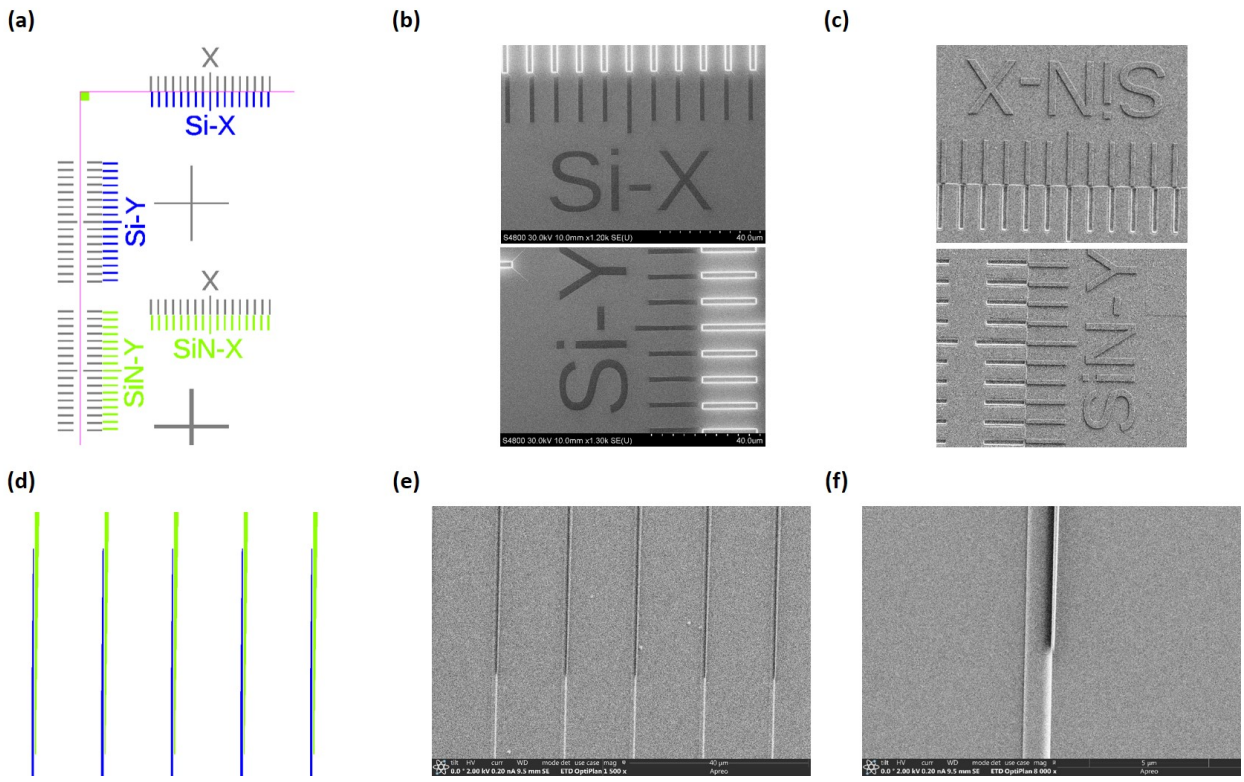

Figure 4.4. (a) The layout of vernier scales engraved on each corner of the writing field on SOI. (b)-(c) SEM images of fabricated vernier scales of both directions and both materials of silicon nitride and silicon. (d) The layout of Si_3N_4 to Si hybrid coupler arrays. (e)-(f) SEM images of the fabrication of the layout (d).

the low-temperature oxidation process. Deposition of silicon dioxide on the substrate with the LTO process used the gases of Silane (SiH_4) and O_2, with the following process reaction:

$$SiH_{4(g)} + O_{2(g)} \rightarrow SiO_{2(s)} + 2H_{2(g)}. \tag{4.1}$$

This reaction proceeded at a relatively low temperature, (400 °C at the highest), in the clean quartz furnace tube. The pressure ran at 5 mTorr. The reason for using the LTO process for the inter-layered SiO_2 film is, first, it produces very clean and conformal depositions among the substrates, and second, since it proceeded at a low temperature, the kinetic energy of the reactive species was relatively low and the species had low surface mobility [49]. Hence, the solid-state of generated SiO_2 tended to grow in the isotropic direction from the top surface of

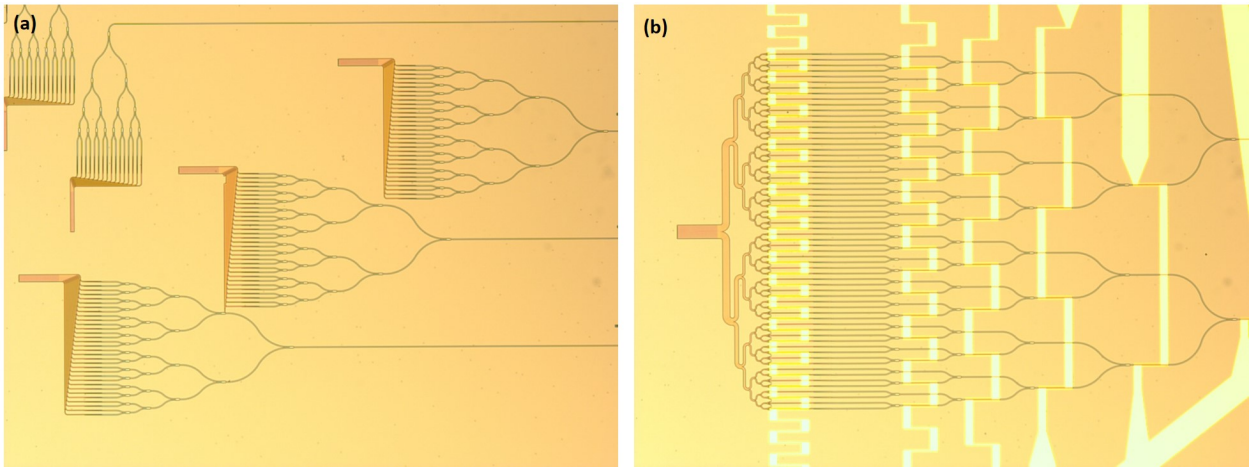

Figure 4.5. Optical images of completed fabrication devices of OPA-based LiDAR: (a) 32-channel L-shaped Si_3N_4 to Si hybrid OPA device and (b) 64-channel active OPA device.

e-skid fin arrays and the waveguides, and, gradually, increments of shadowing effects inside the grooves of fin arrays made it difficult for SiO_2 to grow at the surface of its sidewalls. Figure 4.6 describes the processes of depositing SiO_2 on top of e-skid fin array structures. As Figure 4.6 (b) shows, initially, isotropic grown SiO_2 on top of e-skid fin structures generates shadow effects inside the groove structures that hinder the deposition process further and we can fully trap the void gap in between the fin layered structures. Therefore, the e-skid array structures sustain the high refractive index contrast between silicon and the background to satisfy the anisotropic media and greatly reduce evanescent waves. The results of this deposit are shown in Figure 4.7 (a). Figure 4.7 (b) shows the trapped void gap between the fin structures.

4.3 Electron beam lithography challenges of dense arrayed patterns and their resolutions

Both OPA-based LiDAR and waveguide arrayed DLA structures a pitch array at least a half-wavelength range at the output on the silicon part. Designs should be made to combine the array from the large space to the half-wavelength space while keeping the same optical line paths. Thus, Figure 4.8 (a) is an example of 64 channels of combining waveguide array structures with e-skid platforms. Starting with 21 μm of the spacing between the adjacent

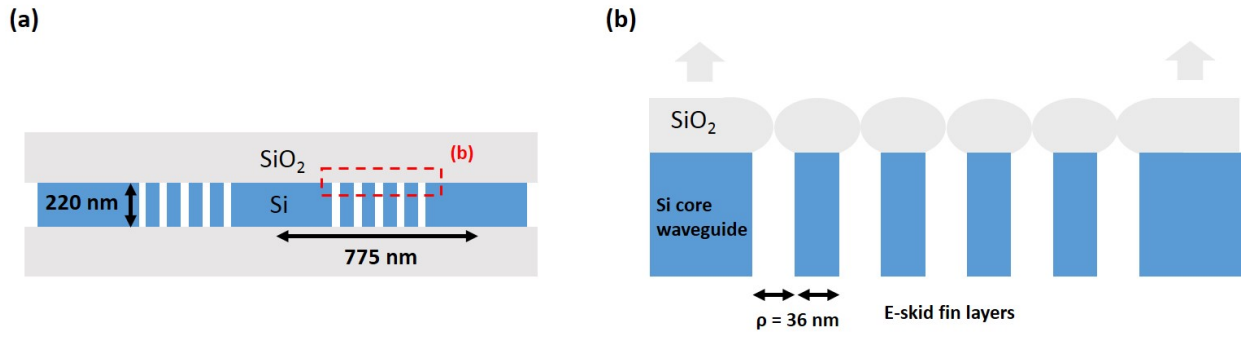

Figure 4.6. (a) Illustration of the trapped void gap in an e-skid waveguide array. (b) Zoomed-in illustration of the initial deposition process of SiO2 on top of the e-skid Si waveguide and its fin structures.

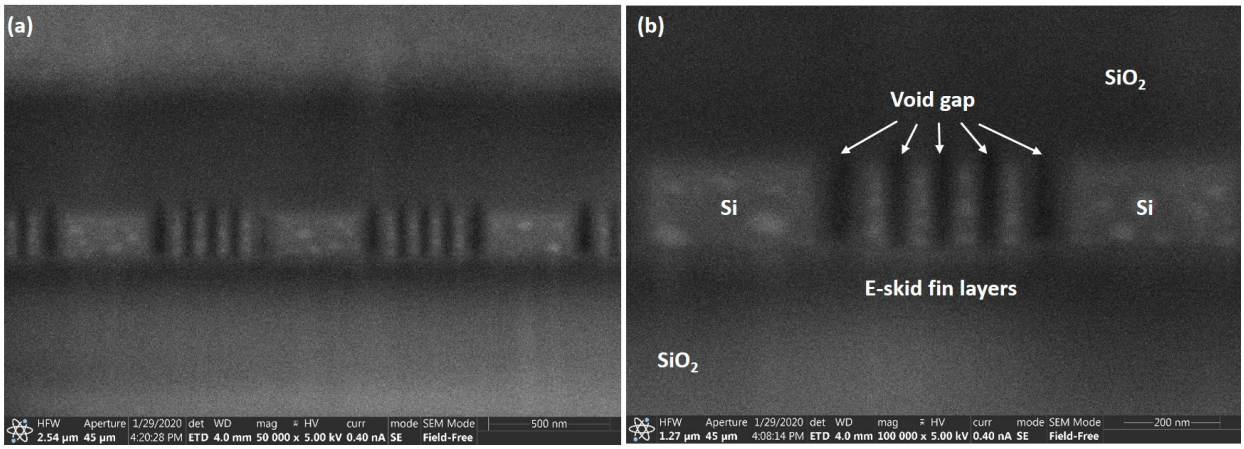

Figure 4.7. (a)-(b) SEM images of a cross-sectional view of the fabricated trapped void gap in an e-skid fin structure.

waveguides to install the microheaters' structures or apply the optical path delay line, each branch was combined with a half-wavelength pitch size and surrounded by the tapered e-skid fin arrays, as in Figure 4.8 (b). Then, a few steps of combining with adjacent arrays, like Figure 4.8 (c), and finally, 64 channels were combined into a single array with a half-wavelength pitch, and each waveguide branch was applied with sidewall gratings, as in Figure 4.8 (d) and (e).

Unlike the e-beam writing of a single or a few lines of optical waveguide structures, the combined waveguide array patterns are difficult to write using e-beam lithography because of the electron scattering effects. Once the focused electron beam hits the resist at the targeted

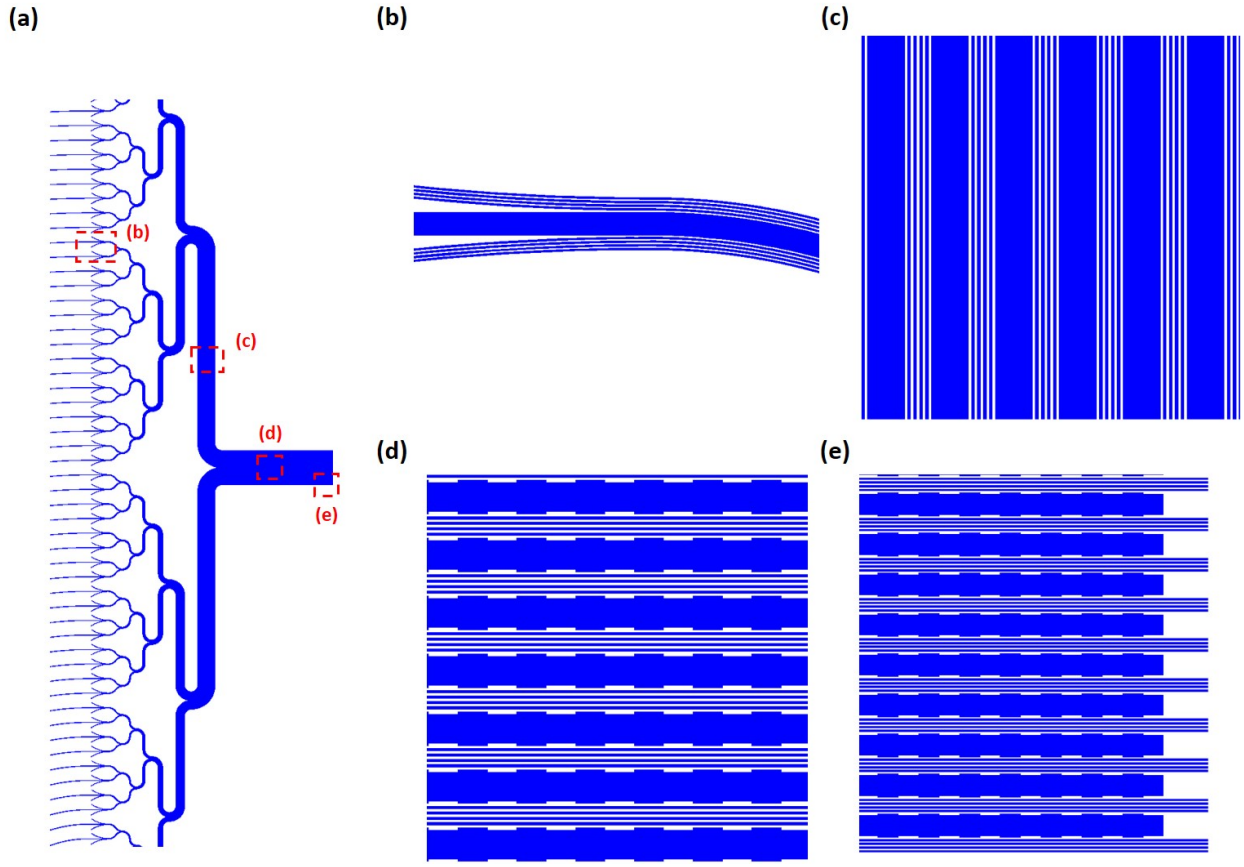

Figure 4.8. (a)Sample layout of an e-skid 64-channel combining array and grating emitters for fabrication optimization using e-beam lithography. (b) Layout image of an input waveguide array, starting with an e-skid fin structure. (c) Layout image of an e-skid waveguide array in the middle of a 32-channel combining array. (d) Layout image in the middle of 64 channels of an e-skid grating emitter array. (e) Layout image at the corner of 64 channels of an e-skid grating emitter array.

area, it scatters in the resist layer creating what is known as forward scattered electrons, then it scatters again in the film or substrate material beneath creating backscattered electrons. These scattered electrons create secondary electrons at the resist and substrate layers and these electrons influence the resist exposure and contribute to the total exposure dose. Therefore, some designs with dense patterns could be implemented imprecisely on a sample due to the over-exposure to the targeted patterns. This is known as the 'proximity effect' in the literature. Figure 4.9 (b) shows the scheme of the electron trajectories generating secondary electrons from scattering effects from both the resist and the substrate. This

proximity effect is related to an energy density profile deposited in the electron resist layer due to a point exposure (often called point spread function (PSF)) [50]. This profile is often described by the sum of two Gaussian distributions [50], [51]:

$$f(r) = \frac{1}{\pi(1+\eta)}\left(\frac{1}{\alpha^2}exp\left(-\frac{r^2}{\alpha^2}\right) + \frac{\eta}{\beta^2}exp\left(-\frac{r^2}{\beta^2}\right)\right). \tag{4.2}$$

In equation 4.2, the first term of α describes the effective area of energy density distribution due to the forward scattering effects from the resist. The second term of β describes the effective area due to the backward scattering effects from the substrates. The parameters of η describe the ratio of the backward scattering to the forward scattering component. These parameter values are variable with respect to the atomic numbers of resist, the materials of substrates, the thickness of both the resist and the films or substrates, the initial energy of the electron beam, and so forth. Commonly, these values are calculated by Monte-Carlo simulations and this simulation can be provided by commercial software such as CASINO or TRACER. The Monte-Carlo simulation provides the profiles of scattered electrons, as in Figure 4.9 (a), and we can obtain the parameters of each specific condition of e-beam lithography. For the fabrication of our silicon waveguides' array structure, we used the HSQ resist with its height of 60 nm on top of the SOI substrate, which had 220 nm of silicon thickness on top of 2 μm of a silicon dioxide buried layer. In this case, the typical values of PSF were α as 2 nm, β as 29.53 μm, and η as 0.65. However, once we had written the e-beam lithography with the given patterns of Figure 4.8, we did not have the right patterns. . The e-beam writing results of the SEM images of the following conventional PSF parameters are shown in Figure 4.10. Figure 4.10 (a) corresponds to the image from Figure 4.8 (b), Figure 4.10 (b) shows in the middle part of 32-channels of e-skid array, corresponds to Figure 4.8 (c), Figure 4.10 (c) is the results of e-beam writing in the middle of 64-channels of grating emitter array, corresponds to the layout of Figure 4.8 (d), and Figure 4.10 (d) refers to the written results of the pattern at the end of the corner of 64-channel array structures that came from the layout of Figure 4.8 (e). Although we used the underdose of HSQ being chemically reacted from the electron energy, the exposed patterns in the large and dense areas, such as the 64-channel array of e-skid grating emitter structure (shown in Figure 4.10

(c)), was over-exposed so that all of the features inside the area stuck together. Therefore, we needed to resolve this issue.

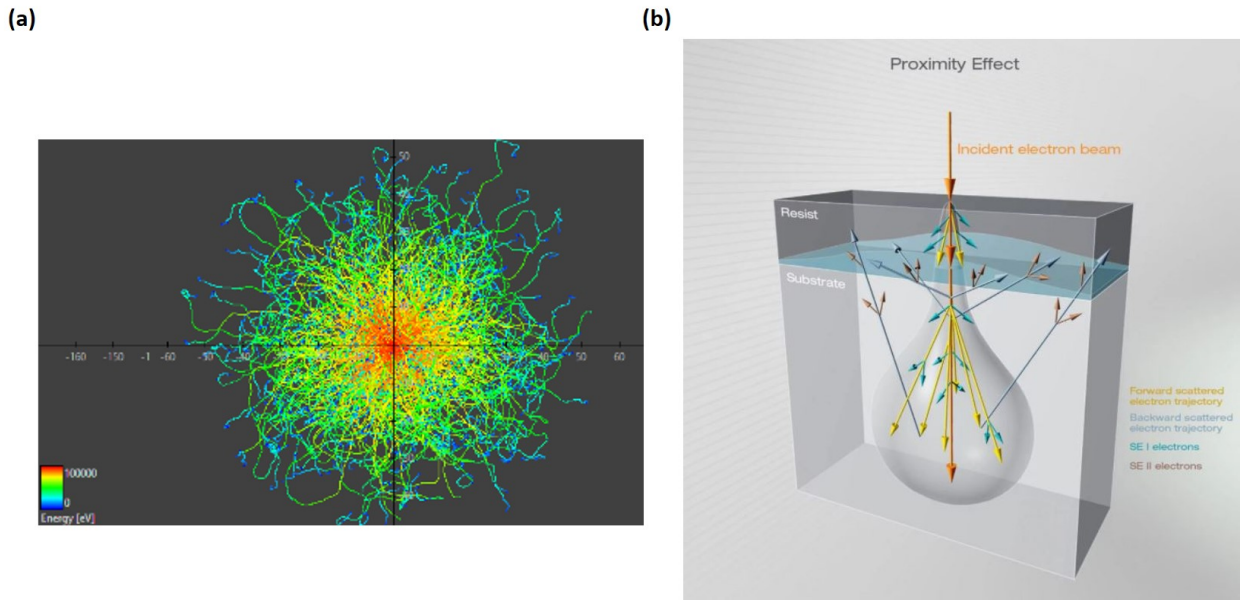

Figure 4.9. (a) 2D-profile of electron density distribution from the input electron beam, retrieved from the Monte-Carlo simulation results of SOI substrate. (b) Illustration of the electron generation from the forward and backward scattering effects by the resist and the substrate from the incident electron beam [52].

4.3.1 Characteristics of HSQ

To solve the problem of e-beam lithography writing of a large e-skid combining array with given PEC parameters, we needed to examine the characteristics of HSQ. HSQ is an inorganic compound used for negative-toned e-beam resists. Due to its high resolution and silica-like chemical compound, it is widely used for fabricating on-chip waveguide structures. Before exposing the electron energy to HSQ, it forms a cage structure, as in Figure 4.11 (a), and maintains a liquid state. Once it is exposed to electron energy, the cage-shaped chemical turns into a network form, as in Figure 4.11 (b), and transforms to a solid state [53]. However, it is not only reacted from the energy of electron beam, but also influenced by thermal energy. Sookyung Choi et al. (2018) demonstrated HSQ with thermal curing,

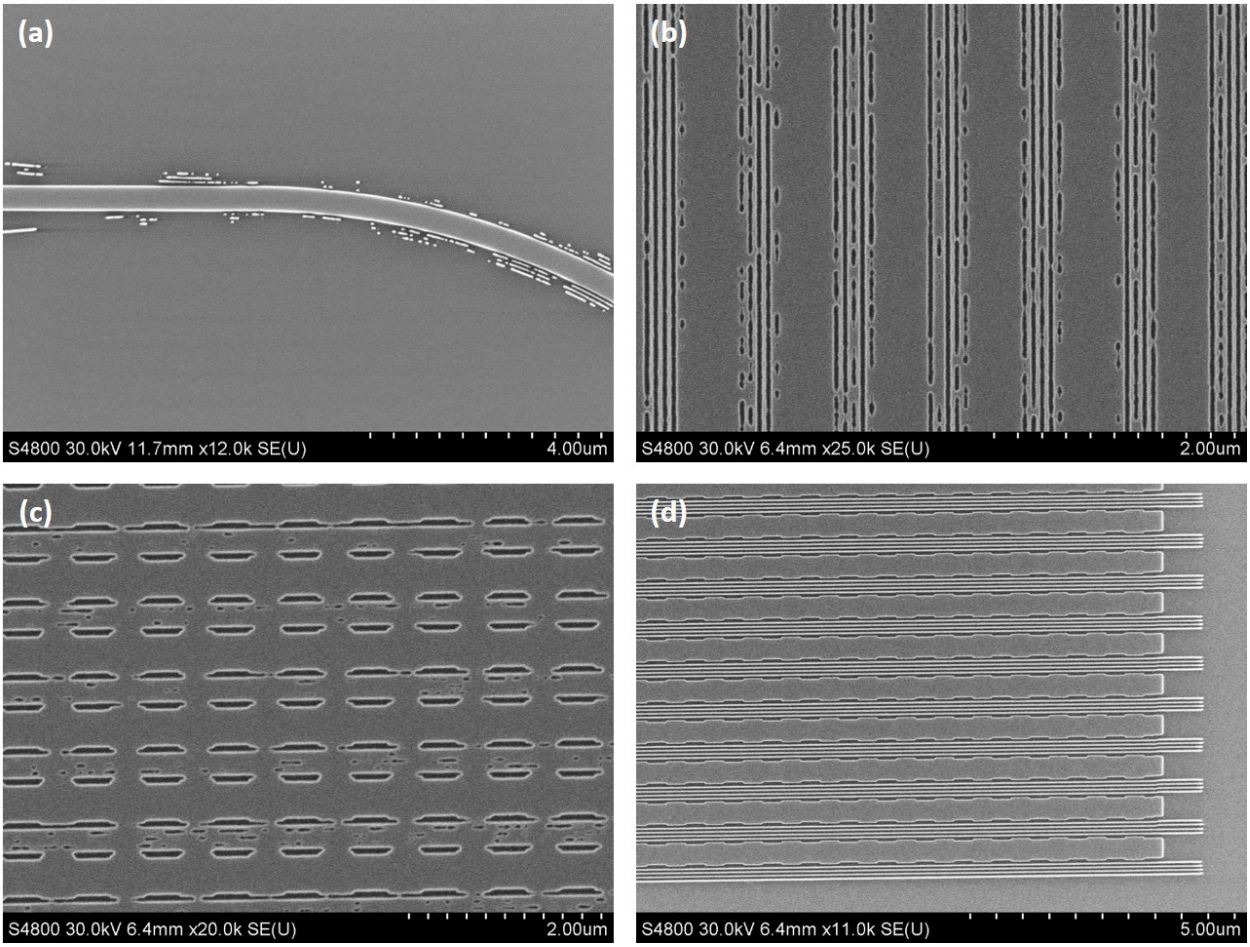

Figure 4.10. SEM images of error results of writing the layout of the Figure 4.8 using e-beam lithography with original PEC applied.

which produced a similar behavior of chemical bond distribution as with electron curing [54]. Figure 4.11 (c) and (d) present the measurements of the Fourier transform infrared (FTIR) spectrum of thermally cured and electron-beam-exposed HSQ film. Comparing the curing results of igure 4.11 (c) and (d), spectrum results of HSQ cured at 1200 μC/cm^2 of electron-beam exposure corresponds to that of the thermal curing process at 500 °C. This result implies our soft-baking process of HSQ at the temperature of 120 °C increased reaction energy levels with respect to the energy of electron beam exposure. Approximately 120 °C during soft-baking influenced HSQ, approximately 300 μC/cm^2 of the dose on its whole surface.

4.3.2 Customized proximity effect correction and dose assignments

The Monte-Carlo simulations did not record such thermal effects. Therefore, we needed to modify the parameters of PSF manually. In the aspect of pattern writing, increasing the reactive energy level via soft-bake temperatures can be considered the backward scattering effect in PSF. This means we should increase the value of η in equation 4.2 so that the backward scattering effects have a more significant role in the PSF of input electron energy. Figure 4.12 (a) shows the plot of energy densities that are changed by the value of η from 0.65 to 1.3 of the condition of 60 nm of HSQ on SOI substrate. Figure 4.12 (b) shows the results of the contour plot of dose distribution of the 32-channel silicon-only OPA-based passive LiDAR device after PEC was implemented by changing the value of η from 0.65 of original PSF to 1.1. Once the η value increased in the PSF, the effects of secondary electrons from backward scattering increased in the β (which is approximately 30 μm of radius from the main beam) so that more dose variations were required to write the dense pattern.

The results of writing the dense pattern on the SOI substrate were successful, increasing the value of η of PSF for proximity effect correction. The SEM images of Figure 4.13 came from the writing of same pattern shown in Figure 4.10. From sparse patterns of a single e-skid waveguide (a) to the middle of large and dense array patterns in (d), all the arrayed sections were well written by changing the value of η to 1.1. Not only the structures of the part of Si waveguide but the waveguide structures with silicon nitride were also successful after modifying the value of η. To fabricate the waveguide structure with Si_3N_4, wwe used the resist of HSQ with a much thicker height (approximately 600 nm), as discussed in Chapter 4.1.2. Thus, the values of PSF for correcting the proximity effect were also slightly different. The original values of PSF with the 600 nm of HSQ on top of 300 nm of Si_3N_4 on 2.3 μm of SiO_2 were as follows: the value of α was 6 nm, the value of β was 29.58 μm similar with SOI condition, and the value of η was 1.1 from the TRACER simulator. However, we increased the amount of the increment value of η as 0.4 from Si waveguide fabrication, we increased the value of η to 1.5 for fabricating Si_3N_4 waveguide structure due to the same conditions of soft-baking at 120 °C. Following this, the difference could be observed from the fabrication results of the Si_3N_4 grating coupler in waveguide-arrayed DLA structure; the SEM images of

those contrast are shown in Figure 4.14. Figure 4.14 (a) is a SEM image of the HSQ resist of the apodized grating coupler area for Si_3N_4 after its development with the base dose of 1000 $\mu C/cm^2$ with an original PSF value of η as 1.1. The written pattern of the middle of the grating coupler region seems blurred due to overexposure to that region. The SEM images of Figure 4.14 (b) to (f) are the SEM images of same fabrication condition of (a) but with a modified the value of η as 1.5. The results show that the blurred image in (a) did not show in the result of (b), and once we zoomed in on the entrance region of the grating coupler, we could clearly observe the groove of the etched line, which was approximately 80 nm of its width, in the dense pattern with 600 nm of the height of the HSQ resist. Modifying the value of η also clearly generate the 1x2 MMI components and curved wavguide of Si_3N_4 at the same time.

4.3.3 Stitching error issues and how we fixed them

Although the dense patterns of the waveguide arrays were well-defined by modifying the PSF parameters, disconnection issues with the long waveguide array structures also occurred in the e-beam lithography process, although the substrate had alignment marks. The SEM images in Figure 4.15 show an example of the disconnection issues. These were not related to the pattern density but occurred near the boundaries of the e-beam writing field. These kinds of issues are known as "stitching errors" in the literature. There are several causes for field stitching errors in e-beam lithography and these are mostly due to the mechanical imperfections of stage movements [55]. Approximately 20 to 50 nm of pattern offset occurred in our electron beeam lithography (EBL) system. We added two more steps to solve this stitching error. First, we used the technique of dose splitting and overlapped field boundary exposure during the pattern fracturing process. Figure 4.16 (a) and (b) describe the fracturing and dose assignments. Since BEAMER software has multi-functions to prepare patterns and assign doses with each specified fractured structure, we chose 200 nm of the patterns at the field boundary region and assigned only half of its original dose for one writing field to expose. We then overlapped the 200 nm of the selected area and assigned the other half of the original dose to the next writing field to expose. This technique

was able to fabricate waveguide arrays without disconnection. Additionally, since most of the stitching errors came from the imperfect stage movement of the writing field, we added another technique to minimize the movement of the writing field. BEAMER is also capable of assigning the writing field movement and its position concerning the pattern area. Even if the writing field area were assigned as 1 mm by 1 mm of the square region, we could overlap these fields following the geometry of the structure and reduce the physical movement of the stage while e-beam writing the patterns, as in Figure 4.17. This kind of assigning field movement and writing order is called 'follow geometry'. With these two techniques for pattern writing preparation, we finally fabricated large dense arrayed patterns without any discontinuity or over-exposure effects. The final SEM images of the fabricated structures of silicon waveguide arrays are shown in Figure 4.18.

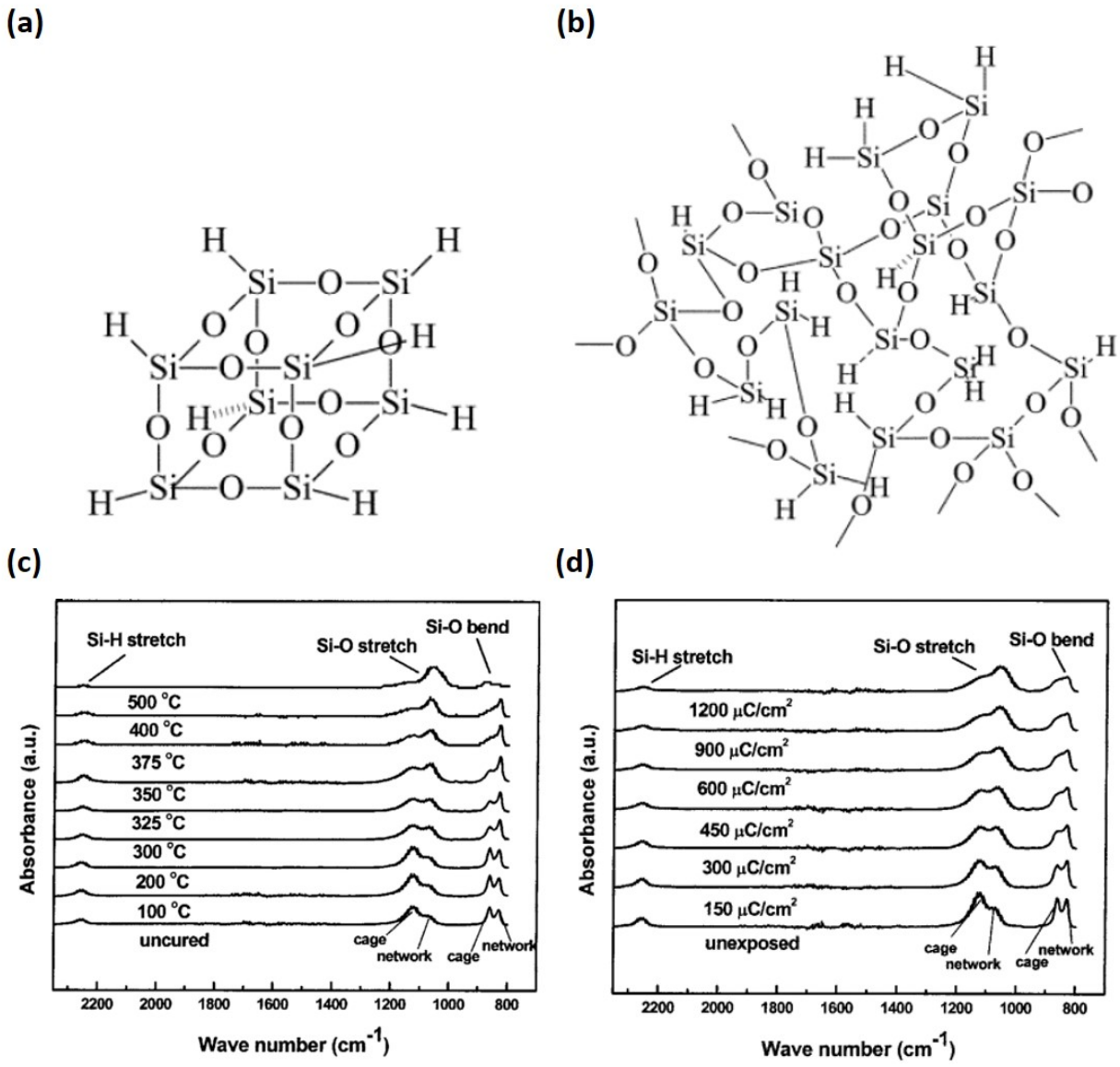

Figure 4.11. Chemical structure of HSQ: (a) cage-form and (b) network-form [53]. (c) FTIR absorption spectra of thermal curing HSQ and (d) FTIR absorption spectra of electron-beam-exposed HSQ [54].

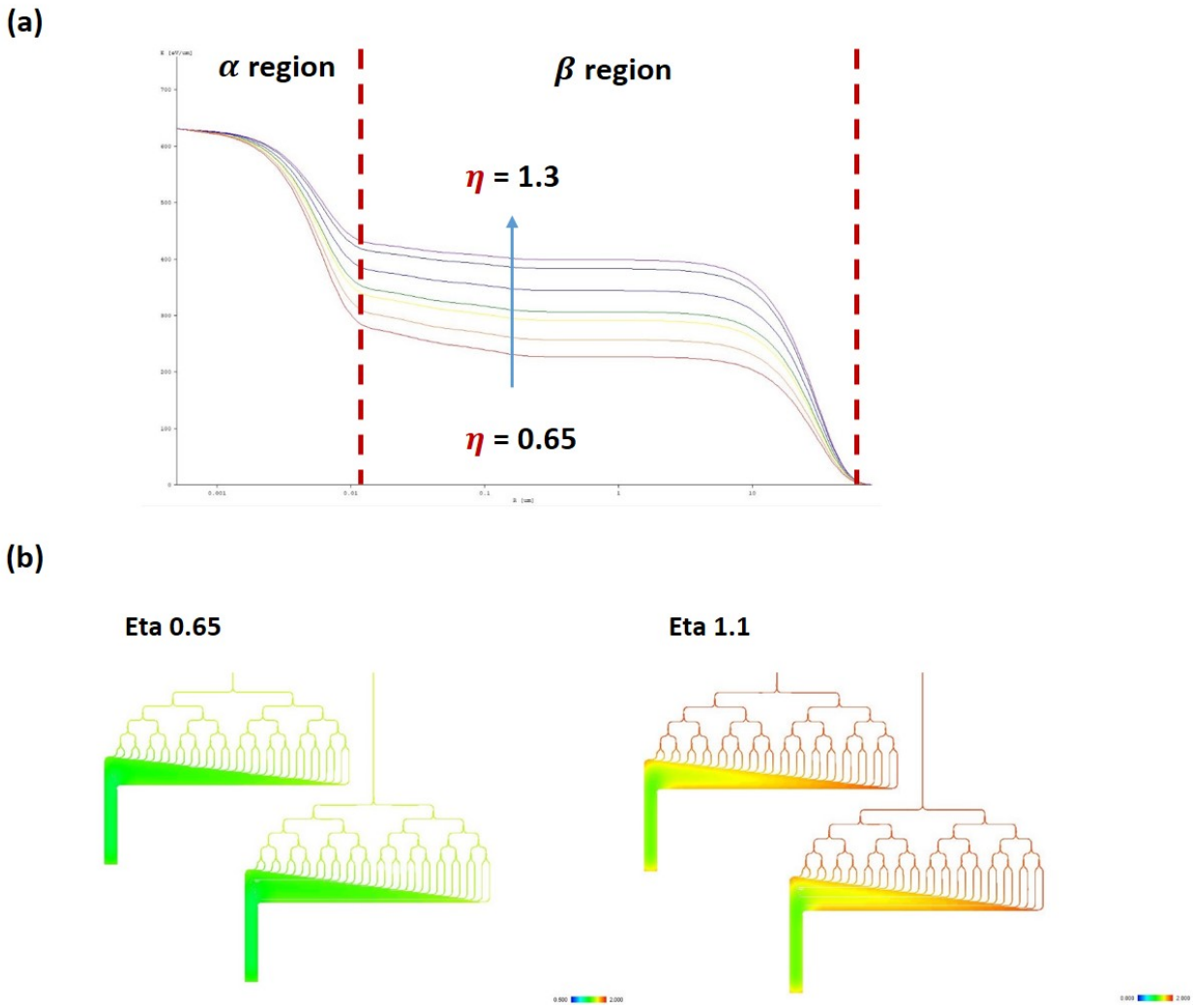

Figure 4.12. (a) Plot of different values of η from 0.65 to 1.3 of double-Gaussian energy density distribution with respect to the logarithmic distance from the incident electron beam. (b) Results of different electron dose distributions by the value of η of 0.65 (original PEC value) and η of 1.1 for manual modification.

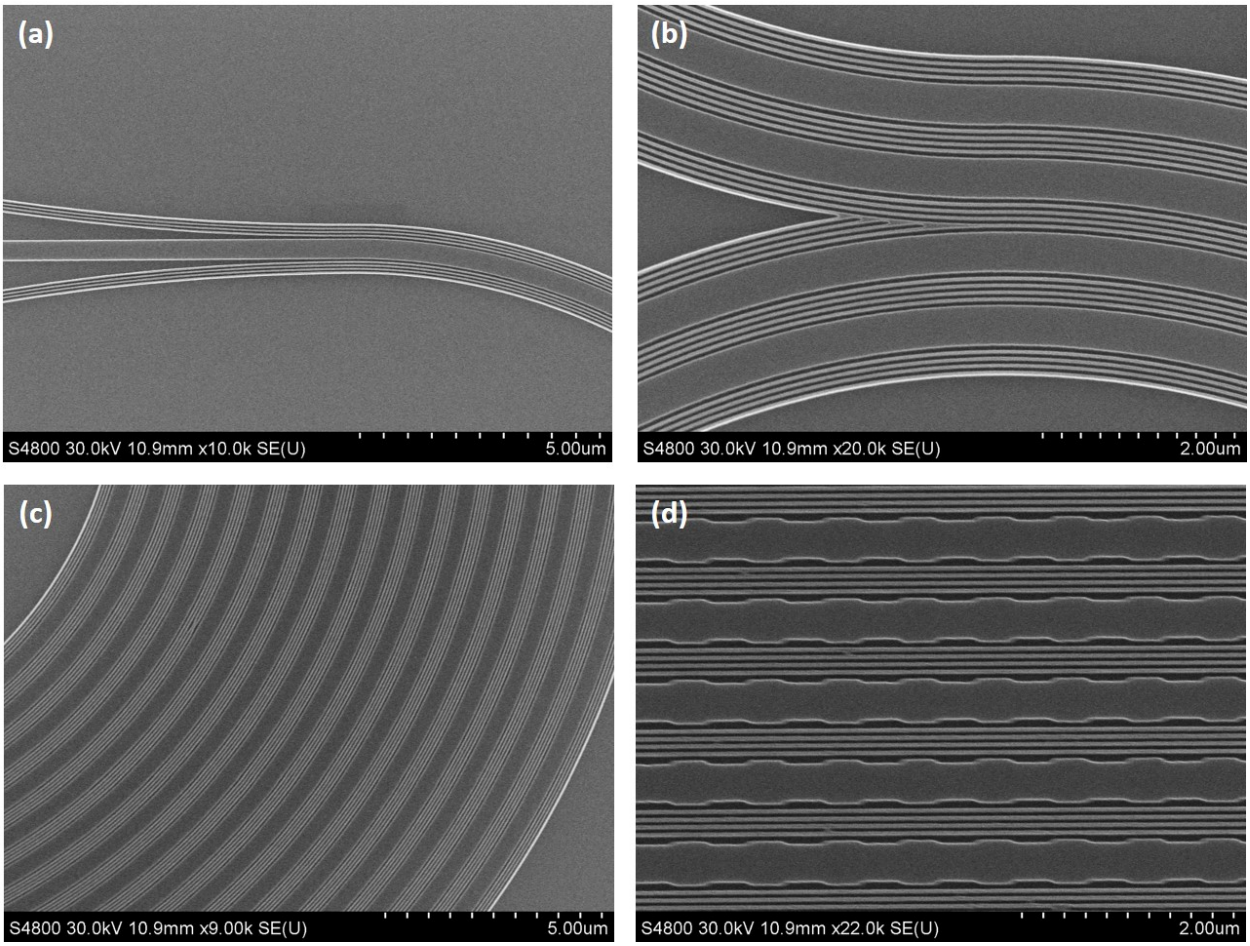

Figure 4.13. SEM images of the final e-beam writing of Figure 4.8 utilizing the PEC customization.

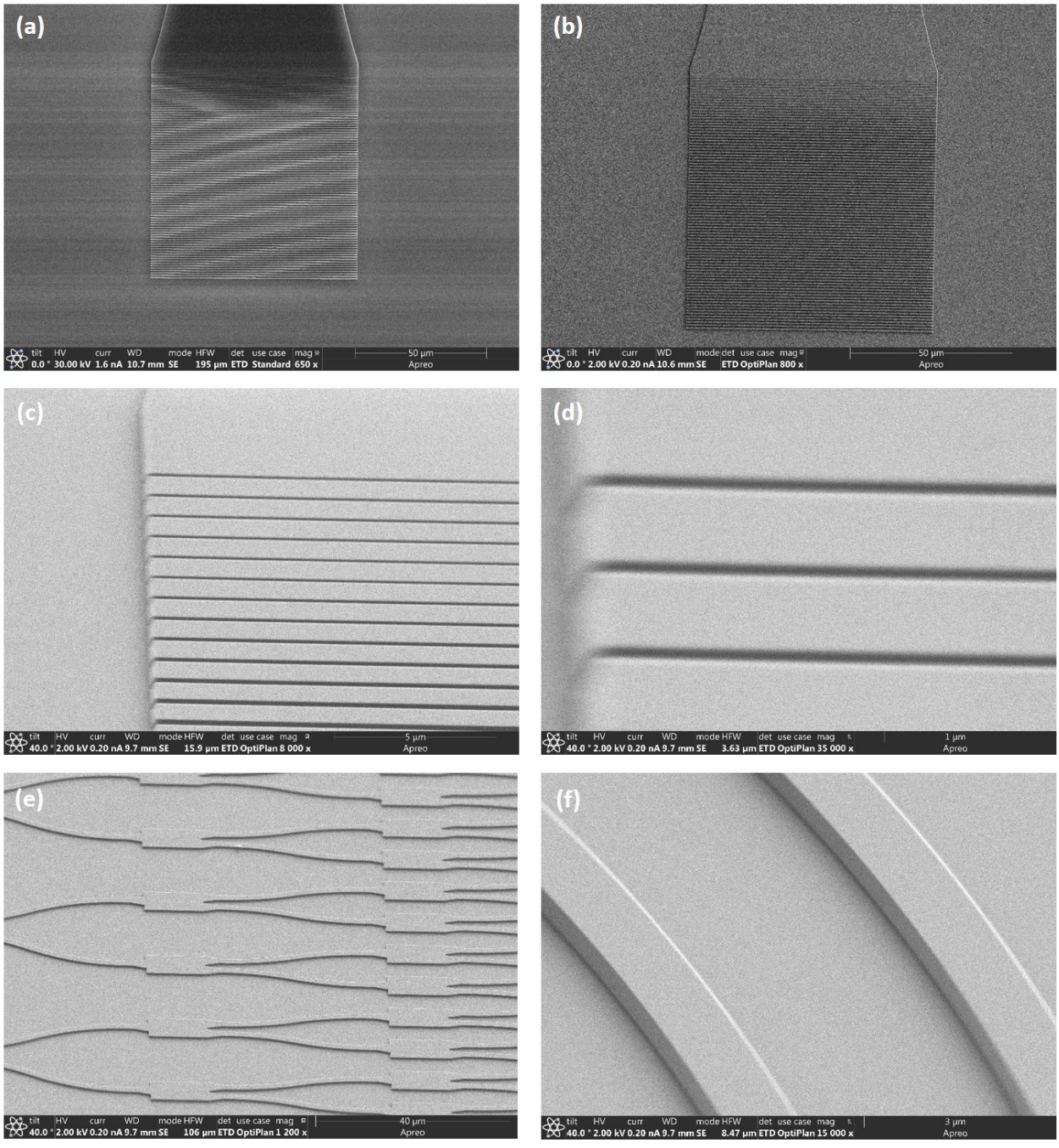

Figure 4.14. (a) (a) SEM image of the e-beam writing result of an apodized Si_3N_4 grating coupler on thick HSQ using the original value of PEC ($\eta = 1.1$). (b)-(d) SEM images of e-beam writing results of an apodized Si_3N_4 grating coupler on thick HSQ with modifying values of PEC ($\eta = 1.5$). (e) Tilted SEM image of e-beam writing on thick HSQ of cascaded Si_3N_4 1x2 MMI tree splitters. (f) Tilted SEM image of e-beam writing on thick HSQ of curved Si_3N_4 waveguides

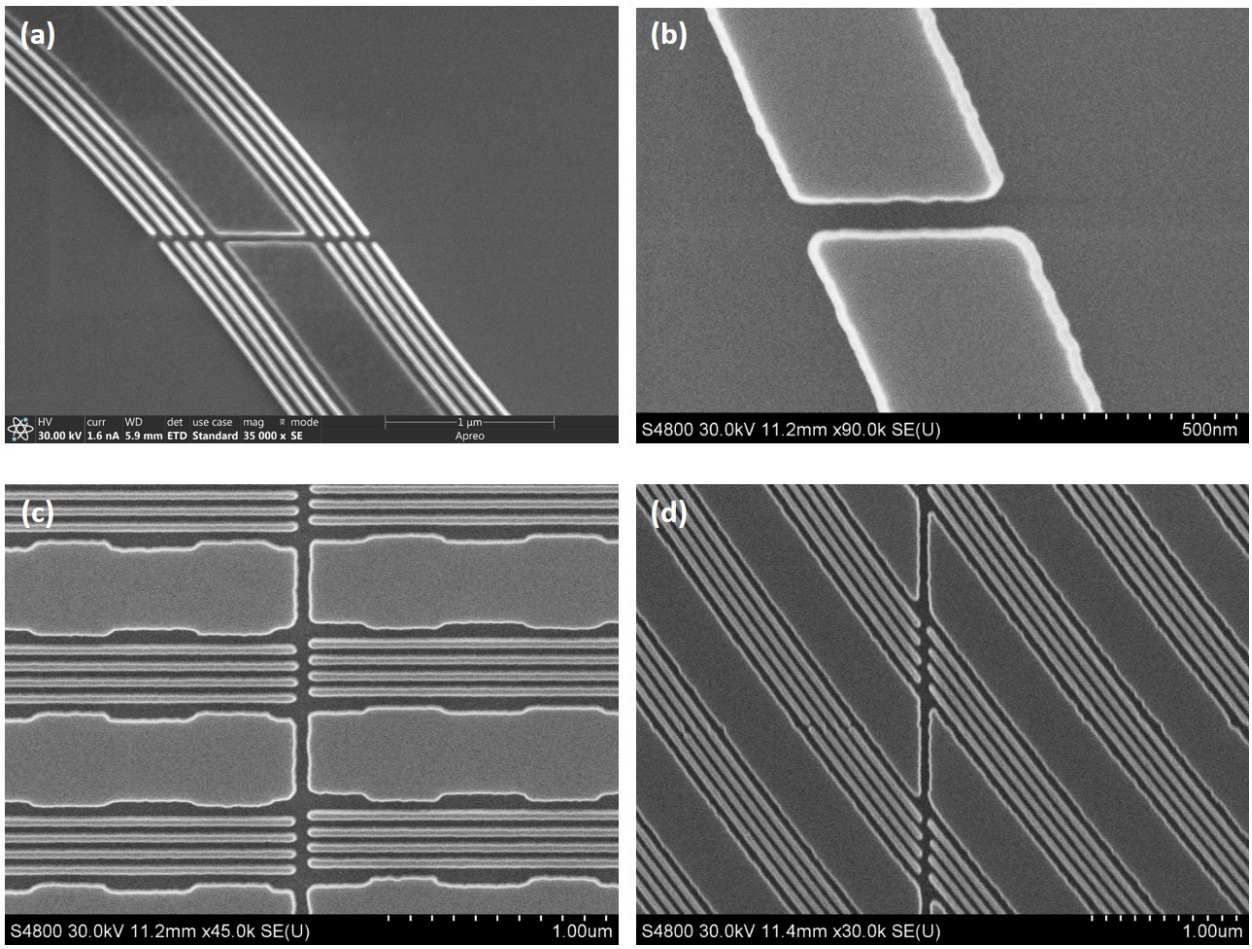

Figure 4.15. SEM images of the examples of stitching errors.

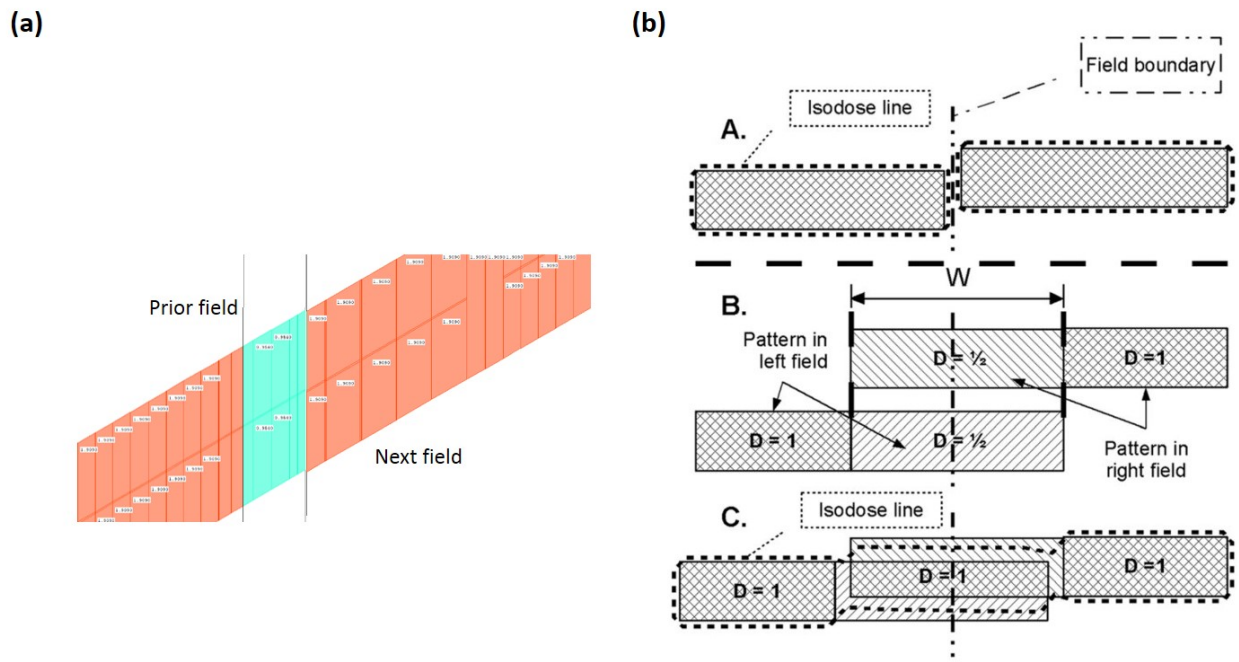

Figure 4.16. Illustrations of splitting dose effects at the field boundary [55].

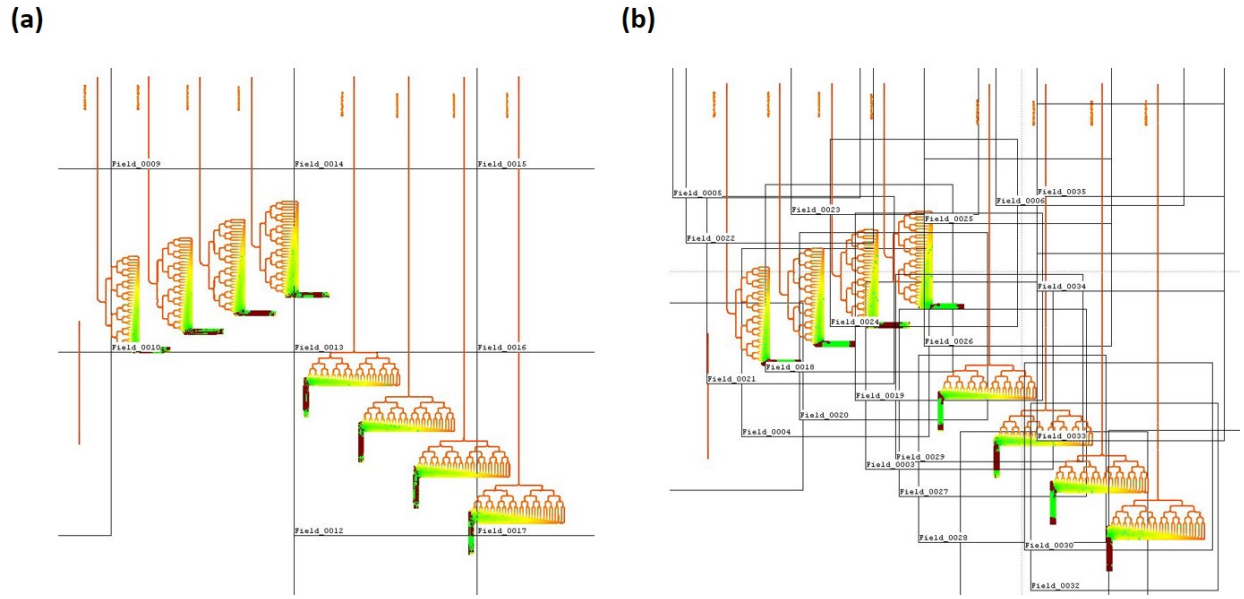

Figure 4.17. (a) Fracturing result of fixed writing order. (b) Fracturing result of overlapped follow geometric writing order.

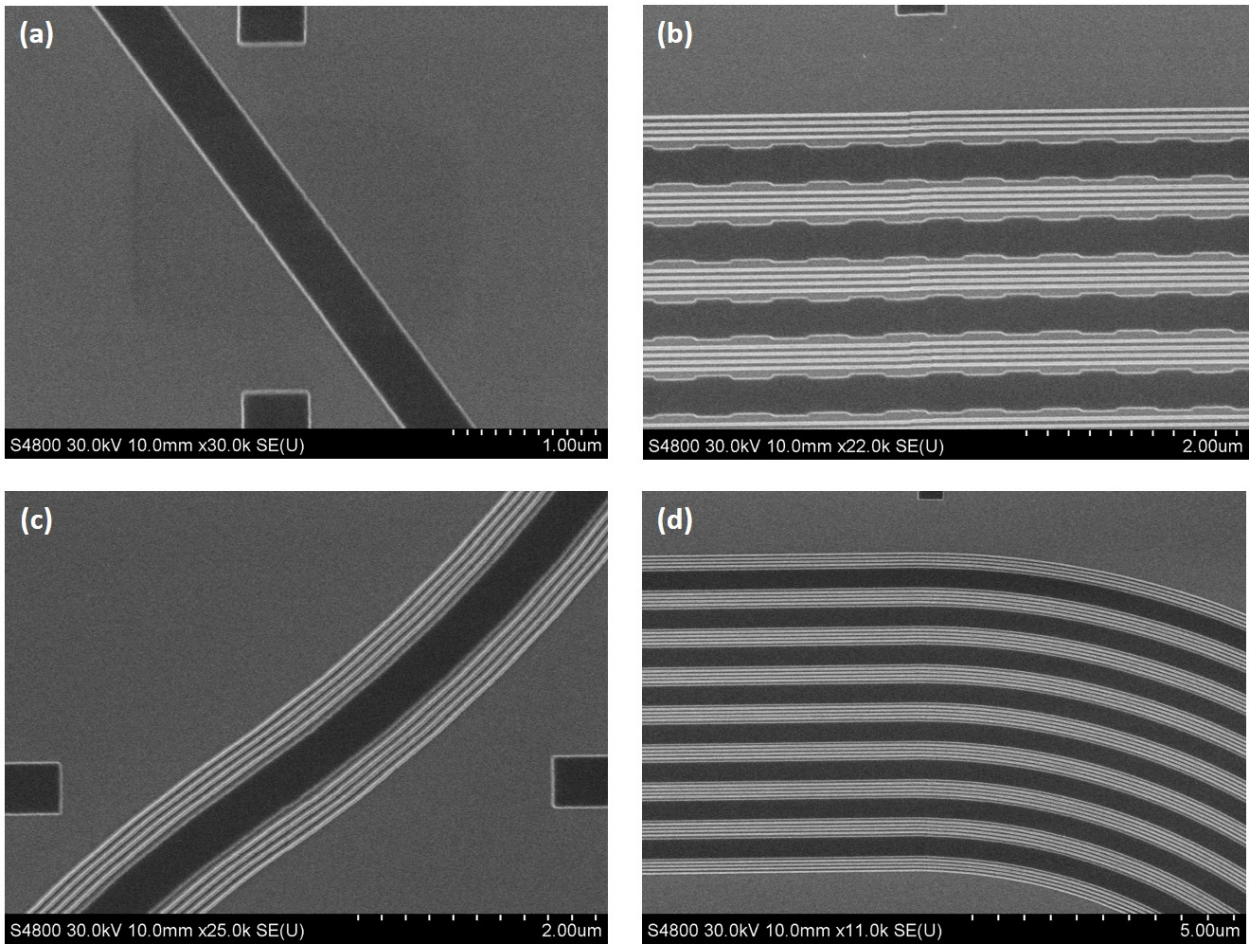

Figure 4.18. SEM images of final optimizations of both dose distribution and stitching error resolution at the field boundary regions.

5. EXPERIMENTAL RESULTS AND DISCUSSIONS

5.1 High power optical transmission with hybrid waveguide structure

First, we must evaluate the performance of the coupler design. The layout of the fabricated device is shown in Figure 5.1 (a); it contains several reference waveguides of silicon, silicon nitride, and the additional half-circled curves on each straight waveguide's material. Those were tested with 1 mm of its length, including the inverse tapers on the input/output facets for both Si and Si_3N_4 waveguides, which were optimized for 2.5 μm of mode field diameters (MFD) of lensed fiber for 1550 nm wavelength. The bending radius of the Si waveguide was 18.2 μm and that of Si_3N_4 is 48.25 μm, both bending radii were large enough with the neglectable loss of fundamental TE mode guiding. Those results are presented in Figure 5.1 (b). The output from Si_3N_4 waveguides grew proportional to the input power while output from the Si waveguide grew linearly up to 5 mW and then began to drop with respect to the input power. The reason for the decreasing output at the Si waveguide was that the free carriers in Si absorbed the photon energy and switched it to thermal energy. Thus, once the input power increased, the absorption of photon energy heated the core waveguide and produced more free carriers, continuously leading to more absorption. Assuming an edge coupling loss of 3 dB on each side, we estimated the maximum power the Si waveguide could deliver to be approximately 10 mW. A similar transmittance result showed for the Si_3N_4 to Si hybrid coupled waveguide. It showed approximately 0.5 dB higher insertion loss than the straight Si waveguide and had a power handling capability of up to 10 mW.

Additionally, the layout of 1 x 8 tree-branch Si and Si_3N_4 hybrid structures with combining 1 x 2 MMI splitters were also fabricated, as shown in figure 5.2 (a). The result from this layout is shown in figure 5.2 (b) and (c). The output power from six Si waveguide ports showed uniform distribution within 1 dB of power variation. This means that if the Si_3N_4 to Si hybrid branches were expanded more than 1 x 16, then the total power guiding and distribution could be increased; thus, this is a promising structure for high-power guiding OPA-based LiDAR and waveguide-arrayed DLA structures.

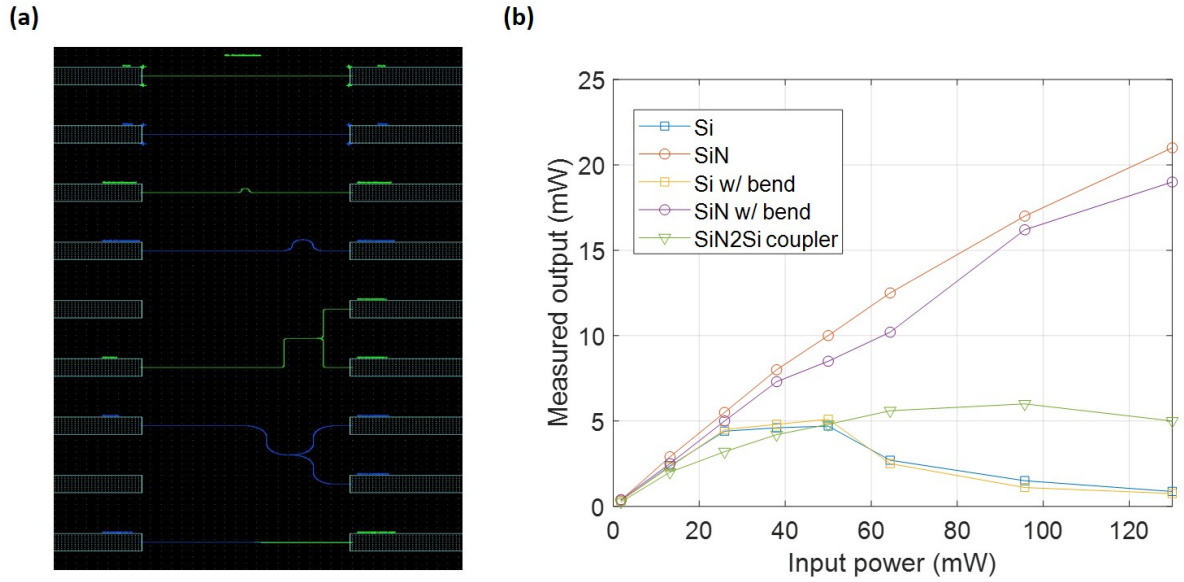

Figure 5.1. (a) The layout of optical power transmittance test for silicon nitride, silicon, and hybrid structured waveguides and (b) the results of power transmittance from the fabricated layout.

5.2 Demonstration of Half-wavelength pitched silicon nitride to silicon optical phased array

5.2.1 Results of 16-channel e-skid applied OPA

We demonstrated an OPA design with a 16-channel array of uniform half-wavelength spacing, large aliasing-free beam steering, and two-dimensional beam confinement [39]. Using the fabricated device of figure 3.1, we measured the range of the angle of aliasing-free beam steering. Figure 5.3 (a) is an image of the experimental setup of scanning the angle of the beam emission from the top surface of the device. Once the input tunable wavelength laser source was guided through the lensed fiber, it coupled it with the end-fire coupling method at the right-hand side of the image. To measure the correct scanning angle, we aligned the rotational stage at the same position as the device and then fixed a photodiode with a 5 mm input aperture to a rotational stage. The output beam was sampled by the photodiode through an attached adjustable iris. This setup covered a FoV from -80° to 60°, limited by the placement of input lensed fiber. As discussed in Chapter 3, by tuning the input wavelength from 1535 nm to 1575 nm, different linear phase profiles were applied

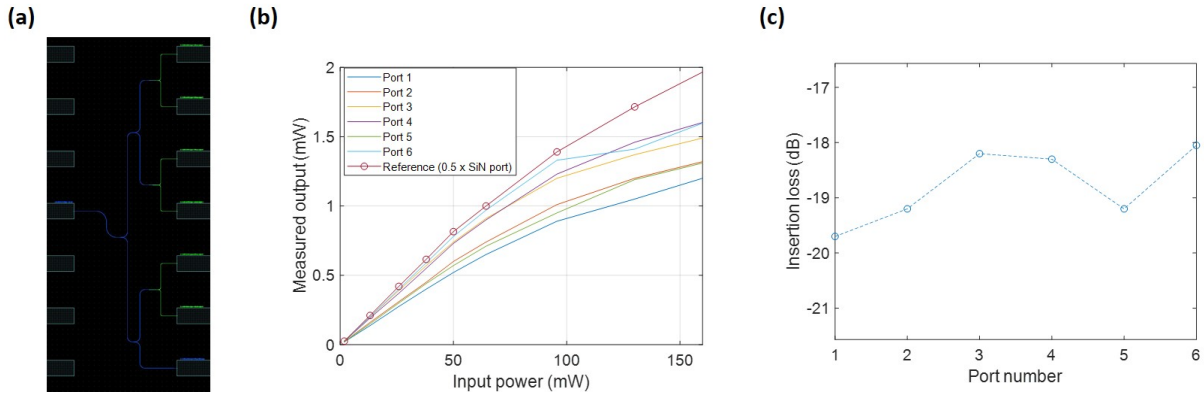

Figure 5.2. (a) The layout of 1 x 8 MMI splitting structures and hybrid couplers of silicon nitride to silicon and (b) testing results from the layout. The reference line is the measured output of the Si_3N_4 waveguide for comparing Si transmittance

to the grating emitters due to the L-shaped delay lines and steered the beam in different directions. Aliasing-free beam steering is observed within a 120° FoV (-67° to 53°). Figure 5.3 (b) presents the normalized angular emission pattern for different input wavelengths. The FWHM of the measured upright beam was 6°, which matched the estimation from the array size. Figure 5.3 (c) shows the agreement between the measured beam and expected beam positions due to the optical delay line tuned by the wavelength.

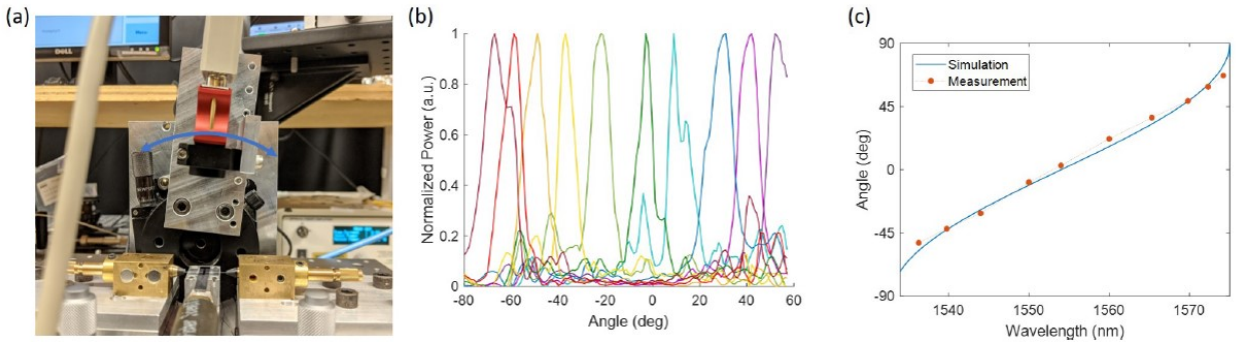

Figure 5.3. (a) Image of experimental setup of emission angle scanning. (b) Measurement result of the angled beam with different wavelength input. (c) Measured steering angle compared with simulation result from the optical delay line.

5.2.2 Results of 32-channel e-skid applied OPA

Previous 16-channel Si-only OPA-based LiDAR devices operated at a low input power (approximately 1 mW). For OPA designs in automobile applications, two major characteristics should be considered: emission power, which is directly related to detection distance, and FoV. Since the 32-channel Si_3N_4-to-Si hybrid device described in figure 3.3 achieved both high power emission and full range FoV, we adjusted the experimental setup from the previous one to measure the main beam with both high power and almost a full range of angles. As shown in figure 5.4, we switched the photodetector that could detect the power up to 1 W with the wavelength range of 1200 to 2500 nm. We also rotated 90-degrees of the direction of angle steering from the previous setup (also rotated emission gratings) to avoid the interference of the input fiber holder, so that the power value could be recorded as over 155° (from -65° to 90° off axis) with 1-degree interval by the detector.

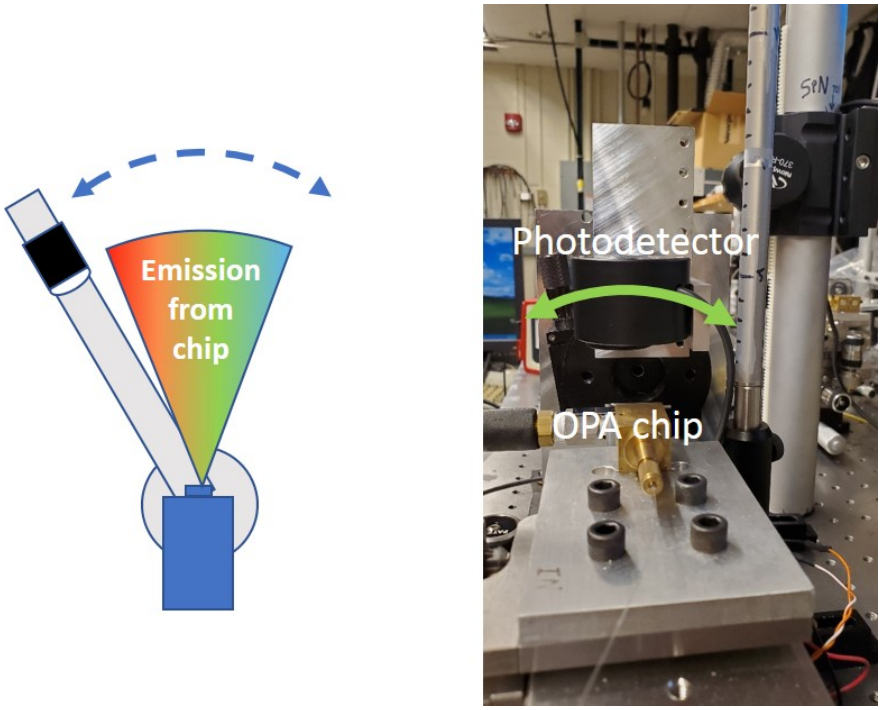

Figure 5.4. (a) Illustration of experimental setup and (b) the image of actual setup.

The measurement results are shown in Figure 5.5 (a) and (b). We tested 32-channel L-shaped OPA devices with both Si-only (a) and Si_3N_4-to-Si hybrid (b) composited structures.

A device with 32 channel Si-only OPA with 775 nm emitter spacing demonstrated 135° aliasing-free beam steering FoV, and a device with 32 channel Si_3N_4-to-Si hybrid OPA with 775 nm emitter spacing achieved 70° of aliasing-free FoV, which is limited by the insufficient wavelength tuning from the Erbium-doped fiber amplifier (EDFA).

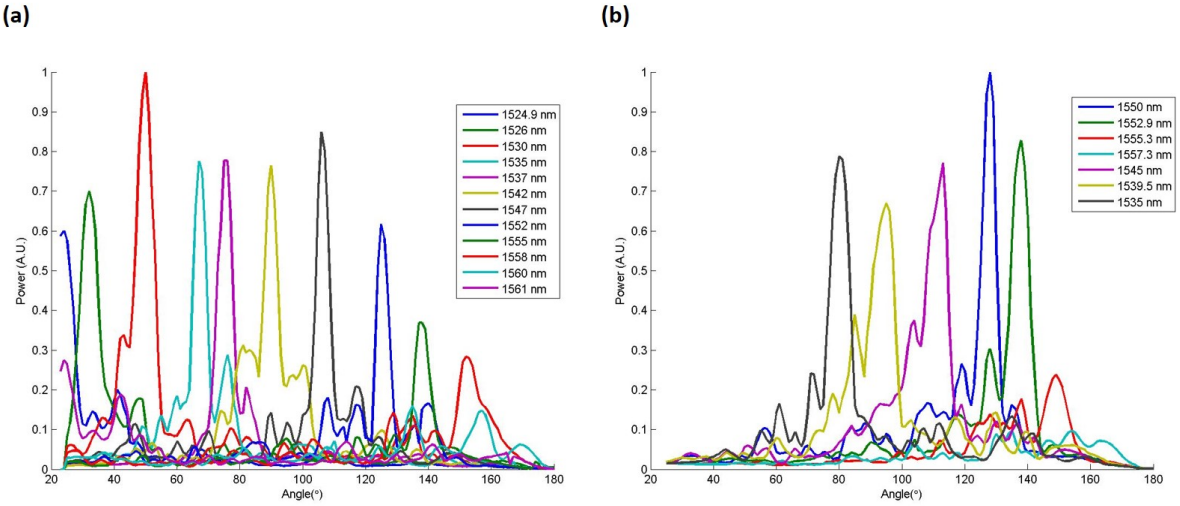

Figure 5.5. (a) Measurement result from 32 channel Si OPA; (b) Measurement result from 32 channel Si_3N_4-to-Si hybrid OPA

Furthermore, we scanned two different rotational angles from the emitted beam so that we could obtain a 2D profile of the beam. To investigate the 2D profile of the beam, we first needed to set the beam that emits perpendicular to the surface of the grating emitters. Figure 5.5 (b) shows that the wavelength of the perpendicular emission from the top of the device was at 1540 nm. Thus, we set the wavelength at 1540 nm and inserted the input optical power to 32 channels of Si_3N_4-to-Si hybrid OPA, and then scanned two different rotational angle. The results are shown in Figure 5.6. Figure 5.6 (a) shows the angle annotation concerning the grating emitter. θ - angle represents the beam profile along with the direction of the grating-structured waveguide array so that its width and direction were followed by the phase control of each waveguide array. However, ϕ - angle describes the beam profile along with the sub-wavelength grating teethes; it was controlled by the wavelength tuning. Figure 5.6 (b) and (c) present the emission results at 1540 nm of input wavelength. The results show different values for FWHM for each angle of the beam. Since the area

of the emitter grating was different (approximately 24 μm of array width and 140 μm of grating length), the FWHM of each angle was also different. We had the emitted beam approximately 8.8° of FWHM of θ - angle and 1.5° of FWHM of ϕ - angle profile. These values are related with the length of grating emitters with respect to the angle components.

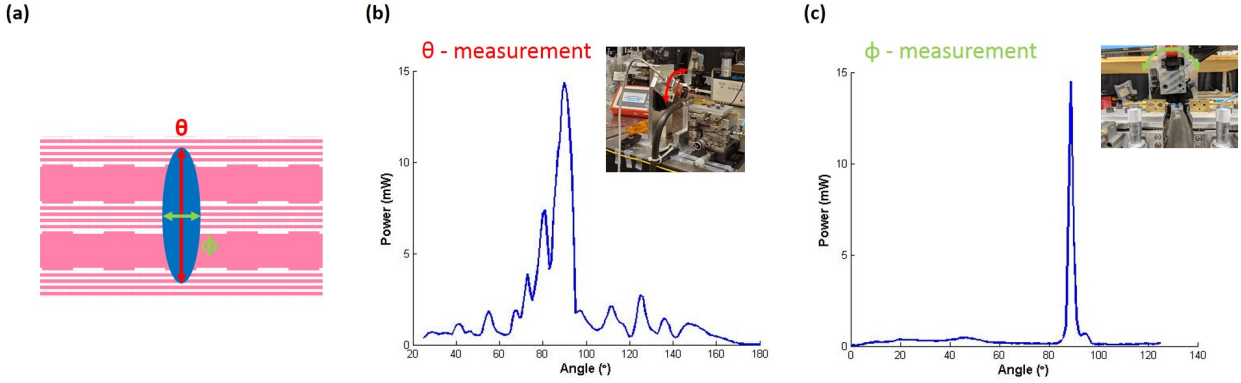

Figure 5.6. (a) Illustration of denoted angle components of the emitted beam with respect to the direction of grating array. (b) Emission result of θ-angle at the wavelength of 1540 nm. (c) Emission result of ϕ-angle at the wavelength of 1540 nm.

Since the size of the input aperture of the photodetector was fixed at 5 mm and the distance between the OPA device and the detector was also fixed at 5 cm while measuring the beam by rotating the rotational stage, the measured data is the convolution between the actual emission profile and a gate function from the measured data. Thus, we de-convolved the detector gate function from the measured data and achieved an emission profile of θ - angle with 0.1° precision. The resulting data are shown in figure 5.7. Figure 5.7 (a) and (c) are more precise results from the de-convolution process of figure 5.5 (a) and (b). Figure 5.7 (b) and (d) are the collected points of normalized beam widths of θ - angle from the figure 5.7 (a) and (c). The expected beam width from the OPA emission was calculated to the equation 2.4. We normalized the beam width at different emission angle by factoring out the term $1/cos\theta$. The normalized beam width is 3.56° for Si-only OPA and 3.89° for Si_3N_4-to-Si hybrid OPA, compared to the expected value of 3.17°. The phase error between the emitter array contributes the difference between Si-only and Si_3N_4-to-Si hybrid OPA, and also between the experimental values the calculated one.

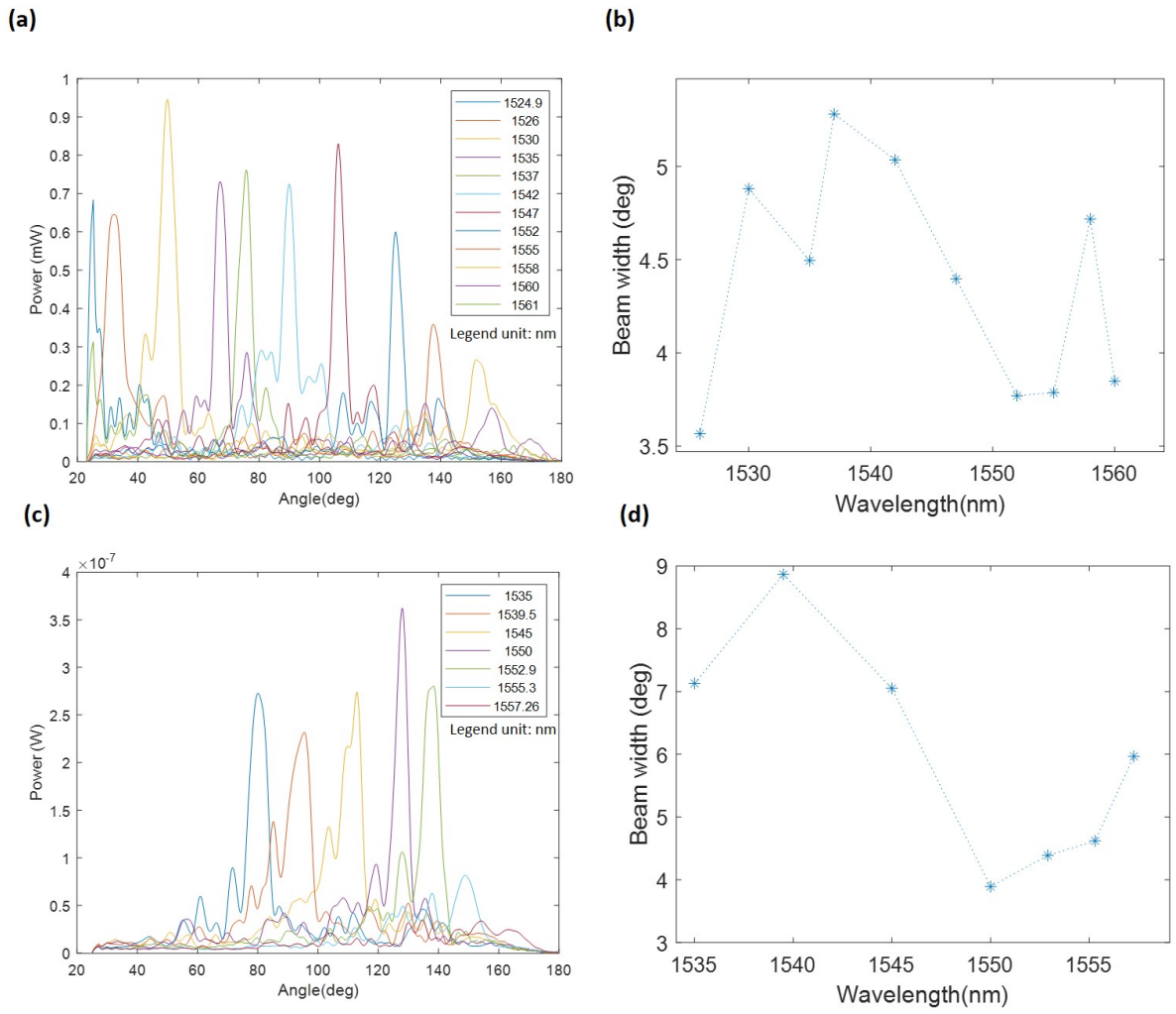

Figure 5.7. (a) Deconvolved result from the measurement result of 32 channel Si OPA. (b) Normalized beam width from 32 channel Si OPA. (c) Deconvolved result from the measurement result of 32 channel Si_3N_4-to-Si hybrid OPA. (d) Normalized beam width from 32 channel Si_3N_4-to-Si hybrid OPA.

To analyze the power handling capability difference between Si-only and Si_3N_4-to-Si hybrid OPA devices, we first tested Si-only OPA with inserting amplified power from EDFA. Figure 5.8 shows the emission power concerning the input power at the fixed wavelength of 1547 nm. The emission power increased while the input power also increased up to 400 mW. However, the emission power suddenly dropped at the input power of 500 mW, approximately a quarter of the power emission from 400 mW. This can be explained by previous waveguide power handling tests. As the high input power produces more free carriers inside the main

silicon waveguide branch, these carriers turned into thermal energy and lowered the optical output power.

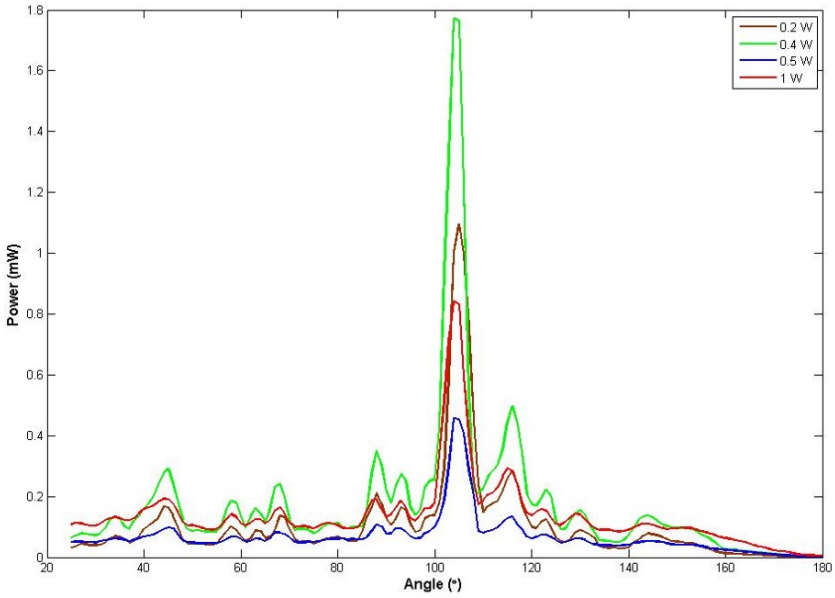

Figure 5.8. Result of emission power from 32 channel Si-only OPA at 1547 nm of input wavelength with the input power of: 0.2 W, 0.4 W, 0.5 W, and 1 W.

However, for Si_3N_4-to-Si hybrid OPA devices, it was difficult to see such nonlinear effects of emission power due to the main branch of the input waveguide consisting of Si_3N_4, which has much lower nonlinearity than silicon. To measure the maximum emission power from the device, we set the 1550 nm of input wavelength and inserted the three different power levels from EDFA: 0.5 W, 1 W, and 1.6 W. Both the measured and de-convolved data are shown in figure 5.9 (a) and (b). The total beam power is shown in figure 5.9 (c), which gives a maximum emission power of 44.38 mW at 1.6 W input and shows a strong linear relationship between input and output power profiles. This value is the highest amount of CW power measured from a Si OPA emitter array. It should also be noted that the effect of the strong vibration of the fiber while coupling the high input power into the chip affected the maximum amount of power coupled into the chip. Additionally, with little nonlinearity observed during the measurement, a higher emission power could be achieved from this

design. The total emission efficiency was approximately 10 %, while the power within the main beam was approximately 3 % of the input power, which is compatible with the reported value from the recent article [56].

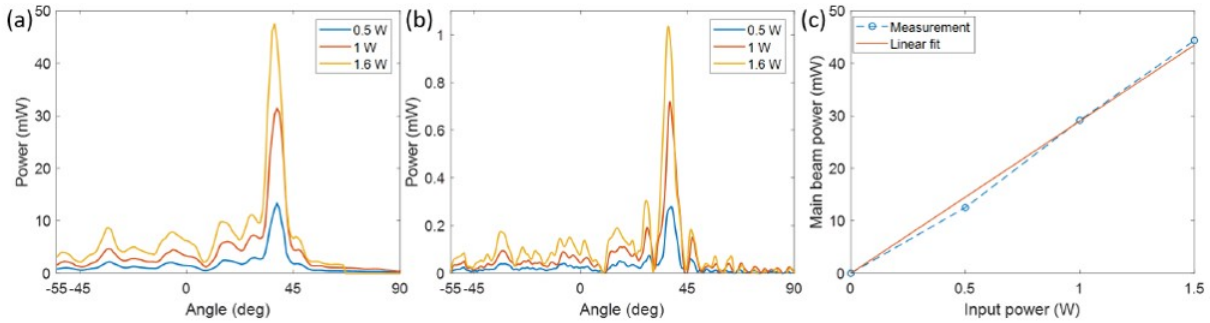

Figure 5.9. (a) High power emission measurement from 32 channel Si_3N_4-to-Si hybrid OPA; (b) Deconvolved result from (a); (c) Emitted main beam power with respect to input power.

Furthermore, FDTD simulations were performed to observe the effect of phase error on the current device. In the simulation, the input amplitude and phase of 32 emitters were optimized to reconstruct the de-convoluted emission profile (see Figure 5.9 (b)). The reconstructed profile for matching its beam is shown in figure 5.10 (a). Once phase errors from all 32 channels of the array were suppressed, we could achieve up to 2.5 times higher power from the measured data, as shown in Figure 5.10 (b). This means, if we could actively control the phase on each of the branches individually, a higher beam power could be achieved. Figure 5.10 (c) illustrates the simulation result of the power of the main beam with respect to the pitch of the OPA array. It shows that if the emitter spacing extends from $\lambda/2$ to λwhile keeping the same errors of phase and power, the power of the main beam drastically dropped to 50 % from the measured data due to the generations of grating lobes.

5.3 Estimations of waveguide-arrayed hybrid DLA structure

In Chapter 3, we proposed several designs of waveguide-arrayed Si_3N_4-to-Si hybrid DLA in figure 3.5, figure 3.6, and figure 3.7 for different initial velocity of electrons.To accelerate the electrons traveling through the electron channels surrounded by the waveguide arrayed

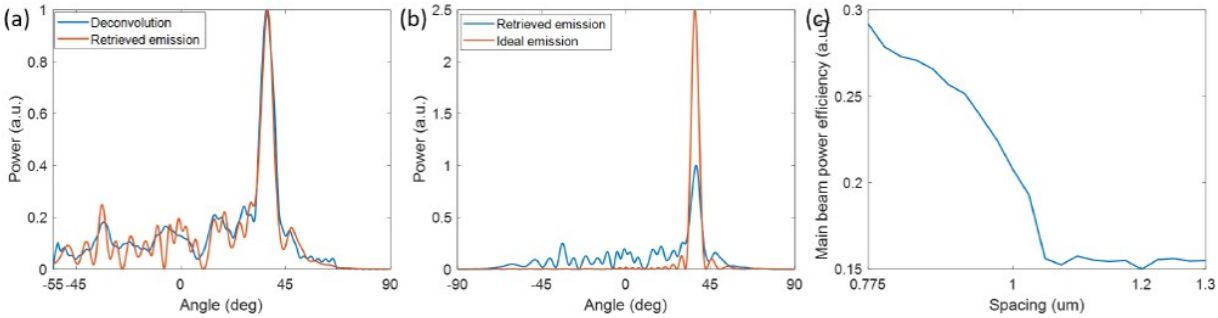

Figure 5.10. (a) Comparison between measured and simulation retrieved emission profile. (b) Comparison between retrieved and ideal emission profile. (c) Main beam power efficiency with respect to OPA emitter spacing.

branches, the phases of the electric field emitted from each waveguide array should synchronize the trajectories of electrons. Then, the pitch of the array should match the condition of $\Lambda = \beta\lambda_0$, where β refers to the ratio of electron velocity to the speed of the light and λ_0 as the central wavelength of the free-space pulsed laser. For satisfy these conditions when $\beta = 0.43$, which is a condition of initial electron energy of 57 keV for shoebox-sized designed accelerator structure, we must place the array with the 670 nm of its pitch for the operational central wavelength at 1550 nm. Figure 5.11 shows how the acceleration mode and phases were generated to accelerate the electrons. Once the electron traveled through the channel as in Figure 5.11 (a) and the optical power, which had a sub-picosecond pulsed laser with 1550 nm of the central wavelength, synchronously emitted the same phase with each output port simultaneously, then if one of the electrons synchronously confronted the maximum phase of quasi-TE_0 mode at the output port, it would keep following the positive phase while traveling through the channel and keep avoiding the maximum point of negative phase at the half of optical cycles, as in Figure 5.11 (b) and (c). Therefore, the electron has a net energy gain while synchronizing these steps. Figure 5.11 (b) illustrates the top-side view of electron channel, and Figure 5.11 (c) presents the cross-sectional view of the mode of generation inside the middle of the channel.

To shape the mode and propagate the power thoroughly inside the electron channel, we must place the same cross-sectional size of the arrayed waveguide on the other side of the electron channels, aligning the same position so that the guided and propagated modes from

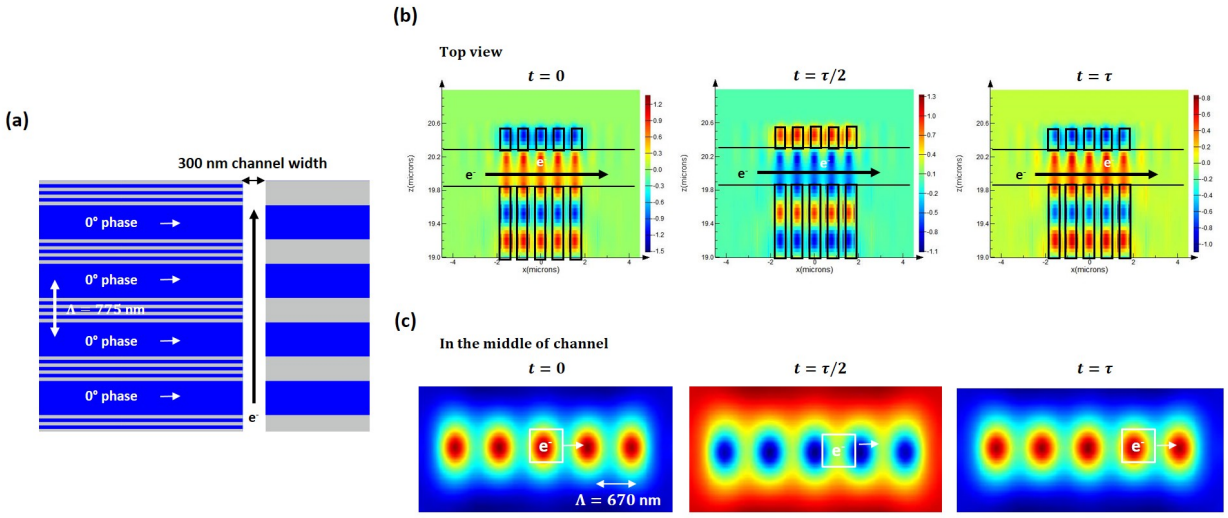

Figure 5.11. (a) Illustration of generating acceleration modes in the channel of the electron beam trajectory from the in-phase waveguide array. (b) Top-view illustration of mode profile generated from the waveguide arrayed structure while the electron trajectory synchronizes with the mode. (c) Cross-sectional illustration of the mode while the electron travels into the channel.

the left-hand side (at the aspect of the structural image) can be coupled with the waveguide on the right-hand side without any phase distortion. Additionally, once the reflector is placed at the end of the waveguide array on the right-hand side, the phases of the mode inside the electron channel can be amplified. The gold film has the value of LIDT at the femtosecond pulsed laser with NIR approximately 0.2 J/cm^2, which is slightly higher than that of silicon; thus, it is compatible with using the reflector at the end of the waveguide array at the end of the other side. However, determinations of the sizes of the electron channel and the length of the waveguide array on the other side are critical for synchronizing the right acceleration mode inside the channel. This necessitates calculating both the ratio of the internal reflection from the guided waveguide array and the reflection from the reflectors on the other side. Figure 5.12 (a) and (b) illustrate the placements of aligned short waveguide arrays (k-mismatched waveguide array and e-skid applied waveguide array, respectively) and the gold reflectors. We used 3D-FDTD simulators to calculate the acceleration modes with respect to the size of electron channels and the locations of the gold reflectors. Figure 5.12 (c) presents the results of the intensities of the acceleration mode (E_z) and the deflection

mode (E_x). The simulation result driven by sweeping the size of the gap of the electron channel shows that the highest ratio from the acceleration mode to the deflection mode is when the size of the gap is at 300 nm. Figure 5.12 (d) provides the result of the placement of the gold film, beginning from the 300 nm of a gap from the left-hand side. This result shows that the highest ratio from the acceleration mode to the deflection mode is at 450 nm of the length of the waveguide array from the gap to the reflector. Thus, using the 3D-FDTD simulation result with the fixed conditions outlined above, the intensity of the acceleration mode achieved the highest value and the deflection mode the lowest, as shown in Figure 5.12 (e) and (f), which the intensities of acceleration and deflection modes observed from the top-side of the structure.

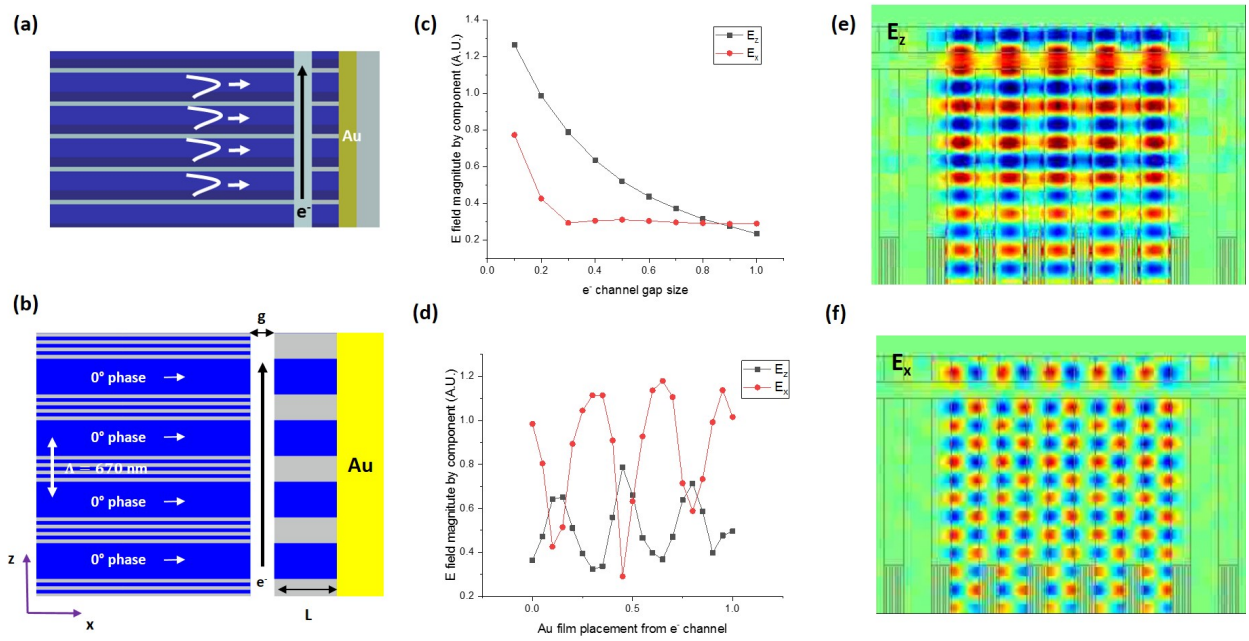

Figure 5.12. (a) 3D illustration of k-mismatched waveguide array with Au-reflector. (b) 2D illustration of e-skid arrayed waveguide with Au-reflector. (c) Electric field intensities of acceleration mode (E_z) and deflection mode (E_x) difference due to the variation of the channel gap. (d) Electric field intensities of acceleration mode (E_z) and deflection mode (E_x) difference due to the variation of the placement of Au-reflector from the electron channel gap. (e) Generation of acceleration mode by optimized channel gap and Au-reflector. (f) Generation of deflection mode by optimized channel gap and Au-reflector.

Based on the simulation results in Figure 5.12, we can calculate the net gain while the electron travels through the designed electron channel with the initial velocity of $\beta = 0.43$ (which corresponds to the initial electron energy of 57 keV). Figure 5.13 (a) illustrates the intensity of the mode oscillated by the time span inside the cross-sectional channels with 670 nm of the arrayed pitch. The white arrow presents the trajectory of the electron concerning the time spent in a phase-synchronous condition. In this condition, the electron achieves a higher energy gain (which corresponds to the higher net acceleration) than the negative gain from the evanescent modal field in between the adjacent waveguides while traveling into each pitch of array, as in Figure 5.13 (b). The net gain can be achieved approximately 185 % from the intensity of electric field from the single output from the silicon waveguide.

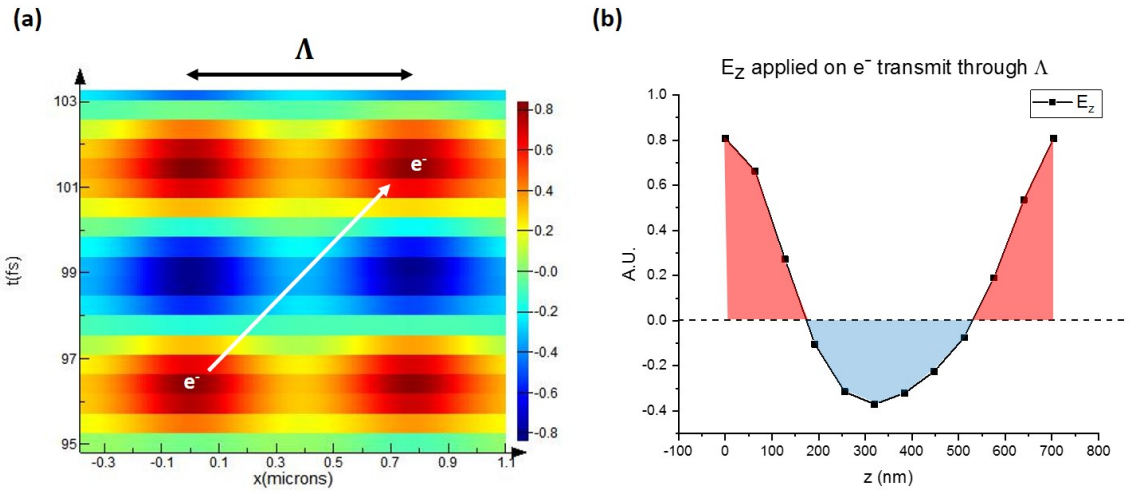

Figure 5.13. (a) Illustration of an electron trajectory while acceleration mode generated in the pitch size of Λ with respect to the time. (b) A plot of net gain of the electron while it travels in Λ.

From these simulation results, we can estimate the energy gain and the acceleration gradient from the device of Figure 3.7 (a). Previously, we had tested the transmittance of guiding the high-power pulsed laser with both silicon and Si_3N_4 waveguides with the condition of the high confinement mode. The characteristics of the laser was 250 fs of the pulsed width and 1550 nm of the central wavelength and a repetition rate of 100 kHz. With the cross-sectional size of silicon waveguide with 450 nm (W) x 220 nm (H), the maximum output energy was 3 pJ. Hence, the peak power intensity guided by silicon can be calculated,

and its value is about 1.2×10^{14} W/m^2. This value corresponds to the maximum intensity of the electric field of single mode, which is 192 MV/m. In figure 3.7 (a) 8-branches of each Si_3N_4 waveguide from the grating coupler has 32 channels of silicon waveguide array. Since we knew that the power transmittance of Si_3N_4 waveguide is much higher from previous demonstration [24], we considered that each silicon branch can transfer the electric field intensity up to 34.29 MV/m. With calculating the net gain value from the Figure 5.13 (b), then we can get the acceleration gradient of 61.73 MV/m of the structure and 10.28 keV of energy gain within the 267 μm of interaction length. Table 5.1 summarized the results of previous DLA experiments in sub-relativistic regime. The table shows this design can

Table 5.1. Summary of previously demonstrated DLA results in sub-relativistic regime. $\mathcal{E}_0$ refers to the initial electron energy before injecting into the DLA structures, G refers to the acceleration gradient, $\Delta\mathcal{E}$ refers to the energy again, and L refers to the interaction length.

Year	Citation	$\mathcal{E}_0$ [keV]	G [MeV/m]	$\Delta\mathcal{E}$ [keV]	L [μm]
2013	[7]	27.7	25	0.3	11.2
2015	[9]	86.5 - 96.3	370	1.05 - 1.95	5.6
2015	[8]	96.3	218	1.22	5.6
2018	[10]	99	200	3	15
2019	[57]	57	60	1.3	50.76
2020	[3]	97	178	2.67	15
2020	[12]	83.4	30.5	0.915	30
This device		57	61.73	10.28	267

produce the highest acceleration gradient among the devices that have an initial electron energy at 57 keV. In addition, due to the fact that the tree-branch network design is able to extend the interaction length with keeping small pitch array, this device can generate the highest acceleration gradient among the longest interaction length in the sub-relativistic regime. Furthermore, since the design consists with Si_3N_4 to Si hybrid waveguide array, it has also higher acceleration gradient and energy gain than the silicon-only inverse design structure from Dr. Neil Sapra's previous demonstrations [12].

6. SUMMARY AND CONCLUSION

In summary, we have shown the new layouts, fabrication technologies, and its experimental measurements of the silicon nitride to silicon hybrid structures of OPA-based LiDAR and waveguide arrayed DLAs. Since both applications of on-chip waveguides integrated circuits shared similar characteristics, such as high power durability, phase coherences, and minimizing the crosstalk while guiding the signals into the half-wavelength pitch waveguide arrays, we designed both applications with similar waveguide arrayed structures.

In chapter 2, we studied the theoretical reviews of basic operational mechanisms of both optical phased arrays and dielectric laser accelerators. Also, we studied the physical mechanisms of laser-induced damage thresholds of dielectric materials at the high-power laser which has a sub-picosecond pulse width and a near-IR wavelength range. We presented data of five representative optical materials (Si, SiO_2, Si_3N_4, Al_2O_3, and $LiNbO_3$) which are widely utilized in photonic integrated circuits. In addition, we reviewed the laser-induced damage threshold and power handling capabilities of Si_3N_4 waveguides at the weakly guided mode. Furthermore, we studied two methods of extremely reducing the crosstalk of signal in sub-wavelength pitch waveguide array, which are extreme skin-depth (e-skid) waveguide structures and phase space mismatched (k-mismatched) waveguide structures. We reviewed those waveguide structures by explaining the demonstrated results from the articles that were recently published including our last experimental demonstrations.

In chapter 3, we proposed various types of designs of OPA-based LiDAR devices and waveguide arrayed DLA devices with applying Si_3N_4 to Si hybrid structures. Then, we explained the design of each component that consisted of each full-layout by describing how we optimized each component driven by 3D-FDTD simulations, such as half-wavelength pitch arrays of e-skid and k-mismatched, Si_3N_4 to Si hybrid mode converters, 1x2 multimode interferometer (MMI) beam splitters for both SOI and Si_3N_4 platforms, and apodized Si_3N_4 grating couplers and its power splitters.

In chapter 4, we overviewed the fabrication process flow of Si_3N_4 to Si hybrid waveguide arrays that are commonly used in both applications. Then we discussed the fabrication challenges and resolution methods, such as trapping the void gap in between the metama-

terial fin structures of e-skid array, applying the customized proximity effect corrections for avoiding pattern distortions in large and dense arrays while writing e-beam lithography, and applying customized fracturing methods of patterns for alleviating stitching error issues.

In chapter 5, we showed the experimental demonstrations from the fabricated devices and analyzed the results. We first presented the power transmittance results of Si_3N_4 to Si hybrid mode converting devices and 1x2 MMI splitting results. We demonstrated the optimized designs shown in chpater 3 which produced power transmittance with low loss and distributed power uniformly at high power input conditions. In addition, we tested the passive beam steering of the 16 channels Si-only OPA device. We first achieved top emission of 120° of aliasing-free beam steering while tuning the wavelength at the c-band. Furthermore, we tested the 32 channels of both Si-only and Si_3N_4 to Si hybrid OPA structures to measure both steerable angles and to compare their maximum power emission. A deconvolution process from the retrieved power profile was performed to discover the original emission profiles and the power within the main beam. We measured a 135° of field-of-view along with a high power emission (44 mW), which indicates the Si_3N_4 to Si hybrid OPA structure is a promising design for long-range LiDAR system. In addition, we estimated the net gain and its acceleration gradients from the hybrid waveguide arrayed DLA structures. From the newly proposed design, we would achieve 61.73 MV/m of its acceleration gradient and 1.28 keV of energy gain within 21 μm of interaction length while the initial electron energy is at 57 keV. This design indicates higher value than the Si-only inverse designed DLA structures and it first demonstrates that waveguide arrayed DLA is operatable in low initial electron energy.

For the future work, we need to run the experimental demonstrations of waveguide arrayed DLA structures. In addition, we need to increase the number of arrays of hybrid OPA devices so that we achieve the main beam with higher power and reducing the beam width for stepping forward to the productions of the commercial compatible. Also, we need to investigate active tuning structures on both applications with integrating active phase shifters on the chips for increasing the signal to noise ratio and higher phase coherence.

REFERENCES

[1] C.-P. Hsu, B. Li, B. Solano-Rivas, A. R. Gohil, P. H. Chan, A. D. Moore, and V. Donzella, "A review and perspective on optical phased array for automotive lidar," *IEEE Journal of Selected Topics in Quantum Electronics*, vol. 27, no. 1, pp. 1–16, 2021. DOI: 10.1109/JSTQE.2020.3022948.

[2] X. Sun, L. Zhang, Q. Zhang, and W. Zhang, "Si Photonics for Practical LiDAR Solutions," *Applied Sciences 2019, Vol. 9, Page 4225*, vol. 9, no. 20, p. 4225, Oct. 2019. DOI: 10.3390/APP9204225. [Online]. Available: https://www.mdpi.com/2076-3417/9/20/4225/htm%20https://www.mdpi.com/2076-3417/9/20/4225.

[3] Y. Miao, "Design and fabrication improvements for the dielectric laser accelerators.," PhD thesis, 2020. DOI: http://purl.stanford.edu/hk823qg0346.

[4] Z. Zhao, "Photonic design of dielectric laser accelerators and quantum features of free electrons," PhD thesis, 2021. DOI: http://purl.stanford.edu/bx457cv7250.

[5] T. Plettner, P. P. Lu, and R. L. Byer, "Proposed few-optical cycle laser-driven particle accelerator structure," *Physical Review Special Topics - Accelerators and Beams*, vol. 9, p. 111 301, 11 Nov. 2006. DOI: 10.1103/PhysRevSTAB.9.111301. [Online]. Available: https://journals.aps.org/prab/abstract/10.1103/PhysRevSTAB.9.111301.

[6] P. EA, S. K, E. RJ, C. ER, W. Z, M. B, M. C, M. J, L. KJ, W. D, S. EB, C. B, S. B, T. G, and B. RL, "Demonstration of electron acceleration in a laser-driven dielectric microstructure," *Nature*, vol. 503, pp. 91–94, 7474 2013, ISSN: 1476-4687. DOI: 10.1038/NATURE12664. [Online]. Available: https://pubmed.ncbi.nlm.nih.gov/24077116/.

[7] J. Breuer and P. Hommelhoff, "Laser-based acceleration of nonrelativistic electrons at a dielectric structure," *Physical Review Letters*, vol. 111, p. 134 803, 13 Sep. 2013. DOI: 10.1103/PhysRevLett.111.134803. [Online]. Available: https://journals.aps.org/prl/abstract/10.1103/PhysRevLett.111.134803.

[8] K. J. Leedle, R. L. B. R. Fabian Pease, and J. S. Harris, "Laser acceleration and deflection of 96.3 kev electrons with a silicon dielectric structure," *Optica, Vol. 2, Issue 2, pp. 158-161*, vol. 2, pp. 158–161, 2 Feb. 2015, ISSN: 2334-2536. DOI: 10.1364/OPTICA.2.000158. [Online]. Available: https://www.osapublishing.org/viewmedia.cfm?uri=optica-2-2-158&seq=0&html=true%20https://www.osapublishing.org/abstract.cfm?uri=optica-2-2-158%20https://www.osapublishing.org/optica/abstract.cfm?uri=optica-2-2-158.

[9] K. J. Leedle, A. Ceballos, H. Deng, J. S. Harris, O. Solgaard, R. F. Pease, and R. L. Byer, "Dielectric laser acceleration of sub-100 kev electrons with silicon dual-pillar grating structures," *Optics Letters, Vol. 40, Issue 18, pp. 4344-4347*, vol. 40, pp. 4344–4347, 18 Sep. 2015, ISSN: 1539-4794. DOI: 10.1364/OL.40.004344. [Online]. Available: https://www.osapublishing.org/viewmedia.cfm?uri=ol-40-18-4344&seq=0&html=true%20https://www.osapublishing.org/abstract.cfm?uri=ol-40-18-4344%20https://www.osapublishing.org/ol/abstract.cfm?uri=ol-40-18-4344.

[10] K. J. Leedle, D. S. Black, Y. Miao, K. E. Urbanek, A. Ceballos, H. Deng, J. S. Harris, O. Solgaard, and R. L. Byer, "Phase-dependent laser acceleration of electrons with symmetrically driven silicon dual pillar gratings," *Optics Letters, Vol. 43, Issue 9, pp. 2181-2184*, vol. 43, pp. 2181–2184, 9 May 2018, ISSN: 1539-4794. DOI: 10.1364/OL.43.002181. [Online]. Available: https://www.osapublishing.org/viewmedia.cfm?uri=ol-43-9-2181&seq=0&html=true%20https://www.osapublishing.org/abstract.cfm?uri=ol-43-9-2181%20https://www.osapublishing.org/ol/abstract.cfm?uri=ol-43-9-2181.

[11] T. W. Hughes, S. Tan, Z. Zhao, N. V. Sapra, K. J. Leedle, H. Deng, Y. Miao, D. S. Black, O. Solgaard, J. S. Harris, J. Vuckovic, R. L. Byer, S. Fan, R. J. England, Y. J. Lee, and M. Qi, "On-chip laser-power delivery system for dielectric laser accelerators," *Physical Review Applied*, vol. 9, p. 054 017, 5 May 2018, ISSN: 23317019. DOI: 10.1103/PhysRevApplied.9.054017. [Online]. Available: https://link.aps.org/doi/10.1103/PhysRevApplied.9.054017.

[12] N. V. Sapra, K. Y. Yang, D. Vercruysse, K. J. Leedle, D. S. Black, R. J. England, L. Su, R. Trivedi, Y. Miao, O. Solgaard, R. L. Byer, and J. Vučković, "On-chip integrated laser-driven particle accelerator," *Science*, vol. 367, pp. 79–83, 6473 Jan. 2020. DOI: 10.1126/SCIENCE.AAY5734. [Online]. Available: https://www.science.org.

[13] A. Yaacobi, "Integrated optical phased arrays for lidar applications," Massachusetts Institute of Technology, Jun. 2015.

[14] S. Chung, H. Abediasl, and H. Hashemi, "A Monolithically Integrated Large-Scale Optical Phased Array in Silicon-on-Insulator CMOS," *IEEE Journal of Solid-State Circuits*, vol. 53, no. 1, pp. 275–296, Jan. 2018, ISSN: 00189200. DOI: 10.1109/JSSC.2017.2757009.

[15] J. K. Doylend, M. J. R. Heck, J. T. Bovington, J. D. Peters, L. A. Coldren, and J. E. Bowers, "Two-dimensional free-space beam steering with an optical phased array on silicon-on-insulator," *Optics Express*, vol. 19, no. 22, p. 21 595, Oct. 2011, ISSN: 1094-4087. DOI: 10.1364/oe.19.021595.

[16] N. V. Sapra, "Design and demonstration of on-chip integrated laser-driven particle accelerators," English, Copyright - Database copyright ProQuest LLC; ProQuest does not claim copyright in the individual underlying works; Last updated - 2021-09-28, PhD thesis, 2020, p. 113, ISBN: 9798662511361. [Online]. Available: https://www.proquest.com/dissertations-theses/design-demonstration-on-chip-integrated-laser/docview/2432569284/se-2?accountid=13360.

[17] Y. J. Lee, "Ultrafast laser-induced damage threshold of the optical materials in near-infrared region," Purdue University, 2017, p. 64, ISBN: 9780355613025. [Online]. Available: https://search.proquest.com/docview/2016700427?accountid=13360.

[18] *1. Laser-Induced Damage - LIDARIS*. [Online]. Available: http://lidaris.com/glossary-2/laser-induced-damage/.

[19] B. Rethfeld, D. S. Ivanov, M. E. Garcia, and S. I. Anisimov, "Modelling ultrafast laser ablation," *Journal of Physics D: Applied Physics*, vol. 50, no. 19, p. 193 001, 2017, ISSN: 0022-3727. DOI: 10.1088/1361-6463/50/19/193001. [Online]. Available: http://stacks.iop.org/0022-3727/50/i=19/a=193001?key=crossref.018ba9a682d87e828aa07398bc0c13af.

[20] K. Soong, R. L. Byer, E. R. Colby, R. J. England, and E. A. Peralta, "Laser damage threshold measurements of optical materials for direct laser accelerators," *AIP Conference Proceedings*, vol. 1507, no. 2012, pp. 511–515, 2012, ISSN: 0094243X. DOI: 10.1063/1.4773749.

[21] S. C. Jones, P. Braunlich, and R. T. Casper, "Recent progress progress on on laser-induced laser- induced modifications modifications and and intrinsic intrinsic bulk damage damage of of wide-gap wide -gap optical optical materials," vol. 28, no. 10, 1989.

[22] C. B. Schaffer, A. Brodeur, and E. Mazur, "Laser-induced breakdown and damage in bulk transparent materials induced by tightly focused femtosecond laser pulses," *Measurement Science and Technology*, vol. 12, no. 11, pp. 1784–1794, 2001, ISSN: 0957-0233. DOI: 10.1088/0957-0233/12/11/305. [Online]. Available: http://stacks.iop.org/0957-0233/12/i=11/a=305?key=crossref.043421ca1734b562bf30f003ece30735.

[23] M. Mero, J. Liu, W. Rudolph, D. Ristau, and K. Starke, "Scaling laws of femtosecond laser pulse induced breakdown in oxide films," *Physical Review B*, vol. 71, no. 11, p. 115 109, 2005, ISSN: 1098-0121. DOI: 10.1103/PhysRevB.71.115109. [Online]. Available: https://link.aps.org/doi/10.1103/PhysRevB.71.115109.

[24] S. Tan, Z. Zhao, K. Urbanek, T. Hughes, Y. J. Lee, S. Fan, J. S. Harris, and R. L. Byer, "Silicon nitride waveguide as a power delivery component for on-chip dielectric laser accelerators," *Optics Letters*, vol. 44, no. 2, p. 335, Jan. 2019, ISSN: 0146-9592. DOI: 10.1364/OL.44.000335. [Online]. Available: https://www.osapublishing.org/abstract.cfm?URI=ol-44-2-335.

[25] S. Jahani, S. Kim, J. Atkinson, J. C. Wirth, F. Kalhor, A. A. Noman, W. D. Newman, P. Shekhar, K. Han, V. Van, R. G. DeCorby, L. Chrostowski, M. Qi, and Z. Jacob, "Controlling evanescent waves using silicon photonic all-dielectric metamaterials for dense integration," *Nature Communications 2018 9:1*, vol. 9, pp. 1–9, 1 May 2018, ISSN: 2041-1723. DOI: 10.1038/s41467-018-04276-8. [Online]. Available: https://www.nature.com/articles/s41467-018-04276-8.

[26] J. A. Dionne, L. A. Sweatlock, H. A. Atwater, and A. Polman, "Plasmon slot waveguides: Towards chip-scale propagation with subwavelength-scale localization," *Physical Review B*, vol. 73, p. 035 407, 3 Jan. 2006. DOI: 10.1103/PhysRevB.73.035407. [Online]. Available: https://journals.aps.org/prb/abstract/10.1103/PhysRevB.73.035407.

[27] R. F. Oulton, V. J. Sorger, D. A. Genov, D. F. P. Pile, and X. Zhang, "A hybrid plasmonic waveguide for subwavelength confinement and long-range propagation," *Nature Photonics 2008 2:8*, vol. 2, pp. 496–500, 8 Jul. 2008, ISSN: 1749-4893. DOI: 10.1038/nphoton.2008.131. [Online]. Available: https://www.nature.com/articles/nphoton.2008.131.

[28] D. K. Gramotnev and S. I. Bozhevolnyi, "Plasmonics beyond the diffraction limit," *Nature Photonics 2010 4:2*, vol. 4, pp. 83–91, 2 Jan. 2010, ISSN: 1749-4893. DOI: 10.1038/nphoton.2009.282. [Online]. Available: https://www.nature.com/articles/nphoton.2009.282.

[29] S. Kim and M. Qi, "Mode-evolution-based polarization rotation and coupling between silicon and hybrid plasmonic waveguides," *Scientific Reports 2015 5:1*, vol. 5, pp. 1–7, 1 Dec. 2015, ISSN: 2045-2322. DOI: 10.1038/srep18378. [Online]. Available: https://www.nature.com/articles/srep18378.

[30] S. Kim and M. Qi, "Polarization rotation and coupling between silicon waveguide and hybrid plasmonic waveguide," *Optics Express, Vol. 23, Issue 8, pp. 9968-9978*, vol. 23, pp. 9968–9978, 8 Apr. 2015, ISSN: 1094-4087. DOI: 10.1364/OE.23.009968. [Online]. Available: https://www.osapublishing.org/viewmedia.cfm?uri=oe-23-8-9968&seq=0&html=true%20https://www.osapublishing.org/abstract.cfm?uri=oe-23-8-9968%20https://www.osapublishing.org/oe/abstract.cfm?uri=oe-23-8-9968.

[31] S. Raza, N. Stenger, A. Pors, T. Holmgaard, S. Kadkhodazadeh, J. B. Wagner, K. Pedersen, M. Wubs, S. I. Bozhevolnyi, and N. A. Mortensen, "Extremely confined gap surface-plasmon modes excited by electrons," *Nature Communications 2014 5:1*, vol. 5, pp. 1–7, 1 Jun. 2014, ISSN: 2041-1723. DOI: 10.1038/ncomms5125. [Online]. Available: https://www.nature.com/articles/ncomms5125.

[32] N. Kinsey, M. Ferrera, A. Boltasseva, and V. M. Shalaev, "Examining nanophotonics for integrated hybrid systems: A review of plasmonic interconnects and modulators using traditional and alternative materials [invited]," *JOSA B, Vol. 32, Issue 1, pp. 121-142*, vol. 32, pp. 121–142, 1 Jan. 2015, ISSN: 1520-8540. DOI: 10.1364/JOSAB.32.000121. [Online]. Available: https://www.osapublishing.org/viewmedia.cfm?uri=josab-32-1-121&seq=0&html=true%20https://www.osapublishing.org/abstract.cfm?uri=josab-32-1-121%20https://www.osapublishing.org/josab/abstract.cfm?uri=josab-32-1-121.

[33] J. B. Khurgin, "How to deal with the loss in plasmonics and metamaterials," *Nature Nanotechnology 2015 10:1*, vol. 10, pp. 2–6, 1 Jan. 2015, ISSN: 1748-3395. DOI: 10.1038/nnano.2014.310. [Online]. Available: https://www.nature.com/articles/nnano.2014.310.

[34] J. B. Khurgin, "Replacing noble metals with alternative materials in plasmonics and metamaterials: How good an idea?" *Philosophical Transactions of the Royal Society A: Mathematical, Physical and Engineering Sciences*, vol. 375, 2090 Mar. 2017. DOI: 10.1098/RSTA.2016.0068. [Online]. Available: https://royalsocietypublishing.org/doi/abs/10.1098/rsta.2016.0068.

[35] M. B. Mia, S. Z. Ahmed, I. Ahmed, Y. J. Lee, M. Qi, and S. Kim, "Exceptional coupling in photonic anisotropic metamaterials for extremely low waveguide crosstalk," *Optica, Vol. 7, Issue 8, pp. 881-887*, vol. 7, pp. 881–887, 8 Aug. 2020, ISSN: 2334-2536. DOI: 10.1364/OPTICA.394987. [Online]. Available: https://www.osapublishing.org/viewmedia.cfm?uri=optica-7-8-881&seq=0&html=true.

[36] C. T. Phare, M. C. Shin, S. A. Miller, B. Stern, and M. Lipson, "Silicon optical phased array with high-efficiency beam formation over 180 degree field of view," Feb. 2018. [Online]. Available: http://arxiv.org/abs/1802.04624.

[37] W. Song, R. Gatdula, S. Abbaslou, M. Lu, A. Stein, W. Y. Lai, J. Provine, R. F. W. Pease, D. N. Christodoulides, and W. Jiang, "High-density waveguide superlattices with low crosstalk," *Nature Communications*, vol. 6, May 2015, ISSN: 20411723. DOI: 10.1038/ncomms8027.

[38] B. E. A. Saleh and M. C. Teich, *Fundamentals of Photonics*, 3rd ed. Wiley, Feb. 2019, vol. 2. [Online]. Available: https://www.wiley.com/en-us/Fundamentals+of+Photonics%2C+2+Volume+Set%2C+3rd+Edition-p-9781119506874.

[39] Z. Kong, Y. J. Lee, A. A. Noman, Y. Tang, G. Chang, R. Chen, and M. Qi, "Aliasing-free beam steering from an optical array emitter with half-wavelength pitch," *OSA Advanced Photonics Congress (AP) 2020 (IPR, NP, NOMA, Networks, PVLED, PSC, SPPCom, SOF) (2020), paper ITh2H.6*, vol. Part F184-IPRSN 2020, ITh2H.6, Jul. 2020. DOI: 10.1364/IPRSN.2020.ITH2H.6. [Online]. Available: https://www.osapublishing.org/abstract.cfm?uri=IPRSN-2020-ITh2H.6.

[40] W. D. Sacher, J. C. Mikkelsen, P. Dumais, J. Jiang, D. Goodwill, X. Luo, Y. Huang, Y. Yang, A. Bois, P. G.-Q. Lo, E. Bernier, and J. K. S. Poon, "Tri-layer silicon nitride-on-silicon photonic platform for ultra-low-loss crossings and interlayer transitions," *Optics Express*, vol. 25, p. 30 862, 25 Dec. 2017, ISSN: 1094-4087. DOI: 10.1364/OE.25.030862. [Online]. Available: https://www.osapublishing.org/abstract.cfm?URI=oe-25-25-30862.

[41] R. Takei, Y. Maegami, E. Omoda, Y. Sakakibara, M. Mori, and T. Kamei, "Low-loss and low wavelength-dependence vertical interlayer transition for 3d silicon photonics," *Optics Express*, vol. 23, p. 18 602, 14 Jul. 2015, ISSN: 1094-4087. DOI: 10.1364/OE.23.018602. [Online]. Available: https://www.osapublishing.org/abstract.cfm?URI=oe-23-14-18602.

[42] K. Shang, S. Pathak, G. Liu, S. Feng, S. Li, W. Lai, and S. J. B. Yoo, "Silicon nitride tri-layer vertical y-junction and 3d couplers with arbitrary splitting ratio for photonic integrated circuits," *Optics Express*, vol. 25, p. 10 474, 9 May 2017, ISSN: 1094-4087. DOI: 10.1364/OE.25.010474. [Online]. Available: https://www.osapublishing.org/abstract.cfm?URI=oe-25-9-10474.

[43] M. Bachmann, P. A. Besse, and H. Melchior, "General self-imaging properties in n × n multimode interference couplers including phase relations," *Applied Optics, Vol. 33, Issue 18, pp. 3905-3911*, vol. 33, pp. 3905–3911, 18 Jun. 1994, ISSN: 2155-3165. DOI: 10.1364/AO.33.003905. [Online]. Available: https://www.osapublishing.org/viewmedia.cfm?uri=ao-33-18-3905&seq=0&html=true%20https://www.osapublishing.org/abstract.cfm?uri=ao-33-18-3905%20https://www.osapublishing.org/ao/abstract.cfm?uri=ao-33-18-3905.

[44] R. Ulrich and G. Ankele, "Self-imaging in homogeneous planar optical waveguides," *Applied Physics Letters*, vol. 27, pp. 337–339, 6 1975. DOI: 10.1063/1.88467.

[45] L. B. Soldano, F. B. Veerman, M. K. Smit, B. H. Verbeek, A. H. Dubost, and E. C. Pennings, "Planar monomode optical couplers based on multimode interference effects," *Journal of Lightwave Technology*, vol. 10, pp. 1843–1850, 12 1992. DOI: 10.1109/50.202837.

[46] H. Zhang, C. Li, X. Tu, X. Luo, M. Yu, and P. G.-Q. Lo, "High efficiency silicon nitride grating coupler," *Applied Physics A 2013 115:1*, vol. 115, pp. 79–82, 1 Sep. 2013, ISSN: 1432-0630. DOI: 10.1007/S00339-013-7954-2. [Online]. Available: https://link.springer.com/article/10.1007/s00339-013-7954-2.

[47] Z. Zhao and S. Fan, "Design principles of apodized grating couplers," *Journal of Lightwave Technology, Vol. 38, Issue 16, pp. 4435-4446*, vol. 38, pp. 4435–4446, 16 Aug. 2020. DOI: 10.1364/JLT.38.004435. [Online]. Available: https://www.osapublishing.org/abstract.cfm?uri=jlt-38-16-4435%20https://www.osapublishing.org/jlt/abstract.cfm?uri=jlt-38-16-4435.

[48] K. J. Seu, A. P. Pandey, F. Haque, E. A. Proctor, A. E. Ribbe, and J. S. Hovis, "Effect of surface treatment on diffusion and domain formation in supported lipid bilayers," *Biophysical Journal*, vol. 92, p. 2445, 7 2007. DOI: 10.1529/BIOPHYSJ.106.099721. [Online]. Available: /pmc/articles/PMC1864818/%20/pmc/articles/PMC1864818/?report=abstract%20https://www.ncbi.nlm.nih.gov/pmc/articles/PMC1864818/.

[49] C. Bourreau, Y. Catherine, and P. Garcia, "Growth kinetics and step coverage in plasma deposition of silicon dioxide from organosilicon compounds," *Materials Science and Engineering: A*, vol. 139, pp. 376–379, C Jul. 1991, ISSN: 0921-5093. DOI: 10.1016/0921-5093(91)90645-4.

[50] A. V. D. K. Modified and R. Murali, "Proximity effect in e-beam lithography," Georgia Institute of Technology. [Online]. Available: https://nanolithography.gatech.edu/proximity.pdf.

[51] S. Aya, K. Kise, H. Y. H. Yabe, and K. M. K. Marumoto, "Validity of double and triple gaussian functions for proximity effect correction in x-ray mask writing," *Japanese Journal of Applied Physics*, vol. 35, p. 1929, 3R Mar. 1996, ISSN: 1347-4065. DOI: 10.1143/JJAP.35.1929. [Online]. Available: https://iopscience.iop.org/article/10.1143/JJAP.35.1929%20https://iopscience.iop.org/article/10.1143/JJAP.35.1929/meta.

[52] R. Nanofabrication. (). Proximity effect correction – getting your design precisely implemented on every sample, [Online]. Available: https://www.raith.com/technology/nanofabrication-software/proximity-effect-correction/. (accessed: 10.23.2021).

[53] C.-C. Yang and W.-C. Chen, "The structures and properties of hydrogen silsesquioxane (hsq) films produced by thermal curing," *Journal of Materials Chemistry*, vol. 12, pp. 1138–1141, 4 Mar. 2002, ISSN: 1364-5501. DOI: 10.1039/B107697N. [Online]. Available: https://pubs.rsc.org/en/content/articlehtml/2002/jm/b107697n%20https://pubs.rsc.org/en/content/articlelanding/2002/jm/b107697n.

[54] "Comparative study of thermally cured and electron-beam-exposed hydrogen silsesquioxane resists," *Journal of Vacuum Science and Technology B: Microelectronics and Nanometer Structures Processing, Measurement, and Phenomena*, vol. 26, p. 1654, 5 Sep. 2008, ISSN: 1071-1023. DOI: 10.1116/1.2960565. [Online]. Available: https://avs.scitation.org/doi/abs/10.1116/1.2960565.

[55] A. L. Bogdanov, J. Lapointe, and J. H. Schmid, "Electron-beam lithography for photonic waveguide fabrication: Measurement of the effect of field stitching errors on optical performance and evaluation of a new compensation method," *Journal of Vacuum Science and Technology B, Nanotechnology and Microelectronics: Materials, Processing, Measurement, and Phenomena*, vol. 30, p. 031 606, 3 Apr. 2012, ISSN: 2166-2746. DOI: 10.1116/1.3700439. [Online]. Available: https://avs.scitation.org/doi/abs/10.1116/1.3700439.

[56] C. V. Poulton, M. J. Byrd, M. Raval, Z. Su, N. Li, E. TiImurdogan, D. Coulbaugh, D. Vermeulen, and M. R. Watts, "Large-scale silicon nitride nanophotonic optical phased arrays at infrared and visible wavelengths," *Optics Letters*, vol. 42, 1 2016, ISSN: 0146-9592. DOI: 10.1364/OL.42.000021.

[57] D. S. Black, U. Niedermayer, Y. Miao, Z. Zhao, O. Solgaard, R. L. Byer, and K. J. Leedle, "Net acceleration and direct measurement of attosecond electron pulses in a silicon dielectric laser accelerator," *Physical Review Letters*, vol. 123, p. 264 802, 26 Dec. 2019, ISSN: 10797114. DOI: 10.1103/PHYSREVLETT.123.264802/FIGURES/3/MEDIUM. [Online]. Available: https://journals.aps.org/prl/abstract/10.1103/PhysRevLett.123.264802.

VITA

Yun Jo Lee was born in Seoul, South Korea, in 1989. He obtained his Bachelor of Science degree in Engineering Physics from University of Illinois at Urbana-Champaign in 2014. He obtained his Master of Science degree in Electrical and Computer Engineering from Purdue University, West Lafayette, in 2017. He is pursuing his Ph.D degree in the school of Electric and Computer Engineering in Purdue University, West Lafayette. He is a research assistant in Nanophotonics fabrication group in Birck Nanotechnology center. His research interests include integrated photonic device fabrication, simulation, and characterization.